Funded by the European Union NextGenerationEU

Ministero dell'Università e della Ricerca

Italiadomani
PIANO NAZIONALE DI RIPRESA E RESILIENZA

The doctoral scholarship was funded by
the European Union – Next Generation EU, Mission 4 Component 2, CUP D93D22001360001

Politecnico di Bari

Department of Mechanics, Mathematics and Management

Ph.D. Program in

ENGINEERING AND AEROSPACE SCIENCES

SSD: ING-IND/04 – Aerospace Structures

Final Dissertation

Modelling and design of origami-inspired deployable structures for aerospace applications

candidate

Andrea Troise

Supervisors:

Prof. Maria Cinefra

Prof. Paolo Celli

Coordinator of Ph.D. Program:

Prof. Caterina Ciminelli

XXXVIII Ph.D. Cycle – A.Y. 2022/2025

Funded by the European Union NextGenerationEU

Ministero dell'Università e della Ricerca

Italiadomani
PIANO NAZIONALE DI RIPRESA E RESILIENZA

The doctoral scholarship was funded by
the European Union – Next Generation EU, Mission 4 Component 2, CUP D93D22001360001

Politecnico di Bari

Department of Mechanics, Mathematics and Management

Ph.D. Program in

ENGINEERING AND AEROSPACE SCIENCES

SSD: ING-IND/04 – Aerospace Structures

Final Dissertation

Modelling and design of origami-inspired deployable structures for aerospace applications

candidate

Andrea Troise

Supervisors:

Prof. Maria Cinefra

Prof. Paolo Celli

Coordinator of Ph.D. Program:

Prof. Caterina Ciminelli

XXXVIII Ph.D. Cycle – A.Y. 2022/2025

"Dai un cuore al cervello
e un cervello al cuore."

Acknowledgments

"To me, it underscores our responsibility to deal more kindly with one another, and to preserve and cherish the pale blue dot, the only home we've ever known."
– Carl Sagan, *Pale Blue Dot*, 1994

I am profoundly grateful to Prof. Maria Cinefra for her constant encouragement and for the trust she placed in me, in my abilities, and in my potential.
Her unwavering support, intellectual rigor, and confidence in my work have been a continuous source of motivation, and have played a decisive role in my academic and professional development.

I would also like to sincerely thank Prof. Paolo Celli for his steadfast support over more than two years overseas, as well as during the months we spent together at Stony Brook University, which passed far too quickly.
His availability, insight, and commitment were invaluable for me.

I would like to deeply thank the entire Astradyne team for welcoming me as a newly graduated student and for fostering my growth, both professionally and personally.
Every member of the team has had a profound impact on me.
I owe Astradyne far more than a doctoral degree.
Without Astradyne, I would not be working in the space sector today; for this, I offer my heartfelt and forever-lasting gratitude.

I wish to thank my friends, my family, and my loved one.
These three years have been intense, at times overwhelmingly so, and without your support, I would certainly not have been able to complete this journey.

I dedicate this work to my mother, the strongest woman I know.
I owe her my life, and far more than words can express.

Abstract

The increasing power demand of modern spacecraft requires solar arrays that are both lightweight and highly compactable. Origami-inspired deployable structures offer an effective solution, achieving large deployed areas within limited launch volumes. However, their strongly nonlinear folding behaviour poses significant challenges for numerical modelling: full finite element analyses are accurate but computationally expensive, limiting their use in early-stage design.

This PhD research, conducted in collaboration with Astradyne Srl, an Italian start-up developing textile-based photovoltaic technologies, addresses this gap by advancing reduced-order modelling techniques for origami-inspired systems.
Astradyne's core technology merges high-performance textile with rigid-flexible electronics, enabling ultralightweight deployable solar arrays, which motivates the need for efficient and predictive simulation tools.

Building upon existing reduced-order methods, this work develops a new *dynamic bar and hinge framework* that extends classical quasi-static formulations to time-dependent behaviour. The framework is implemented in MATLAB, incorporating inertia and damping and supporting multiple integration schemes (Forward Euler, Newmark–β, and HHT–α). Validation against analytical cases and high-fidelity finite element models demonstrates accurate predictions of deployment transients, oscillations, and post-deployment dynamics.

The proposed method preserves the computational efficiency of bar and hinge models while expanding their applicability to dynamic analyses. It thus provides both a methodological advancement in the mechanics of deployable structures and a practical design tool for next-generation origami-based solar arrays and lightweight space systems.

Contents

Introduction

This dissertation opens with a prefatory chapter that situates the research within its technological and industrial context. It explains the motivation that led to the development of a low computational cost simulation framework for origami–inspired deployable structures, a requirement that emerged directly from the work of *Astradyne* on textile–based electronic laminates for foldable and lightweight solar arrays. The prefatory section, titled *"The Textile–Based Technology as Rationale for the Research"*, therefore provides the reader with a comprehensive understanding of the link between industrial objectives and the scientific framework underpinning this study.

Chapter 1 reviews the state of the art in modelling techniques for origami–inspired deployable structures, with emphasis on applications in the aerospace domain. It surveys the principal numerical modelling strategies, from continuum mechanics and discrete shell formulations to reduced–order and multibody approaches, and highlights the trade–off between computational cost and physical fidelity. Within this context, the *bar–and–hinge* method is introduced as an effective reduced–order approach capable of capturing large folding deformations with a limited number of degrees of freedom. The chapter concludes by identifying the main limitations of current implementations, particularly the lack of robust dynamic capabilities, thus motivating the developments presented in the following chapters.

Chapter 2 presents the quasi–static formulation of the bar–and–hinge model. It details the geometric decomposition of origami structures into bar and hinge elements, the derivation of the total potential energy, and the corresponding equilibrium equations. The formulation of the stiffness matrices and the incremental–iterative procedures for solving nonlinear problems are described in depth. Special attention is devoted to the calibration of fold and facet stiffness parameters through analytical scaling relations and finite element benchmarks, ensuring the mechanical consistency of the static solver that forms the foundation for subsequent dynamic extensions.

Chapter 3 extends the bar–and–hinge framework to dynamic simulations. The governing equations of motion are derived together with the associated kinetic energy and mass matrices. Several time–integration schemes are implemented and compared, Forward Euler, Newmark–β, and Hilber–Hughes–Taylor (HHT–α), with

a focus on stability, numerical damping, and energy conservation. The chapter also examines different damping models and algorithmic dissipation mechanisms, leading to a robust, energy–consistent dynamic solver capable of reproducing the transient deployment and oscillatory behaviour of origami structures.

Chapter 4 reports the experimental activities and the integration of the bar and hinge framework. It begins with the design and fabrication of test specimens used to characterise folding stiffness and validate the analytical models. The chapter describes the measurement setup, data acquisition procedure, and the analytical processing of the experimental results to obtain experimental folding stiffness values of simple origami structures. A numerical campaign carried out in ABAQUS complements the experiments, enabling a parametric study on the dependence of the folding stiffness on the hinge geometry. The chapter concludes with the introduction of the complete MATLAB based simulation environment that integrates static and dynamic solvers with experimental calibration.

Chapter 5 presents the validation of the proposed dynamic bar–and–hinge framework. It compares the performance of explicit and implicit time–integration schemes using benchmark problems such as simple folds, Miura–ori unit cells, and multi–cell assemblies. The numerical predictions are assessed against finite element results to verify accuracy, convergence, and computational efficiency. The chapter also discusses the transient response and energy evolution of the models, demonstrating the ability of the framework to capture deployment dynamics with high fidelity and low computational cost.

Chapter 6 summarises the main conclusions and outlines potential future developments. It highlights the contributions of this research to both scientific understanding and industrial application, including improvements in dynamic folding control, contact modelling, and the integration of the framework within broader multi–physics simulation environments. The conclusions emphasise the relevance of the developed methodology to Astradyne's ongoing efforts to design ultralight, textile–reinforced photovoltaic systems, where accurate prediction of folding dynamics is crucial for mission success.

The **Appendix** includes supplementary material supporting the calibration and verification of the bar–and–hinge framework. It provides detailed results from panel–level traction, shear, and bending benchmarks, together with additional MATLAB implementation notes to facilitate reproducibility and future extension of the solver for both academic and industrial use.

In summary, the dissertation follows a progression, from the industrial motivation for efficient deployable systems, through the theoretical formulation of the bar–and–hinge method, to various experimental trials and experiments, and finally dynamic implementation and numerical validation.

Statement of Novelty

This dissertation makes the following original contributions to the field of origami-inspired deployable structures:

- The formulation of a dynamic bar–and–hinge framework that extends traditional quasi-static origami models by consistently incorporating inertia, damping, and implicit time integration. To the author's knowledge, this represents the first reduced-order bar–and–hinge implementation capable of iteratively simulating deployment dynamics within a implicit framework.
- The implementation of the proposed dynamic formulation in a modular MATLAB computational framework, enabling seamless transition from quasi-static analysis to full dynamic simulation without changing modelling assumptions or data structures.
- The use of the reduced-order framework to inform the design of a Mechanical Ground Support Equipment (MGSE), demonstrating how bar–and–hinge simulations can directly guide experimental hardware design.
- The development of a vision-based motion tracking tool intended to support future experimental validation of origami deployment dynamics, enabling non-intrusive measurement of displacements, velocities, and damping properties.





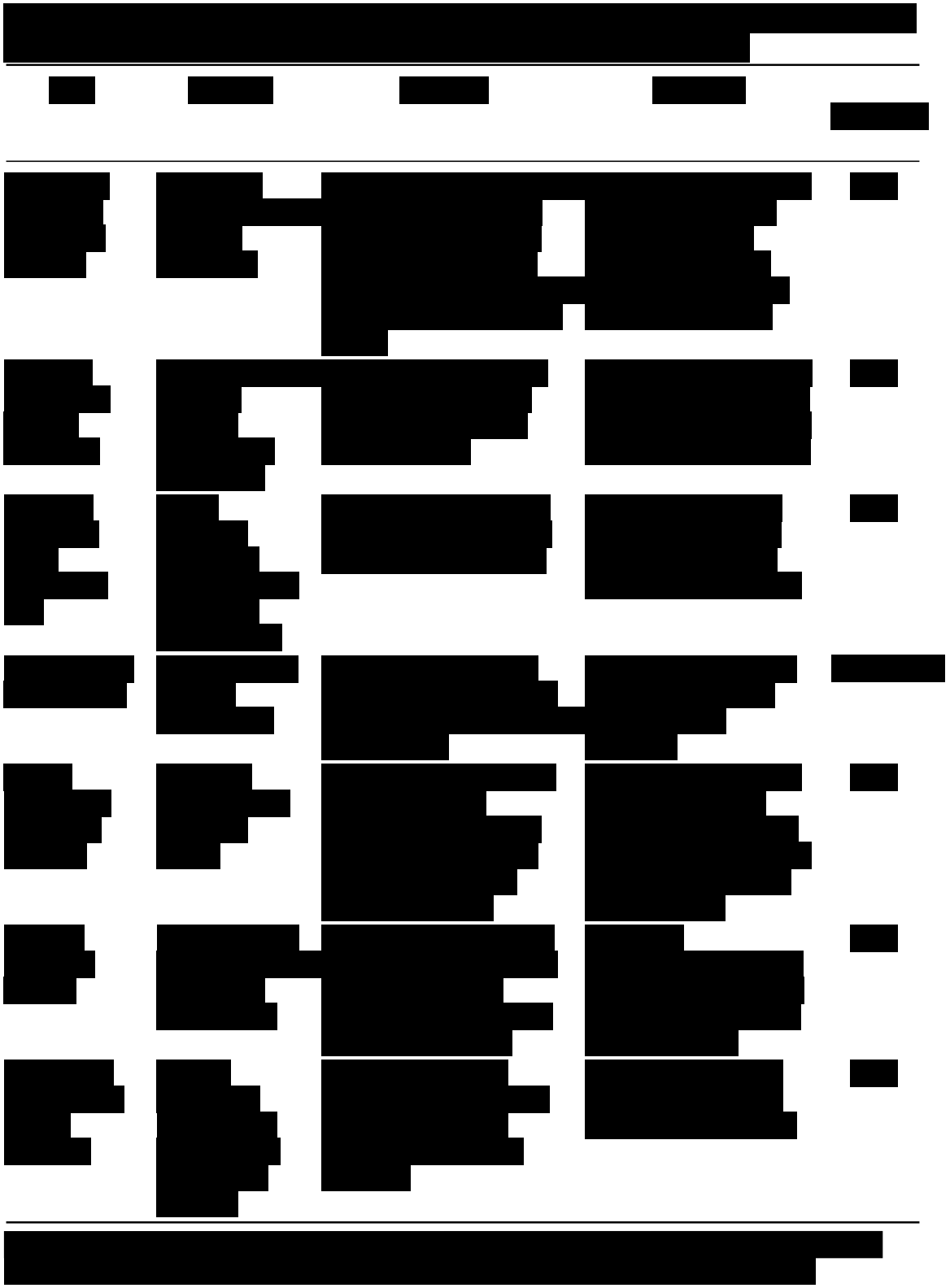

Chapter 1

State of the art in modelling techniques for origami-inspired deployable structures

The design and analysis of origami-inspired deployable structures require computational models that can accurately capture their complex folding kinematics, geometric nonlinearity, and structural response under various loading conditions. This chapter provides a comprehensive review of modelling techniques developed for origami-inspired deployable structures, with particular emphasis on methods relevant to aerospace applications. The review is organized into two main parts: Part I focuses on numerical modelling approaches for structural analysis, while Part II addresses origami structures specifically designed for space applications.

1.1 Numerical Modelling of Deployable Structures

1.1.1 Kinematics and Geometric Foundations of Origami

The kinematic analysis of origami structures provides the foundation for understanding their folding behavior and mechanical properties. This section reviews the fundamental theorems, geometric design methods, and thickness accommodation strategies that enable the transformation of flat sheets into three-dimensional deployable systems.

Rigid origami theory and flat-foldability Rigid origami assumes that panels remain perfectly flat during folding, with all deformation concentrated along crease lines. The kinematics of rigid origami are governed by geometric compatibility theorems that determine whether a given crease pattern can fold flat.
Kawasaki's theorem establishes that a vertex with $2n$ creases forming sector angles

$\alpha_1, \alpha_2, \ldots, \alpha_{2n}$ (as shown in Figure 1.1) is flat-foldable if and only if the alternating sum of these angles equals zero:

$$\alpha_1 - \alpha_2 + \alpha_3 - \cdots - \alpha_{2n} = 0.$$

Equivalently, the sum of alternate angles must equal π. For instance, in Figure 1.1, defining α_1 as the angle between sections A and B, and continuing the enumeration couterclockwise, $\alpha_1 + \alpha_3 + \alpha_5 = \alpha_2 + \alpha_4 + \alpha_6 = \pi$. This geometric relation ensures that the paper can lie flat without stretching or overlapping at the vertex.
Maekawa's theorem [8] provides a complementary condition, stating that at any interior vertex the difference between the number of *mountain* folds (M) and *valley* folds (V) must be ± 2:

$$M - V = \pm 2.$$

Here, *mountain folds* are those that bend away from the observer (convex folds), while *valley folds* bend toward the observer (concave folds). Together, these two theorems define the necessary and sufficient conditions for local flat-foldability of origami vertices [9, 10, 11].

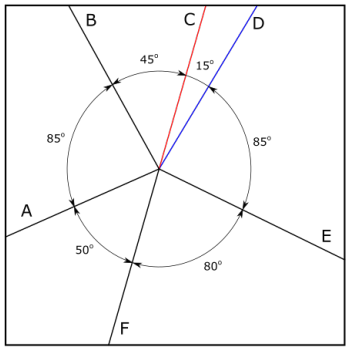

Figure 1.1: Schematic of a flat-foldable vertex with six crease lines (A–F) and corresponding sector angles α_1–α_6, used to verify Kawasaki's theorem. In this example, $\alpha_1 + \alpha_3 + \alpha_5 = \alpha_2 + \alpha_4 + \alpha_6 = \pi$, satisfying the condition for flat-foldability.

These theorems were independently discovered by Toshikazu Kawasaki, Jacques Justin, and documented in early origami mathematics literature [9]. While these conditions are necessary for flat-foldability, they are not always sufficient for rigid origami, as additional constraints may arise from the global connectivity of the crease pattern [12].

Spherical linkages and degree-of-freedom analysis The kinematic behavior of a rigid origami vertex can be described using the framework of spherical linkages, in which each crease is modeled as a revolute joint with its rotation axis passing through the common vertex [13, 14]. At an n-crease vertex, two sets of geometric quantities are defined:

- The *sector angles* $\alpha_1, \alpha_2, \ldots, \alpha_n$ are the planar angles between adjacent crease lines when the pattern is fully unfolded. These angles describe the in-plane geometry of the facets around the vertex.

- The *fold angles* $\theta_1, \theta_2, \ldots, \theta_n$ are the dihedral angles between adjacent facets along each crease line. They quantify the out-of-plane folding motion and define the instantaneous configuration of the vertex during deployment.

For a degree-4 vertex (four creases meeting at a point), the fold and sector angles are related by the spherical closure condition derived from spherical trigonometry [15, 16]:

$$\cos(\theta_i) = \frac{\cos(\alpha_i) - \cos(\theta_{i-1})\cos(\theta_{i+1})}{\sin(\theta_{i-1})\sin(\theta_{i+1})}$$

This equation expresses the geometric compatibility of the folding motion and constrains the admissible configurations of the vertex. For symmetric tessellations such as the Miura–ori, additional angular relationships between creases and facets lead to a reduction to a single degree of freedom, allowing the entire structure to be parametrized by one fold angle [15, 17].
The extension to degree-n vertices and multi-vertex systems requires more sophisticated graph-theoretic approaches. The mobility of an origami structure can be estimated using variants of the Grübler-Kutzbach criterion adapted for spherical mechanisms [18, 19]. However, these estimates may not account for special geometric configurations that lead to additional constraints or freedoms [12].

Thick origami and offset panel techniques Real engineering structures have finite panel thickness, which prevents direct implementation of zero-thickness crease patterns. Several strategies have been developed to accommodate thickness while preserving kinematic behavior. The offset panel technique (OPT) proposed by Edmondson et al. [20, 21] maintains the rotational axes of creases in a reference plane while offsetting panels above or below this plane according to their stacking order. This method preserves both the range of motion and the kinematics of the original zero-thickness pattern, enabling the design of deployable structures with arbitrary panel thickness and material properties [21, 22].
Alternative approaches include tapered panel methods, where panel thickness varies near crease lines to reduce interference [23], and membrane hinge techniques, where compliant zones replace idealized creases [24, 13]. Chen et al. [13] developed a comprehensive kinematic model for thick-panel origami (shown in Fig.1.2) by replacing zero-thickness spherical linkages with spatial linkages that incorporate offset joints, demonstrating agreement with physical prototypes. More recent work addresses seamless surfaces for thick origami tubes [25, 26].

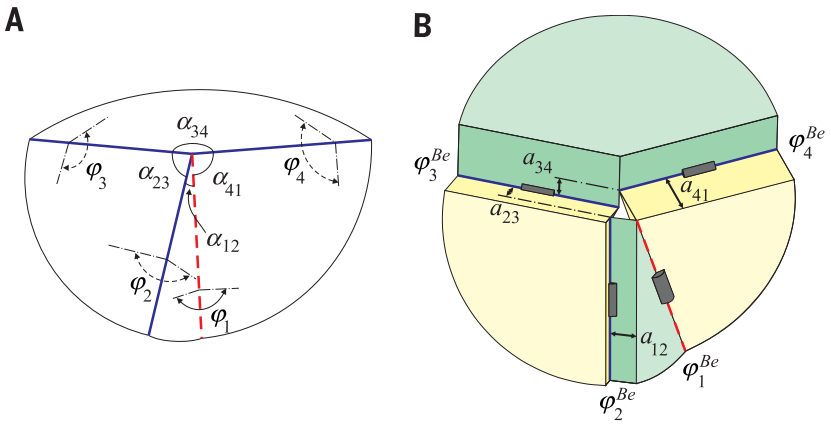

Figure 1.2: (A) Partially folded four-crease rigid origami at a single vertex for a zero-thickness sheet. Blue solid and red dashed lines indicate mountain and valley creases, respectively. The sector angles α_{ij} define the in-plane geometry between adjacent creases, while φ_i denote the dihedral (or fold) angles between connected panels. (B) Thick-panel counterpart with the same sector angles α_{ij} but non-intersecting fold lines due to finite thickness. Distances a_{ij} represent offsets between adjacent fold lines, and φ_i^{Be} denote the corresponding dihedral angles in the thick-panel configuration. Adapted from [13].

Classical origami tessellations Several canonical folding patterns have emerged as particularly relevant for deployable structures due to their advantageous mechanical properties and ease of fabrication. The Miura–ori pattern (Fig. 1.3), originally developed by Koryo Miura for space solar array applications [17], consists of identical parallelogram facets connected at a common vertex and repeated in a zigzag tessellation. The in–plane sector angles α and β satisfy the flat–foldability condition $2(\alpha + \beta) = 2\pi$, ensuring geometric compatibility for rigid folding.

The configuration of the Miura–ori can be fully described by a single fold angle θ, defined once again as the dihedral angle between adjacent facets along a crease line. This parameter governs the entire deformation of the pattern, as all other geometric quantities are uniquely determined by θ. Consequently, the Miura–ori behaves as a one–degree–of–freedom mechanism, enabling simultaneous expansion and contraction along two perpendicular directions through a single coordinated folding motion. The pattern exhibits auxetic behavior (negative Poisson's ratio), making it particularly suited for lightweight deployable structures [27, 28].

The Yoshimura pattern (Fig.1.5 and Fig.1.4), originally observed in buckling patterns of compressed cylindrical shells [29], consists of diamond-shaped facets arranged circumferentially. While not rigidly foldable, it provides high axial stiffness in the deployed state and has been applied to deployable booms and structural columns [30, 31, 32]. Recent studies explore generalized Yoshimura patterns with tunable bistability and meta-stable configurations [32].

The Kresling pattern (Fig.1.4 forms a twisted cylindrical structure with inherent

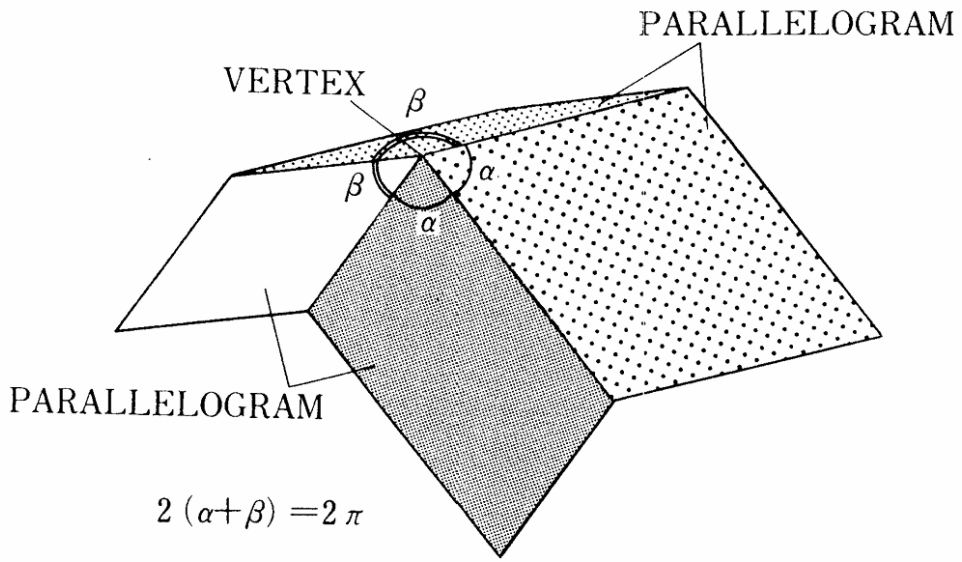

Figure 1.3: Fundamental unit of the Miura-ori tessellation, composed of four identical parallelogram facets connected at a common vertex. The in-plane sector angles α and β satisfy the flat-foldability condition $2(\alpha + \beta) = 2\pi$, ensuring geometric compatibility for rigid folding. The Miura-ori pattern exhibits one-degree-of-freedom kinematics, allowing simultaneous expansion and contraction along both axes under a single folding motion. Image adapted from [17].

bistability, arising from two stable equilibrium configurations separated by an energy barrier [35, 36]. This bistability enables energy absorption, vibration isolation, and morphing structures [36, 37, 38]. Extensions to conical Kresling patterns provide additional design freedom for curvature and deployment paths [39].

The waterbomb base (Fig.1.4), a degree-6 vertex pattern, exhibits complex three-degree-of-freedom kinematics when thickness is neglected [40]. Symmetric waterbomb tessellations can be designed to approximate one-degree-of-freedom deployment through careful control of geometric parameters [14, 41]. Applications include soft robotics, deployable shelters, and programmable metamaterials [42].

The Ron Resch pattern, developed in the 1960s as an architectural tessellation [43], consists of triangular facets with local twisting motions. Its non-developable geometry and coupling between bending and twisting provide unique stiffness characteristics [40, 44, 45]. Recent work explores single-DOF Resch patterns for reliable shape transformation and curvature programming [44, 46].

1.1.2 Continuum Mechanics Approaches

Continuum-based finite element methods provide the highest fidelity representation of origami structures by discretizing both panels and creases with shell or solid

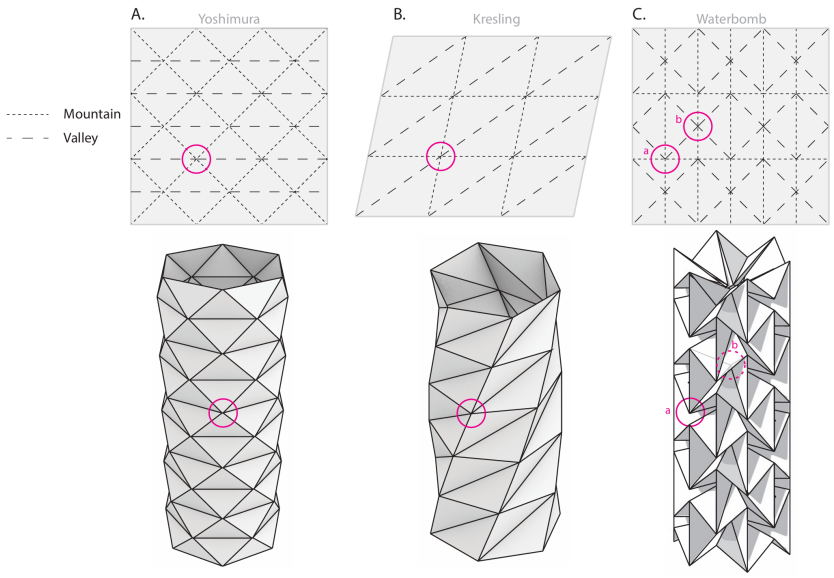

Figure 1.4: Comparison of three canonical origami tessellations forming cylindrical configurations: (A) the Yoshimura pattern, characterized by diamond-shaped facets that yield high axial stiffness; (B) the Kresling pattern, composed of alternating mountain and valley folds producing a twisted bistable cylinder; and (C) the Waterbomb pattern, a degree-6 vertex structure with multi-DOF kinematics that can be tuned toward single-DOF deployment. Each pattern's crease assignment (mountain/valley) and resulting three-dimensional morphology are shown. Image adapted from Lee, *Elastic Energy Behaviours of Curved-Crease Origami* [33].

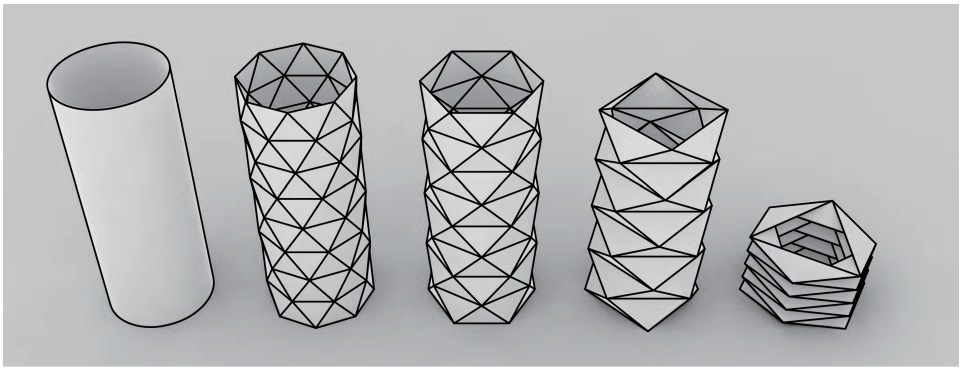

Figure 1.5: Rigid-foldable cylindrical polyhedra derived from the Yoshimura pattern, illustrating the transformation from a smooth cylindrical surface (left) to progressively folded configurations (right). The structure maintains geometric compatibility through a triangulated tessellation that enables controlled axial contraction while preserving overall cylindrical symmetry. Image adapted from Miura and Tachi, *Synthesis of Rigid-Foldable Cylindrical Polyhedra* [34].

elements. These approaches capture material nonlinearity, crease compliance, and local stress concentrations, but at significant computational cost.

Shell theory fundamentals Classical shell theories (Fig.1.6) provide the kinematic and constitutive framework for thin-walled structures. The Kirchhoff-Love theory assumes that normals to the mid-surface remain straight and perpendicular during deformation, neglecting transverse shear deformation [47, 48]. This theory is appropriate for thin shells with thickness-to-radius ratios less than 1/20, and leads to fourth-order partial differential equations requiring C^1 continuity in finite element implementations [49].

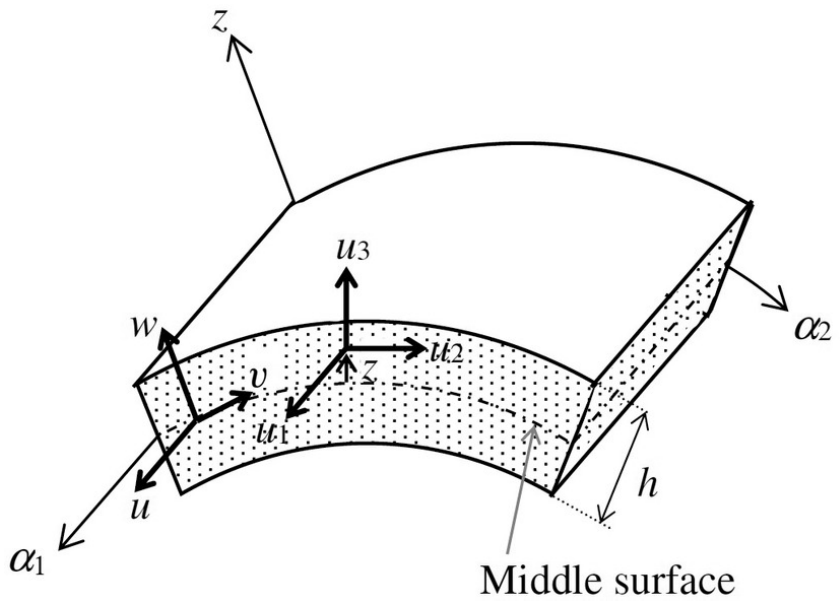

Figure 1.6: Geometric representation of a curved shell element. The middle surface is defined by the curvilinear coordinates (α_1, α_2), with the transverse coordinate z measured along the shell thickness h. The displacement field is described by the tangential components u and v on the middle surface and the transverse deflection w.

Reissner-Mindlin Plate and Shell Theory The Reissner-Mindlin theory, also known as the first-order shear deformation theory (FSDT), extends the classical Kirchhoff-Love formulation by relaxing the assumption that normals to the mid-surface remain perpendicular to it after deformation. In this model, transverse normals are allowed to rotate independently of the mid-surface, introducing additional degrees of freedom that enable the representation of transverse shear deformation [50, 51].
This extension is particularly important for the analysis of moderately thick plates and shells, where the neglect of shear effects, as in Kirchhoff-Love theory, would lead

to significant underestimation of deflections and stresses. The Reissner-Mindlin formulation requires only C_0 continuity of the displacement and rotation fields, making it well suited for finite element implementation [52].
However, a well-known numerical issue arises when this theory is applied to thin structures: as the thickness approaches zero, the transverse shear strains should vanish, but standard finite element discretizations tend to over-constrain this behavior, resulting in an artificially stiff response. This phenomenon, known as shear locking, can severely degrade the accuracy of simulations in the thin-plate limit. To mitigate this effect, several strategies have been developed, including reduced or selective integration, mixed interpolation of tensorial components (MITC) elements, and assumed strain or hybrid formulations [53].
Overall, the Reissner-Mindlin theory provides a robust compromise between the computational simplicity of classical plate theory and the higher accuracy of full three-dimensional elasticity, offering an efficient and reliable framework for modeling moderately thick plates and shells in structural and aerospace applications.
Higher-order theories, including those with polynomial or trigonometric expansion through the thickness, provide improved accuracy for thick laminates and capture zigzag effects in composite structures [54, 55].

Geometric nonlinearity formulations Origami structures undergo large displacements and rotations during folding, necessitating geometrically nonlinear formulations. The Total Lagrangian (TL) formulation refers all kinematic and static variables to the initial undeformed configuration, using the second Piola-Kirchhoff stress tensor and Green-Lagrange strain tensor [56, 57]. The variational statement and tangent stiffness matrix are derived by linearizing the equilibrium equations about the current deformed state.
The Updated Lagrangian (UL) formulation updates the reference configuration at each load step to coincide with the current deformed state [56]. While conceptually similar to TL, UL formulations may offer computational advantages when strains remain moderate despite large rotations [58].
For shell elements, geometric nonlinearity introduces coupling between membrane and bending actions, as well as geometric stiffness contributions that affect buckling and post-buckling behavior [59, 60].

Finite element methods for folded structures Standard shell elements (e.g., SHELL181, SHELL281 in ANSYS; S4R, S8R in Abaqus) can be applied to origami structures by meshing panels and introducing localized compliance or constraints at crease lines [61, 62]. However, care must be taken to avoid shear and membrane locking, particularly in thin panels under folding deformations.
The MITC (Mixed Interpolation of Tensorial Components) family of shell elements addresses locking by interpolating strain components at specific points within the

element, ensuring optimal convergence across thickness ratios [60, 63]. MITC3+ and MITC4 elements have been successfully applied to geometric nonlinear analysis of origami-like folded plates [60, 64].
Isogeometric Analysis (IGA) leverages NURBS or B-spline basis functions from computer-aided design (CAD) to represent both geometry and solution fields [65, 66]. IGA naturally satisfies C^1 continuity requirements for Kirchhoff-Love shells and reduces geometric approximation errors [67, 68]. Recent implementations support trimmed multi-patch geometries and integration with commercial finite element codes [69, 70].

Crease modeling in continuum FEM Representing fold lines in continuum models requires special treatment to localize bending deformation. Common strategies include: (i) reduced stiffness zones, where elements along creases have diminished material properties [24]; (ii) rotational spring connectors linking adjacent panels, calibrated to match crease bending stiffness [62, 71]; (iii) cohesive zone models to simulate progressive crease folding and potential damage [72]; (iv) multi-point constraints (MPC) enforcing kinematic compatibility across fold lines [15].
Contact algorithms are essential to prevent self-intersection during large-amplitude folding. Penalty-based, Lagrange multiplier, and augmented Lagrangian contact formulations have been employed, with smoothing techniques to avoid numerical instabilities near fold closure [73, 74].

Advanced finite element techniques The Absolute Nodal Coordinate Formulation (ANCF), originally developed for flexible multibody dynamics, uses global position vectors and their gradients as nodal coordinates [75, 76, 77]. ANCF elements exhibit a constant mass matrix and are particularly effective for structures undergoing large rotations and moderate strains. Applications to origami include beam elements for thin creases and plate elements for compliant panels [78].
Meshfree methods, such as smoothed particle hydrodynamics (SPH) and element-free Galerkin (EFG), eliminate the need for a structured mesh and can handle extreme deformations and topology changes [79]. While less common in origami analysis, they offer potential for modeling tearing, cutting, or highly irregular crease patterns.

Carrera Unified Formulation (CUF) The Carrera Unified Formulation provides a hierarchical framework for developing refined structural theories through systematic polynomial expansion of displacement fields across the thickness direction [80, 81]. CUF enables Equivalent Single Layer (ESL) models, where the entire laminate is treated as a single equivalent layer, and Layer-Wise (LW) models, where each ply is represented independently with C^0 continuity at interfaces [82, 83].

CUF-based models systematically converge to three-dimensional elasticity solutions as the expansion order increases, providing a rational path for trading accuracy against computational cost [84, 85]. Applications to origami would involve treating textile-reinforced laminates as layered composites, capturing through-thickness stress distributions and interlaminar effects that are critical for durability and failure prediction [86].
The unified nature of CUF facilitates best theory diagrams (BTDs), where the minimum expansion order required for a given accuracy is determined a priori based on geometry and loading [81]. This capability is particularly valuable in early-stage design of deployable structures, where multiple configurations must be rapidly evaluated.

1.1.3 Discrete and Reduced-Order Models

Reduced-order models strike a balance between the simplified kinematics of rigid origami and the computational expense of full finite element analysis. By representing panels with discrete elements and creases with rotational springs, these approaches enable efficient simulation of large origami assemblies while capturing essential elastic behaviors.

Discrete differential geometry for thin shells Discrete differential geometry (DDG) provides a framework for representing smooth surfaces and their deformations using discrete meshes, preserving key geometric properties such as mean curvature and Gaussian curvature [87, 88]. In DDG-based shell models, bending energy is concentrated at edges (hinges) connecting triangular facets, with the discrete mean curvature normal serving as the natural geometric quantity [87, 89].
The bending energy per unit length along an edge e connecting two triangles with normals $\mathbf{n}_1$ and $\mathbf{n}_2$ is proportional to the squared hinge angle deviation from a rest state:

$$E^e_{\text{bend}} = \frac{1}{2} k_{\text{bend}} \ell_e (\theta - \theta_0)^2$$

where ℓ_e is the edge length, $\theta = \arccos(\mathbf{n}_1 \cdot \mathbf{n}_2)$ is the dihedral angle, and k_{bend} is a bending stiffness coefficient related to material properties and thickness [87, 89].
DDG methods have been successfully applied to simulate paper-like materials, cloth, and origami structures [87, 90, 91]. Their efficiency arises from the sparse, geometrically interpretable formulation of bending and stretching energies, yet reproducing continuum-like behavior demands careful calibration. In particular, bending stiffness coefficients must scale consistently with mesh size to ensure convergence under refinement [87], while the ratio between in-plane and bending stiffness must reflect the material thickness and modulus to preserve near-isometric folding [91]. The element topology and crease alignment strongly affect the accuracy of curvature and strain representation, since irregular triangulations or misaligned fold

edges can introduce artificial anisotropy or stiffening. Furthermore, coupling between stretching and bending energies must be treated consistently to avoid shear locking in large-deformation simulations [90]. Proper scaling, mesh alignment, and rest-angle calibration are therefore essential to achieve physically faithful and numerically stable DDG-based origami simulations.

Bar and hinge models: Historical development The bar and hinge model idealizes origami panels as frameworks of axial bars connected by rotational hinges, thereby discretizing the continuous shell into a minimal set of degrees of freedom. Early applications of truss-like models to folded structures were introduced by Schenk and Guest [15], who represented the in-plane stretching and out-of-plane bending of paper sheets using bar and hinge elements. Filipov et al. [62] systematically developed scalable bar and hinge models capable of reproducing isotropic elastic behavior through careful selection of bar layouts and stiffness calibration. Their approach introduced the N4B5, N4B6, and N5B8 discretization schemes (Fig.1.7), where N denotes the number of nodes and B the number of bars per quadrilateral panel. The N5B8 configuration, featuring a central node connected to all corners by diagonal bars, achieves isotropic in-plane stiffness and enables independent calibration of stretching, shearing, and bending behaviors [62]. Liu and Paulino [93] extended the formulation to large deformations by deriving

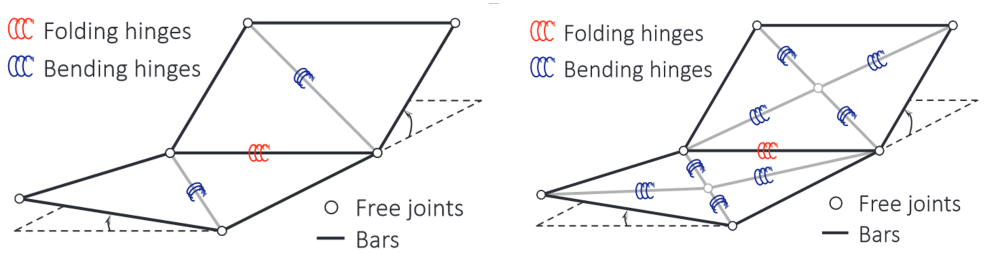

Figure 1.7: Bar–and–hinge discretization scheme for origami structural analysis, image adopted from [92]. Bars represent the in–plane stretching stiffness of the facets, while rotational springs capture hinge compliance. Red springs correspond to folding hinges along crease lines, and blue springs to bending hinges within facets, representing out–of–plane bending. Free joints connect the elements, allowing relative rotation between panels while maintaining geometric compatibility.

consistent tangent stiffness matrices based on energy principles. Their total Lagrangian formulation accounts for geometric nonlinearity through Green-Lagrange strains in bars and exact expressions for hinge angle gradients, ensuring quadratic convergence in Newton-Raphson iterations [93].

Calibration of bar and hinge stiffness The key challenge in bar and hinge modeling is the calibration of element stiffness to reproduce the continuum behavior of thin panels. For a panel of thickness t, Young's modulus E, and Poisson's ratio

ν, the effective bar areas in the N5B8 scheme are derived by matching strain energy under uniaxial tension, pure shear, and bending deformations [62]:

$$A_{\text{x-bar}} = \frac{t(H^2 + W^2)}{2H(1+\nu^2)}, \quad A_{\text{y-bar}} = \frac{t(W^2 + H^2)}{2W(1+\nu^2)}, \quad A_{\text{diag}} = \frac{tHW}{2(1+\nu^2)\sqrt{H^2+W^2}}$$

where H and W are the panel height and width. Rotational hinge stiffness for panel bending is calibrated to match the bending rigidity $D = Et^3/(12(1-\nu^2))$ of a thin plate [62, 71].
For prescribed fold lines, the hinge stiffness can be calibrated from physical crease bending tests or set to represent idealized joints [73, 71]. Compliant crease models, where a finite-width zone exhibits reduced stiffness, have been incorporated to study the influence of crease geometry on global folding behavior [73].

Software implementations: MERLIN and MERLIN2 The bar and hinge method has been implemented in publicly available MATLAB frameworks. MERLIN (Mechanics of Elastic Ridges and Lattices using an Integrated Numerical approach) provides quasi-static equilibrium solvers with arc-length continuation for tracing nonlinear load-displacement paths and detecting snap-through instabilities [92, 62]. The code supports user-defined crease patterns, material properties, and boundary conditions, enabling rapid prototyping of origami designs.
MERLIN2, an enhanced version, improves computational efficiency through vectorized assembly routines, adaptive mesh refinement, and integration with optimization libraries [92]. However, both MERLIN and MERLIN2 are restricted to quasi-static analysis, lacking inertia and damping terms necessary for dynamic deployment simulation [92]. This limitation motivates the development of dynamic bar and hinge frameworks, as pursued in the present dissertation.

Extensions to curved-crease origami While most origami patterns feature straight creases, curved-crease origami introduces additional geometric complexity and enables novel three-dimensional forms [94, 95]. Woodruff and Filipov [71] extended the bar and hinge method to curved creases by discretizing the crease curve into piecewise-linear segments, each represented by a rotational spring. Tangent angle compatibility along the crease ensures smooth folding kinematics, while bending and twisting stiffness can be independently tuned to match experimental observations [71, 95]. Applications of curved-crease models include deployable shells, morphing wings, and architectural surfaces [95, 96].

Truss analogy and lattice models An alternative reduced-order approach treats origami as a spatial pin-jointed framework or tensegrity structure, where bars carry only axial forces and nodes are connected by frictionless hinges [97, 15]. This idealization simplifies the kinematic and static analysis, enabling closed-form

solutions for certain patterns, but neglects bending resistance and may not accurately represent the stiffness of real panels [97].
Homogenization techniques, borrowed from lattice mechanics and metamaterial theory, can be applied to periodic origami tessellations to derive effective continuum properties such as in-plane modulus, Poisson's ratio, and bending stiffness [15, 98, 40]. These effective properties guide the design of origami metamaterials with programmable mechanical characteristics [98, 40].

Energy-based and variational methods Variational formulations based on the principle of minimum potential energy provide a rigorous foundation for deriving equilibrium equations and element stiffness. The total potential energy of an origami assembly is decomposed into contributions from bar stretching, hinge bending, and external loads [93]:

$$\Pi = \sum_{i=1}^{n_{\text{bars}}} U_i^{\text{bar}} + \sum_{j=1}^{n_{\text{hinges}}} U_j^{\text{hinge}} - \mathbf{F}_{\text{ext}}^T \mathbf{u}$$

where $\mathbf{u}$ is the global displacement vector. Equilibrium is obtained by setting $\delta\Pi = 0$, yielding the residual force vector $\mathbf{R}(\mathbf{u}) = \partial\Pi/\partial\mathbf{u} = \mathbf{0}$.
Dynamic relaxation, a pseudo-dynamic iterative method, can be employed to find equilibrium configurations without forming the tangent stiffness matrix [99]. However, explicit time-integration schemes may exhibit slow convergence for stiff systems. [100]
Particle-spring models, commonly used in computational cloth simulation and computer graphics, represent sheets as networks of mass points connected by springs [101, 102]. Software such as Kangaroo (Grasshopper plug-in) implements particle-spring dynamics with goal-seeking algorithms to achieve target geometries. While intuitive and visually appealing, these models are typically calibrated in an ad hoc manner, with spring stiffness and damping parameters tuned heuristically rather than derived systematically from measurable material properties. As a result, their predictive capability is limited, and convergence to physically accurate equilibrium configurations is not guaranteed.

1.1.4 Multibody Dynamics and Analytical Models

Multibody dynamics (MBD) treats origami structures as assemblies of rigid or flexible bodies connected by kinematic joints, enabling efficient simulation of deployment with inertial effects, contact, and actuation forces.

Rigid multibody formulations In rigid MBD, each panel is modeled as a rigid body with six degrees of freedom (three translations, three rotations), and creases

are represented as revolute joints [103, 104]. The equations of motion are derived using Lagrange's equations, Kane's method, or the Newton-Euler formulation:

$$\mathbf{M}(\mathbf{q})\ddot{\mathbf{q}} + \mathbf{C}(\mathbf{q}, \dot{\mathbf{q}}) = \mathbf{Q}_{\text{ext}} + \mathbf{Q}_{\text{constr}}$$

where $\mathbf{q}$ is the vector of generalized coordinates, $\mathbf{M}$ is the mass matrix, $\mathbf{C}$ contains Coriolis and centrifugal terms, $\mathbf{Q}_{\text{ext}}$ are external forces, and $\mathbf{Q}_{\text{constr}}$ are constraint forces enforcing kinematic joints. Joint constraints introduce algebraic equations, forming a system of differential-algebraic equations (DAEs). Stabilization techniques, such as the Baumgarte method or projection-based methods, are employed to prevent constraint drift during time integration [105, 106].

Flexible multibody dynamics When panel flexibility becomes significant, flexible MBD methods are required. The floating frame of reference (FFR) approach decomposes the motion of each body into a rigid-body motion of a local frame plus elastic deformation relative to that frame [103, 107]. The elastic deformation is typically represented using component mode synthesis or assumed modes, reducing the number of elastic degrees of freedom. The Absolute Nodal Coordinate Formulation (ANCF), previously discussed in the context of finite elements (Sec.1.1.2), is also widely used in flexible MBD for beams, plates, and cables undergoing large deformations [75, 76, 77]. ANCF's constant mass matrix and geometric exactness make it particularly suitable for deployment simulations involving large rotations and moderate strains.
Applications to origami deployment include studies of tape spring hinges, Miura-ori arrays, and gossamer structures [108, 109].

Contact and collision modeling Self-contact between panels is a critical phenomenon in origami deployment, particularly when creases fold beyond 180° or panels approach each other during compaction. Contact models in MBD typically employ penalty-based methods, where a repulsive force proportional to the penetration depth is applied [110, 111]:

$$F_{\text{contact}} = k\delta^n + c\dot{\delta}$$

where δ is the penetration depth, k and n are stiffness parameters (Hertzian contact typically uses $n = 3/2$), and c is a damping coefficient to dissipate energy and stabilize integration [110]. Friction models, including Coulomb friction with regularization (LuGre, Stribeck models), are incorporated to capture tangential contact forces during sliding or sticking [112]. Efficient contact detection algorithms, such as bounding volume hierarchies and sweep-and-prune, reduce computational overhead when many panels are present [74, 73].

Commercial multibody software and applications Commercial MBD packages such as MSC Adams, RecurDyn, and Simpack provide comprehensive environments for modeling, simulating, and animating multibody systems. These tools have been applied to deployable space structures, including solar arrays [108], solar sails [113], antennas, and boom systems [109]. Integration with MATLAB/Simulink enables co-simulation of mechanical deployment with control systems, thermal loads, and spacecraft attitude dynamics [113]. However, rigid MBD cannot capture local stresses or panel bending, requiring coupling with finite element models (flexible MBD) for detailed stress analysis [103].

Analytical models for canonical tessellations For certain origami patterns with high symmetry and low degrees of freedom, analytical or semi-analytical models provide closed-form expressions for deployment dynamics. The Miura-ori sheet, with a single kinematic DOF parametrized by fold angle θ, can be modeled as a lumped-parameter oscillator [28]:

$$I_{\text{eff}}(\theta)\ddot{\theta} + c\dot{\theta} + k(\theta - \rho_0) = M_{\text{ext}}(t)$$

where I_{eff} is the effective inertia, c is damping, k is the fold stiffness, ρ_0 is the rest angle, and M_{ext} is the external moment. Extensions include coupling to panel rocking modes and geometric nonlinearity in the restoring moment [28]. The Kresling pattern's bistability is described by an energy landscape with two potential wells separated by a barrier [36, 27]:

$$U(\theta) = \frac{1}{2}k_1(\theta - \theta_1)^2(\theta - \theta_2)^2$$

from which snap-through thresholds and dynamic overshoot can be predicted. These models inform the design of energy harvesters, vibration isolators, and morphing structures [37, 36]. Waterbomb and flasher folds admit reduced kinematic coordinates that capture radial deployment [40]. Analytical conditions for geometric locking and actuation force requirements have been derived, guiding actuator sizing and mechanism design.

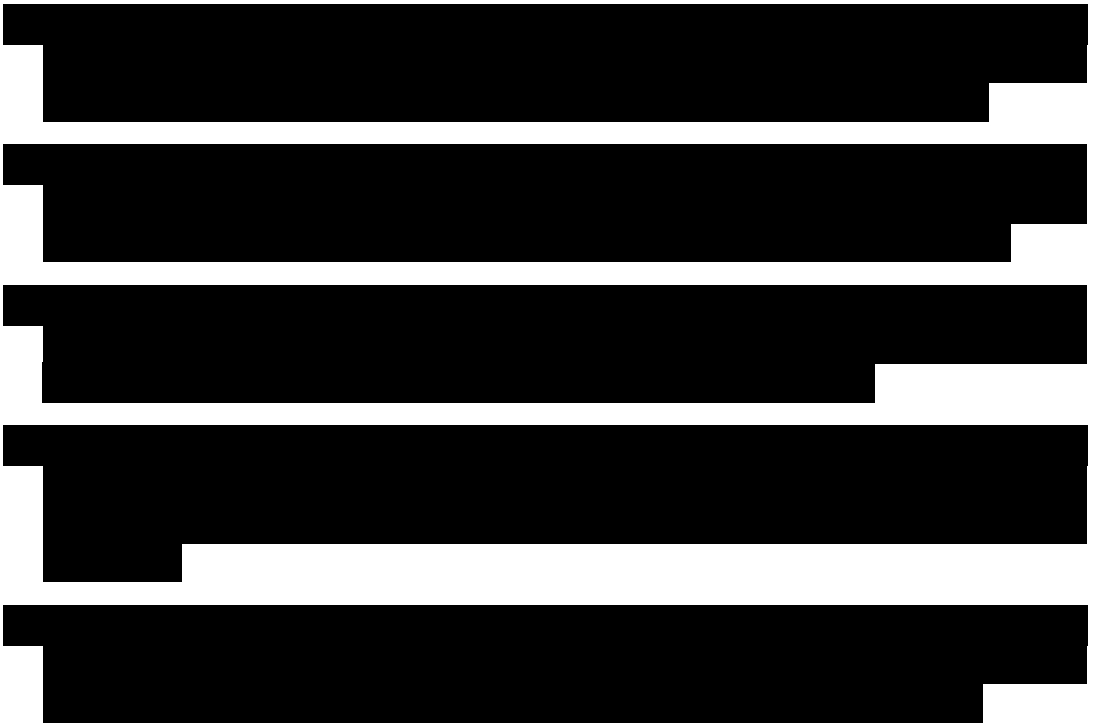

Next chapter introduces the quasi-static bar and hinge numerical framework.

Chapter 2

Quasi-static bar-and-hinge formulation

2.1 Overview and objectives

Origami-inspired structural systems are composed of thin panels connected along fold lines, whose geometric arrangement imparts unique mechanical characteristics such as foldability, reconfigurability and high stiffness-to-weight ratios. Modelling such systems requires a mechanical representation able to capture the fundamental deformation mechanisms while remaining computationally efficient for parametric and design analyses. The *bar-and-hinge* model provides an effective discrete formulation to simulate the quasi-static behaviour of origami and other folded structures. In this approach, the elastic sheet is idealised as a network of linear *bars*, which restrain in-plane deformations (stretching and shear), and rotational *hinges*, which represent out-of-plane bending of panels and rotation along prescribed fold lines. The model reproduces the essential kinematic and elastic features of origami without resorting to full finite element discretisation. The quasi-static formulation presented in this chapter constitutes the first step of the overall mechanical framework of this work. It is derived under the assumptions of:

- geometrically nonlinear, but quasi-static deformation (no inertial effects);
- conservative internal forces (derivable from a potential energy function);
- small strain but potentially large displacement and rotation of elements.

The formulation introduced here provides the foundation for the dynamic extension introduced in Chapter 3, while allowing efficient simulation of equilibrium configurations, stiffness characteristics and load–displacement paths for folded structures.

2.2 Fundamentals of the bar-and-hinge concept

Origami structures are commonly discretised by connecting flat panels with fold lines, which can be interpreted as elastic hinges. Each panel resists stretching, shearing and bending, whereas the fold lines accommodate concentrated rotations. The *bar-and-hinge* abstraction replaces the continuous sheet by a set of discrete elements:

- **Bar elements** — linear axial members connecting nodes, capturing in-plane stretching and shearing of the panels;
- **Rotational hinges** — torsional springs located along folds or panel diagonals, accounting for bending of the sheet.

The model presented in this chapter originates from the seminal works of Schenk and Guest (2011) [149] and was further refined by Filipov *et al.* (2017) [62] and Liu & Paulino (2017) [93]. In particular, Filipov *et al.* formulated scalable bar–hinge configurations (N4B5, N4B6, N5B8) capable of representing isotropic in-plane behaviour, while Liu & Paulino established a fully nonlinear energy-based formulation suitable for large rotations.

2.2.1 Physical decomposition of the model

The elastic behaviour of an origami sheet is decomposed into three fundamental mechanisms:

1. *In-plane stretching and shear* of panels, represented by bar elements of axial stiffness K_S;
2. *Out-of-plane bending* of panels, modelled through rotational hinges of stiffness K_B;
3. *Folding along prescribed creases*, described by additional rotational hinges of stiffness K_F.

Accordingly, the global stiffness matrix of the system can be expressed as the additive contribution of these mechanisms:

$$\mathbf{K} = \mathbf{C}^{\mathrm{T}}\mathbf{D}_S\mathbf{C} + \mathbf{J}_B^{\mathrm{T}}\mathbf{D}_B\mathbf{J}_B + \mathbf{J}_F^{\mathrm{T}}\mathbf{D}_F\mathbf{J}_F = \mathbf{K}_S + \mathbf{K}_B + \mathbf{K}_F, \tag{2.1}$$

where $\mathbf{C}$ denotes the compatibility matrix for bars, $\mathbf{J}_B$ and $\mathbf{J}_F$ are the Jacobian matrices relating angular displacements to nodal coordinates for panel bending and folds, respectively, and $\mathbf{D}_S, \mathbf{D}_B, \mathbf{D}_F$ are diagonal matrices containing the corresponding element stiffness coefficients. Equation (2.1) (adapted from Filipov *et al.*, 2017) defines the structural stiffness of the origami assembly in terms of its constituent bar and hinge components.

2.2.2 Evolution of bar-and-hinge models

Several discretisation schemes have been proposed for panel representation:

- The **N4B5** model, consisting of four corner nodes and five bars (four edges plus one diagonal), provides a first-order approximation of in-plane stiffness but lacks isotropy.
- The **N4B6** model adds a second diagonal bar, forming a statically indeterminate frame able to reproduce Poisson effects and material scaling (E, ν, t).
- The **N5B8** model introduces an additional central node, connecting all diagonals and yielding an isotropic response under in-plane loads while allowing bending representation.

The N5B8 configuration is adopted in this work as it ensures scalability, isotropy, and numerical robustness for large-deformation simulations.

2.2.3 Scope of the quasi-static formulation

The quasi-static model derived in this chapter neglects inertia and damping, focusing instead on the nonlinear equilibrium of the structure:

$$\mathbf{R}(\mathbf{u}) = \mathbf{T}_{\text{bar}}(\mathbf{u}) + \mathbf{T}_{\text{spr}}(\mathbf{u}) - \mathbf{F}_{\text{ext}} = \mathbf{0}, \tag{2.2}$$

where $\mathbf{u}$ is the global displacement vector, $\mathbf{T}_{\text{bar}}$ and $\mathbf{T}_{\text{spr}}$ are the internal force vectors associated with bar and hinge elements, and $\mathbf{F}_{\text{ext}}$ is the external nodal force vector. The tangent stiffness matrix $\mathbf{K} = \partial\mathbf{R}/\partial\mathbf{u}$ is obtained by consistent linearisation, serving as the foundation for incremental Newton–Raphson solution schemes described later.
The next section introduces the geometric framework and mathematical derivation of the potential energy functional that governs this equilibrium.

2.3 Geometric framework and potential energy formulation

2.3.1 Geometric representation and degrees of freedom

The bar–and–hinge model represents an origami or folded sheet as a network of n nodes, each defined by its spatial coordinates in the undeformed reference configuration $\mathbf{X} = [X_1, Y_1, Z_1, \ldots, X_n, Y_n, Z_n]^T$. During deformation, the nodal positions move to $\mathbf{x} = [x_1, y_1, z_1, \ldots, x_n, y_n, z_n]^T$, and the corresponding displacement vector is

$$\mathbf{u} = \mathbf{x} - \mathbf{X}. \tag{2.3}$$

Each node possesses three translational degrees of freedom (DOFs), such that the total system DOFs equal $3n$. Bar elements connect pairs of nodes and are characterised by axial deformation along their local direction, whereas rotational spring elements connect sets of four nodes and represent bending or folding between two triangular facets. The global configuration is governed by the nodal displacement vector $\mathbf{u}$, from which all internal strains and rotations are derived.

2.3.2 Principle of stationary potential energy

Following the total Lagrangian formulation, the system is assumed to be conservative, and its equilibrium configuration is obtained from the *principle of stationary potential energy*. The total potential energy Π is defined as the sum of internal strain energies stored in the bars and hinges minus the potential of external loads:

$$\Pi(\mathbf{u}) = U_{\text{bar}}(\mathbf{u}) + U_{\text{spr}}(\mathbf{u}) - V_{\text{ext}}(\mathbf{u}), \tag{2.4}$$

where:

- U_{bar} is the strain energy stored in all bar (axial) elements;
- U_{spr} is the strain energy stored in the rotational hinges (folds and bending lines);
- V_{ext} is the potential of the external forces applied to the structure.

Equilibrium corresponds to a stationary value of Π, i.e.

$$\delta\Pi = 0, \tag{2.5}$$

which yields the nonlinear residual equilibrium equation:

$$\mathbf{R}(\mathbf{u}) = \mathbf{T}_{\text{bar}}(\mathbf{u}) + \mathbf{T}_{\text{spr}}(\mathbf{u}) - \mathbf{F}_{\text{ext}} = \mathbf{0}. \tag{2.6}$$

Here:

- $\mathbf{R}(\mathbf{u})$ is the residual force vector;
- $\mathbf{T}_{\text{bar}}$ and $\mathbf{T}_{\text{spr}}$ are the internal force vectors of bars and rotational springs, respectively;
- $\mathbf{F}_{\text{ext}}$ is the external nodal force vector.

2.3.3 Linearisation and tangent stiffness matrix

For incremental-iterative quasi-static analysis, the residual vector (2.6) is linearised with respect to the displacement field, yielding the incremental form:

$$\mathrm{D}\mathbf{R}(\mathbf{u})\,\delta\mathbf{u} = \mathbf{K}(\mathbf{u})\,\delta\mathbf{u}, \tag{2.7}$$

where $\mathrm{D}(\cdot)$ denotes the directional derivative, $\delta\mathbf{u}$ is an incremental displacement vector, and $\mathbf{K}$ is the *tangent stiffness matrix* of the complete system. The tangent stiffness matrix is decomposed into contributions from bar and spring components:

$$\mathbf{K}(\mathbf{u}) = \mathbf{K}_{\text{bar}}(\mathbf{u}) + \mathbf{K}_{\text{spr}}(\mathbf{u}). \tag{2.8}$$

2.3.4 Energy-based formulation of bars and hinges

The total strain energy of the system can be expressed as:

$$U_{\text{int}} = \sum_{e=1}^{n_b} U_{\text{bar}}^{(e)} + \sum_{r=1}^{n_s} U_{\text{spr}}^{(r)}, \tag{2.9}$$

where n_b and n_s are the number of bar and spring elements, respectively. The variation of U_{int} with respect to $\mathbf{u}$ provides the internal force vector:

$$\delta U_{\text{int}} = \mathbf{T}_{\text{bar}}^T\,\delta\mathbf{u} + \mathbf{T}_{\text{spr}}^T\,\delta\mathbf{u}. \tag{2.10}$$

Combining Eqs. (2.4)–(2.10), the total variation of potential energy becomes:

$$\delta\Pi = (\mathbf{T}_{\text{bar}} + \mathbf{T}_{\text{spr}} - \mathbf{F}_{\text{ext}})^T\delta\mathbf{u}, \tag{2.11}$$

from which Eq. (2.6) directly follows.

2.3.5 Matrix representation of stiffness components

By analogy with matrix structural analysis, the global stiffness matrix, symmetric by construction, can be written as

$$\mathbf{K} = \begin{bmatrix}\mathbf{C}\\ \mathbf{J}_B\\ \mathbf{J}_F\end{bmatrix}^T \begin{bmatrix}\mathbf{D}_S & 0 & 0\\ 0 & \mathbf{D}_B & 0\\ 0 & 0 & \mathbf{D}_F\end{bmatrix} \begin{bmatrix}\mathbf{C}\\ \mathbf{J}_B\\ \mathbf{J}_F\end{bmatrix}, \tag{2.12}$$

where:

- $\mathbf{C}$ is the compatibility matrix relating bar extensions to nodal displacements;
- $\mathbf{J}_B$ and $\mathbf{J}_F$ are Jacobian matrices of panel bending and fold rotations with respect to nodal DOFs;

- $\mathbf{D}_S$, $\mathbf{D}_B$, and $\mathbf{D}_F$ are diagonal matrices containing the stiffness coefficients for bars, bending hinges, and fold hinges, respectively.

Equation (2.12) generalises Eq. (2.8) by expressing the total stiffness as the superposition of in-plane, bending, and folding contributions:

$$\mathbf{K} = \mathbf{K}_S + \mathbf{K}_B + \mathbf{K}_F. \tag{2.13}$$

2.3.6 Interpretation and scope

The formulation above represents a generalised quasi-static equilibrium model capable of describing nonlinear configurations of folded sheets. Each term in Eq. (2.13) corresponds to an independent physical mechanism and can be scaled according to the material properties of the panels and folds. The equations remain valid for both developable (flat-foldable) and non-developable origami patterns, and are applicable to both single- and multi-panel systems. In the following sections, explicit element formulations for the bar and rotational spring components are derived to complete the quasi-static bar–and–hinge model.

2.4 Bar element formulation

2.4.1 Kinematics and strain measure (total Lagrangian)

Consider a two–node bar element $e = (a, b)$ with end points $\mathbf{X}_a, \mathbf{X}_b \in \mathbb{R}^3$ in the reference configuration and $\mathbf{x}_a, \mathbf{x}_b \in \mathbb{R}^3$ in the current configuration. Define

$$\mathbf{R} = \mathbf{X}_b - \mathbf{X}_a, \qquad L = \|\mathbf{R}\|, \qquad \mathbf{r} = \mathbf{x}_b - \mathbf{x}_a, \qquad \ell = \|\mathbf{r}\|, \qquad \widehat{\mathbf{R}} = \frac{\mathbf{R}}{L}. \tag{2.14}$$

Let the element nodal displacement vector be

$$\mathbf{u}^{(e)} = \begin{bmatrix} \mathbf{u}_a \\ \mathbf{u}_b \end{bmatrix} = \begin{bmatrix} \mathbf{x}_a - \mathbf{X}_a \\ \mathbf{x}_b - \mathbf{X}_b \end{bmatrix} \in \mathbb{R}^6. \tag{2.15}$$

In a total Lagrangian setting, the one–dimensional Green–Lagrange axial strain of the bar reads

$$E_X \;=\; \frac{1}{2}\left(\frac{\ell}{L}\right)^2 - \frac{1}{2} \;=\; \mathbf{B}_1\,\mathbf{u}^{(e)} + \frac{1}{2}\,(\mathbf{u}^{(e)})^T\,\mathbf{B}_2\,\mathbf{u}^{(e)}, \tag{2.16}$$

with the constant operators

$$\mathbf{B}_1 \;=\; \frac{1}{L}\begin{bmatrix} -\widehat{\mathbf{R}}^T & \widehat{\mathbf{R}}^T \end{bmatrix}, \qquad \mathbf{B}_2 \;=\; \frac{1}{L^2}\begin{bmatrix} \mathbf{I}_3 & -\mathbf{I}_3 \\ -\mathbf{I}_3 & \mathbf{I}_3 \end{bmatrix}. \tag{2.17}$$

Equations (2.16)–(2.17) are exact for arbitrarily large finite displacements and rotations of the bar ends.

2.4.2 Element stored energy and constitutive response

Let $A^{(e)}$ be the (constant) cross–sectional area of element e. Denote by $W(E_X)$ the one–dimensional hyperelastic strain–energy density and by $S_X = \partial W/\partial E_X$ and $C = \partial S_X/\partial E_X$ the associated second Piola–Kirchhoff stress and tangent modulus, respectively. The element stored energy is

$$U_{\text{bar}}^{(e)} \;=\; \int_0^L W(E_X)\, A^{(e)}\, \mathrm{d}X \;=\; A^{(e)}\, L\, W(E_X). \tag{2.18}$$

Specialisation (linear elastic bar). When a linear elastic law is appropriate for the in–plane response,

$$W(E_X) = \tfrac{1}{2} E\, E_X^2, \qquad S_X = E\, E_X, \qquad C = E, \tag{2.19}$$

with E the effective Young's modulus associated with the laminate's in–plane behaviour.

2.4.3 Consistent internal force vector

The virtual work of the element axial force follows from (2.18) and (2.16):

$$\delta U_{\text{bar}}^{(e)} \;=\; A^{(e)}\, L\, S_X\, \delta E_X \;=\; \big(\mathbf{T}_{\text{bar}}^{(e)}\big)^T \delta \mathbf{u}^{(e)}, \tag{2.20}$$

which yields the exact (finite–deformation) element internal force vector

$$\boxed{\;\mathbf{T}_{\text{bar}}^{(e)} \;=\; A^{(e)}\, L\, S_X \Big(\mathbf{B}_1^T + \mathbf{B}_2\, \mathbf{u}^{(e)}\Big).\;} \tag{2.21}$$

2.4.4 Consistent tangent stiffness

Linearising (2.21) with respect to $\mathbf{u}^{(e)}$ and using $\mathrm{d}S_X = C\, \mathrm{d}E_X$ gives the exact tangent

$$\boxed{\;\mathbf{K}_{\text{bar}}^{(e)} \;=\; A^{(e)}\, L\, C \left(\mathbf{B}_1^T + \mathbf{B}_2\, \mathbf{u}^{(e)}\right)\left(\mathbf{B}_1^T + \mathbf{B}_2\, \mathbf{u}^{(e)}\right)^T \;+\; A^{(e)}\, L\, S_X\, \mathbf{B}_2.\;} \tag{2.22}$$

It is often convenient to recognise the standard split

$$\begin{aligned} \mathbf{K}_{\text{bar}}^{(e)} \;=\; & \underbrace{A^{(e)}\, L\, C\, \mathbf{B}_1^T \mathbf{B}_1}_{\mathbf{K}_E^{(e)}} \;+\; \underbrace{A^{(e)}\, L\, C \big[(\mathbf{B}_2 \mathbf{u}^{(e)})\mathbf{B}_1 + \mathbf{B}_1^T (\mathbf{B}_2 \mathbf{u}^{(e)})^T\big]}_{\mathbf{K}_1^{(e)}} \\ & + \underbrace{A^{(e)}\, L\, C\, (\mathbf{B}_2 \mathbf{u}^{(e)})(\mathbf{B}_2 \mathbf{u}^{(e)})^T}_{\mathbf{K}_2^{(e)}} \;+\; \underbrace{A^{(e)}\, L\, S_X\, \mathbf{B}_2}_{\mathbf{K}_G^{(e)}}, \end{aligned} \tag{2.23}$$

where $\mathbf{K}_E^{(e)}$ is the (linear) elastic stiffness, $\mathbf{K}_G^{(e)}$ the geometric stiffness, and $(\mathbf{K}_1^{(e)} + \mathbf{K}_2^{(e)})$ the initial–displacement contribution. Expression (2.22) is symmetric and ensures quadratic convergence of Newton iterations when assembled consistently.

2.4.5 Local–to–global operators and assembly

Equations (2.21)–(2.22) are written in the global Cartesian basis via $\mathbf{R}$ and $\mathbf{r}$ and thus require no element–level rotation. For matrix assembly, it is convenient to introduce the Boolean extractor $\mathbf{P}_e \in \mathbb{R}^{6\times 3n}$ that gathers the element DOFs from the global vector ($\mathbf{u}^{(e)} = \mathbf{P}_e\,\mathbf{u}$). The global contributions read

$$\mathbf{T}_{\text{bar}} \mathrel{+}= \mathbf{P}_e^T\,\mathbf{T}_{\text{bar}}^{(e)}, \qquad \mathbf{K}_{\text{bar}} \mathrel{+}= \mathbf{P}_e^T\,\mathbf{K}_{\text{bar}}^{(e)}\,\mathbf{P}_e, \tag{2.24}$$

preserving symmetry and sparsity. When one prefers to express $\mathbf{B}_1$ in global coordinates using only reference nodal positions, the form

$$\widetilde{\mathbf{B}}_1 \;=\; \frac{1}{L}\Big[-\big(\mathbf{X}_b-\mathbf{X}_a\big)^T/L \quad \big(\mathbf{X}_b-\mathbf{X}_a\big)^T/L\Big] \tag{2.25}$$

is directly obtained from (2.17).

2.4.6 Prestretch, eigenstrain and thermal effects

If a known reference (initial) axial strain E_X^0 is present due to prestretch, manufacturing, or thermal mismatch, the stored energy can be written in terms of the elastic strain $E_X - E_X^0$. For the linear case (2.19),

$$U_{\text{bar}}^{(e)} \;=\; \tfrac{1}{2}\,A^{(e)}\,L\,E\,(E_X-E_X^0)^2, \tag{2.26}$$

which adds a constant initial axial force $A^{(e)}\,L\,E\,E_X^0\big(\mathbf{B}_1^T + \mathbf{B}_2\,\mathbf{u}^{(e)}\big)$ to (2.21) while leaving the tangent (2.22) unchanged. Thermal effects enter through $E_X^0 = \alpha\,\Delta T$ with an effective in–plane thermal expansion α.

2.4.7 Panel–level calibration and scalable bar areas for the N5B8 frame

At the panel scale, bars are arranged in an indeterminate frame to reproduce the in–plane membrane response (stretching and shear) of a homogeneous sheet while keeping a very low number of DOFs. For a rectangular facet of width W and height H, thickness t, and Poisson ratio ν, the N5B8 template assigns areas to horizontal (X), vertical (Y), and short–diagonal (D) bars as

$$A_X = \frac{t\,(H^2-\nu W^2)}{2H\,(1-\nu^2)}, \qquad A_Y = \frac{t\,(W^2-\nu H^2)}{2W\,(1-\nu^2)}, \qquad A_D = \frac{t\,\nu\,(H^2+W^2)^{3/2}}{2HW\,(1-\nu^2)}, \tag{2.27}$$

so that the assembled frame exhibits near–isotropic tensile response and realistic shear behaviour (exact shear matching for $\nu = 1/3$) with a scale–independent definition of bar stiffness $K_S^{(e)} = E\,A^{(e)}/L^{(e)}$ at small strains. For skewed panels, W and H are taken as the average opposing–edge distances, which has been shown to retain good agreement with shell FE benchmarks for both tension and shear. These calibrated areas allow the bar network to represent the in–plane membrane stiffness of the sheet while rotational hinges (Section 2.5) capture out–of–plane bending and prescribed folds. The expressions above complete the bar component of the quasi–static bar–and–hinge model. In the next section, we introduce the rotational hinge (dihedral) operator and its consistent linearisation, which governs both panel bending and folding along crease lines.

2.5 Rotational hinge for folds and facet bending

Each crease or intra-panel bending diagonal is modeled with a four-node rotational spring acting (Fig.2.1) on the ordered node quadruple (i, j, k, ℓ), whose axis is the edge (j, k) and whose adjacent triangular facets are (i, j, k) and (k, j, ℓ). With current nodal positions $\{\mathbf{x}_p\}_{p\in\{i,j,k,\ell\}}$ define edge vectors and unnormalized facet normals

$$\mathbf{r}_{pq} = \mathbf{x}_p - \mathbf{x}_q, \qquad \mathbf{e} = \mathbf{r}_{kj}, \quad \hat{\mathbf{e}} = \frac{\mathbf{e}}{\|\mathbf{e}\|}, \qquad \mathbf{m} = \mathbf{r}_{ij} \times \mathbf{r}_{kj}, \quad \mathbf{n} = \mathbf{r}_{kj} \times \mathbf{r}_{k\ell}. \tag{2.28}$$

2.5.1 Dihedral angle and branch control

The robust, sign-augmented arccos definition has been introduced in [150, 151]:

$$\begin{aligned} \theta &= \eta \arccos\!\left(\frac{\mathbf{m}\cdot\mathbf{n}}{\|\mathbf{m}\|\,\|\mathbf{n}\|}\right) \bmod 2\pi, \\ \eta &= \begin{cases} \operatorname{sgn}(\mathbf{m}\cdot\mathbf{r}_{k\ell}), & \mathbf{m}\cdot\mathbf{r}_{k\ell} \neq 0, \\ 1, & \mathbf{m}\cdot\mathbf{r}_{k\ell} = 0. \end{cases} \end{aligned} \tag{2.29}$$

By convention, $\theta > 0$ denotes a mountain assignment when the ordered set (i, j, k, ℓ) is right-handed. The rest angle θ_0 encodes mountain/valley via its sign.

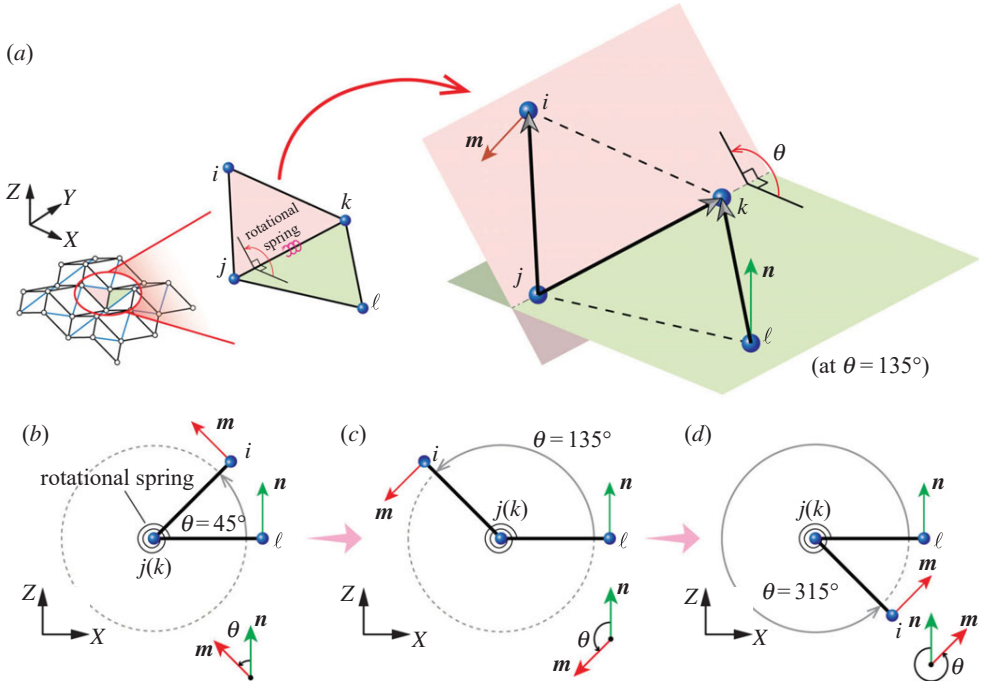

Figure 2.1: Geometry of a rotational spring element and consistent definition of the dihedral (fold) angle. (a) The rotational spring is defined by four nodes (i, j, k, ℓ) forming two triangular facets (i, j, k) and (k, j, ℓ) that meet along the shared edge (j, k). The edge vectors $\mathbf{r}_{ij}$, $\mathbf{r}_{kj}$, and $\mathbf{r}_{k\ell}$ determine the two facet normals $\mathbf{m}$ and $\mathbf{n}$, whose relative orientation defines the dihedral angle θ. (b)–(d) Illustrations of the continuous and consistent assignment of θ as it varies from 0 to 2π, ensuring robust branch control for both mountain and valley configurations. Image adapted from Liu and Paulino, *"Nonlinear mechanics of non-rigid origami: An efficient computational approach," Proc. R. Soc. A*, 2017 [93].

2.5.2 First derivatives (gradient) of the dihedral

To avoid trigonometric singularities, closed-form, singularity-free gradients are used [93]:

$$\frac{\partial\theta}{\partial\mathbf{x}_i} = \frac{\|\mathbf{r}_{kj}\|}{\|\mathbf{m}\|^2}\,\mathbf{m}, \qquad \frac{\partial\theta}{\partial\mathbf{x}_\ell} = -\frac{\|\mathbf{r}_{kj}\|}{\|\mathbf{n}\|^2}\,\mathbf{n}, \tag{2.30}$$

$$\frac{\partial\theta}{\partial\mathbf{x}_j} = \left(\frac{\mathbf{r}_{ij}\cdot\mathbf{r}_{kj}}{\|\mathbf{r}_{kj}\|^2} - 1\right)\frac{\partial\theta}{\partial\mathbf{x}_i} - \frac{\mathbf{r}_{k\ell}\cdot\mathbf{r}_{kj}}{\|\mathbf{r}_{kj}\|^2}\,\frac{\partial\theta}{\partial\mathbf{x}_\ell}, \tag{2.31}$$

$$\frac{\partial\theta}{\partial\mathbf{x}_k} = \left(\frac{\mathbf{r}_{k\ell}\cdot\mathbf{r}_{kj}}{\|\mathbf{r}_{kj}\|^2} - 1\right)\frac{\partial\theta}{\partial\mathbf{x}_\ell} - \frac{\mathbf{r}_{ij}\cdot\mathbf{r}_{kj}}{\|\mathbf{r}_{kj}\|^2}\,\frac{\partial\theta}{\partial\mathbf{x}_i}. \tag{2.32}$$

Stacking the four 3-vectors gives the 12×1 gradient $\mathbf{g}_\theta = \partial\theta/\partial\mathbf{x}$ in node order (i, j, k, ℓ).

2.5.3 Hinge energy, internal force, and tangent

Let $\psi(\theta)$ be the hinge stored energy (fold or facet-bending). Define moment and tangent rotational stiffness

$$M(\theta) = \frac{d\psi}{d\theta}, \qquad k_\theta(\theta) = \frac{dM}{d\theta}. \tag{2.33}$$

Then the element internal force and tangent are

$$\mathbf{T}^{(r)}_{\text{spr}} = M(\theta)\,\mathbf{g}_\theta, \qquad \mathbf{K}^{(r)}_{\text{spr}} = k_\theta(\theta)\,\mathbf{g}_\theta\mathbf{g}_\theta^\top + M(\theta)\,\mathbf{H}_\theta, \tag{2.34}$$

where the exact Hessian $\mathbf{H}_\theta = \partial^2\theta/\partial\mathbf{x}^2 \in \mathbb{R}^{12\times12}$ ensures quadratic Newton convergence near flat or nearly inverted states. For linear torsion, $\psi(\theta) = \frac{1}{2}k_\theta(\theta - \theta_0)^2$ so that $M(\theta) = k_\theta(\theta - \theta_0)$ and k_θ is constant.

2.5.4 Second derivatives (Hessian) of the dihedral

We now list all independent 3×3 blocks of the Hessian from Appendix A of [93]. Denote

$$A = \frac{\mathbf{r}_{ij}\cdot\mathbf{r}_{kj}}{\|\mathbf{r}_{kj}\|^2}, \qquad B = \frac{\mathbf{r}_{k\ell}\cdot\mathbf{r}_{kj}}{\|\mathbf{r}_{kj}\|^2}, \qquad \mathbf{a}\odot\mathbf{b} := \mathbf{a}\otimes\mathbf{b} + \mathbf{b}\otimes\mathbf{a},$$

and the useful derivatives

$$\frac{\partial A}{\partial\mathbf{x}_j} = \frac{(2A-1)\,\mathbf{r}_{kj} - \mathbf{r}_{ij}}{\|\mathbf{r}_{kj}\|^2}, \qquad \frac{\partial B}{\partial\mathbf{x}_j} = \frac{2B\,\mathbf{r}_{kj} - \mathbf{r}_{k\ell}}{\|\mathbf{r}_{kj}\|^2}, \tag{2.35}$$

$$\frac{\partial A}{\partial\mathbf{x}_k} = \frac{-2A\,\mathbf{r}_{kj} + \mathbf{r}_{ij}}{\|\mathbf{r}_{kj}\|^2}, \qquad \frac{\partial B}{\partial\mathbf{x}_k} = \frac{(1-2B)\,\mathbf{r}_{kj} + \mathbf{r}_{k\ell}}{\|\mathbf{r}_{kj}\|^2}. \tag{2.36}$$

With these, the ten unique 3×3 blocks of $\mathbf{H}_\theta$ (node order i, j, k, ℓ) are:

$$\frac{\partial^2\theta}{\partial\mathbf{x}_i\,\partial\mathbf{x}_i} = -\frac{\|\mathbf{r}_{kj}\|}{\|\mathbf{m}\|^4}\left(\mathbf{m}\odot(\mathbf{r}_{kj}\times\mathbf{m})\right), \tag{2.37}$$

$$\frac{\partial^2\theta}{\partial\mathbf{x}_\ell\,\partial\mathbf{x}_\ell} = \frac{\|\mathbf{r}_{kj}\|}{\|\mathbf{n}\|^4}\left(\mathbf{n}\odot(\mathbf{r}_{kj}\times\mathbf{n})\right), \tag{2.38}$$

$$\frac{\partial^2\theta}{\partial\mathbf{x}_i\,\partial\mathbf{x}_k} = \frac{\mathbf{m}\otimes\mathbf{r}_{kj}}{\|\mathbf{m}\|^2\,\|\mathbf{r}_{kj}\|} + \frac{\|\mathbf{r}_{kj}\|}{\|\mathbf{m}\|^4}\left(\mathbf{m}\odot(\mathbf{r}_{ij}\times\mathbf{m})\right), \tag{2.39}$$

$$\frac{\partial^2\theta}{\partial\mathbf{x}_\ell\,\partial\mathbf{x}_j} = \frac{\mathbf{n}\otimes\mathbf{r}_{kj}}{\|\mathbf{n}\|^2\,\|\mathbf{r}_{kj}\|} - \frac{\|\mathbf{r}_{kj}\|}{\|\mathbf{n}\|^4}\left(\mathbf{n}\odot(\mathbf{r}_{k\ell}\times\mathbf{n})\right), \tag{2.40}$$

$$\frac{\partial^2\theta}{\partial\mathbf{x}_i\,\partial\mathbf{x}_j} = -\frac{\mathbf{m}\otimes\mathbf{r}_{kj}}{\|\mathbf{m}\|^2\,\|\mathbf{r}_{kj}\|} + \frac{\|\mathbf{r}_{kj}\|}{\|\mathbf{m}\|^4}\left(\mathbf{m}\odot((\mathbf{r}_{kj}-\mathbf{r}_{ij})\times\mathbf{m})\right), \tag{2.41}$$

$$\frac{\partial^2\theta}{\partial\mathbf{x}_\ell\,\partial\mathbf{x}_k} = -\frac{\mathbf{n}\otimes\mathbf{r}_{kj}}{\|\mathbf{n}\|^2\,\|\mathbf{r}_{kj}\|} - \frac{\|\mathbf{r}_{kj}\|}{\|\mathbf{n}\|^4}\left(\mathbf{n}\odot((\mathbf{r}_{kj}-\mathbf{r}_{k\ell})\times\mathbf{n})\right), \tag{2.42}$$

$$\frac{\partial^2\theta}{\partial\mathbf{x}_j\,\partial\mathbf{x}_j} = \frac{\partial\theta}{\partial\mathbf{x}_i}\otimes\frac{\partial A}{\partial\mathbf{x}_j} + (A-1)\,\frac{\partial^2\theta}{\partial\mathbf{x}_i\,\partial\mathbf{x}_j} - \left(\frac{\partial\theta}{\partial\mathbf{x}_\ell}\otimes\frac{\partial B}{\partial\mathbf{x}_j} + B\,\frac{\partial^2\theta}{\partial\mathbf{x}_\ell\,\partial\mathbf{x}_j}\right), \tag{2.43}$$

$$\frac{\partial^2\theta}{\partial\mathbf{x}_j\,\partial\mathbf{x}_k} = \frac{\partial\theta}{\partial\mathbf{x}_i}\otimes\frac{\partial A}{\partial\mathbf{x}_k} + (A-1)\,\frac{\partial^2\theta}{\partial\mathbf{x}_i\,\partial\mathbf{x}_k} - \left(\frac{\partial\theta}{\partial\mathbf{x}_\ell}\otimes\frac{\partial B}{\partial\mathbf{x}_k} + B\,\frac{\partial^2\theta}{\partial\mathbf{x}_\ell\,\partial\mathbf{x}_k}\right), \tag{2.44}$$

$$\frac{\partial^2\theta}{\partial\mathbf{x}_k\,\partial\mathbf{x}_k} = \frac{\partial\theta}{\partial\mathbf{x}_\ell}\otimes\frac{\partial B}{\partial\mathbf{x}_k} + (B-1)\,\frac{\partial^2\theta}{\partial\mathbf{x}_\ell\,\partial\mathbf{x}_k} - \left(\frac{\partial\theta}{\partial\mathbf{x}_i}\otimes\frac{\partial A}{\partial\mathbf{x}_k} + A\,\frac{\partial^2\theta}{\partial\mathbf{x}_i\,\partial\mathbf{x}_k}\right), \tag{2.45}$$

$$\frac{\partial^2\theta}{\partial\mathbf{x}_\ell\,\partial\mathbf{x}_i} = \mathbf{0}_{3\times3}. \tag{2.46}$$

All remaining six blocks follow by symmetry/transposes, e.g. $\partial^2\theta/(\partial\mathbf{x}_k\,\partial\mathbf{x}_i) = \left[\partial^2\theta/(\partial\mathbf{x}_i\,\partial\mathbf{x}_k)\right]^\top$, etc. Equations (2.37)–(2.46) are free of trigonometric singularities and were verified by finite differences over [0,2π) in [93].

2.5.5 Placement within the bar-and-hinge model

For facet bending we place rotational hinges along panel diagonals following the N5B8 model and its linearization, with the bending Jacobian J_B obtained by assembling $\partial\theta/\partial\mathbf{p}_j$ contributions from each dihedral angle, and the panel-bending stiffnesses stored in the diagonal matrix D_B [62]. Fold-line hinges use the same kinematics with their own constitutive law.

2.5.6 Constitutive relationships for rotational springs

Rotational springs (both fold-line and facet-bending hinges) are governed by a stored energy $\psi(\theta)$, the resisting moment $M(\theta) = \mathrm{d}\psi/\mathrm{d}\theta$, and the tangent rotational

stiffness $k_\theta(\theta) = \mathrm{d}M/\mathrm{d}\theta$ (see §2.5). A classical linear law per unit hinge length is

$$M(\theta) \;=\; L^{(r)}\, k\,\big(\theta - \theta_0\big), \tag{2.47}$$

with constant tangent $k_\theta = L^{(r)}k$ and neutral (stress-free) angle θ_0 [93]. While widely used, the linear model has two limitations: it affords only one tuning parameter, and it does not prevent interpenetration of adjacent panels near $\theta \to 0$ or $\theta \to 2\pi$ without additional kinematic constraints [93]. The moment relationship of rotational springs is addressed more in depth in later sections of this dissertation, starting from section 4.1.3.

Enriched piecewise constitutive law with contact avoidance. To enhance tunability and embed local contact avoidance into the constitutive law, [93] introduces a piecewise moment–angle relationship that is nearly linear in the main operating range while exhibiting *asymptotic* stiffness growth as the dihedral approaches the limiting angles (Fig.2.2). Let k_0 denote the nominal (linear) rotational stiffness per unit length, and let $0 < \theta_1 \le \theta_2 < 2\pi$ be two tunable angles that determine the onset of rapid stiffening. The resisting moment per hinge is

$$M(\theta) \;=\; \begin{cases} L^{(r)}k_0\,(\theta_1 - \theta_0) \;+\; \Big(\dfrac{2k_0\,\theta_1}{\pi}\Big)\,\tan\!\Big(\dfrac{\pi\,(\theta-\theta_1)}{2\,\theta_1}\Big), & 0 < \theta < \theta_1, \\[2ex] L^{(r)}k_0\,(\theta - \theta_0), & \theta_1 \le \theta \le \theta_2, \\[2ex] L^{(r)}k_0\,(\theta_2 - \theta_0) \;+\; \Big(\dfrac{2k_0\,(2\pi-\theta_2)}{\pi}\Big)\,\tan\!\Big(\dfrac{\pi\,(\theta-\theta_2)}{4\pi-2\theta_2}\Big), & \theta_2 < \theta < 2\pi, \end{cases} \tag{2.48}$$

and the corresponding tangent rotational stiffness is continuous and given by

$$k_\theta(\theta) \;=\; \frac{\mathrm{d}M}{\mathrm{d}\theta} \;=\; \begin{cases} L^{(r)}k_0\,\sec^2\!\Big(\dfrac{\pi\,(\theta-\theta_1)}{2\,\theta_1}\Big), & 0 < \theta < \theta_1, \\[2ex] L^{(r)}k_0, & \theta_1 \le \theta \le \theta_2, \\[2ex] L^{(r)}k_0\,\sec^2\!\Big(\dfrac{\pi\,(\theta-\theta_2)}{4\pi-2\theta_2}\Big), & \theta_2 < \theta < 2\pi, \end{cases} \tag{2.49}$$

as reported in equations (2.44)–(2.45) of [93]. This enriched law maintains a constant stiffness $L^{(r)}k_0$ in the central interval $[\theta_1, \theta_2]$ and increases sharply and smoothly near the boundaries. In particular,

$$\text{as } \theta \to 0 \;\Rightarrow\; k_\theta(\theta) \to \infty, \qquad \text{as } \theta \to 2\pi \;\Rightarrow\; k_\theta(\theta) \to \infty, \tag{2.50}$$

providing an *asymptotic barrier* that prevents local panel penetration without introducing explicit contact constraints [93]. The same constitutive form can be used for fold hinges and facet-bending hinges, with different choices of k_0 to reflect crease versus panel-bending stiffness.

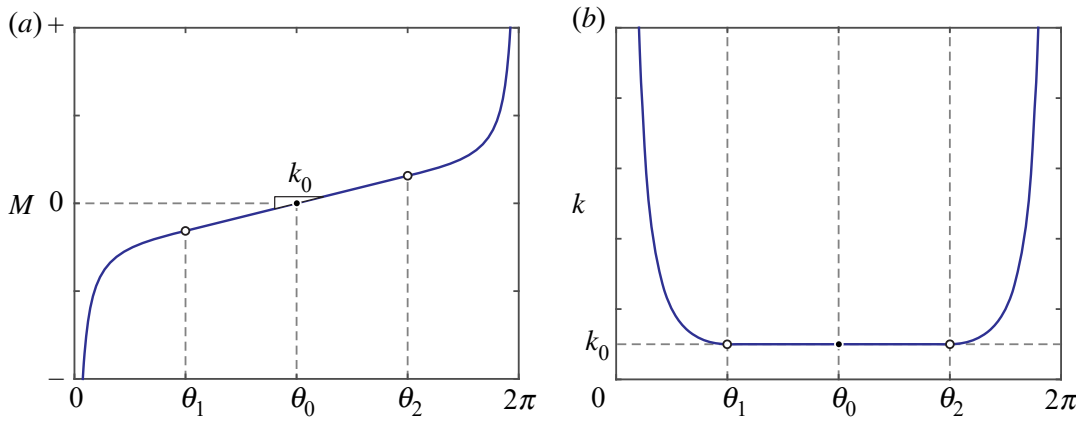

Figure 2.2: Enriched nonlinear constitutive law for rotational springs incorporating local contact avoidance, as proposed by Liu and Paulino [93]. (a) Moment–angle relationship $M(\theta)$ per unit hinge length, defined piecewise to provide nearly linear response in the operating range $[\theta_1, \theta_2]$ and asymptotic stiffening near the limiting angles. (b) Corresponding tangent rotational stiffness $k_\theta(\theta)$, continuous across all branches and exhibiting rapid growth as $\theta \to 0$ and $\theta \to 2\pi$, which prevents local panel interpenetration without explicit contact constraints. The parameters k_0, θ_1, and θ_2 tune the stiffness profile, while the rest angle θ_0 defines the stress-free configuration ($M = 0$). Image adapted from Liu and Paulino, *"Nonlinear mechanics of non-rigid origami: An efficient computational approach," Proc. R. Soc. A*, 2017.

Choice of θ_1, θ_2. The parameters θ_1 and θ_2 are related to the panel thickness and to the desired numerical robustness. Thicker panels call for earlier stiffening (i.e. θ_1 and θ_2 closer to the flat state $\theta = \pi$). At the same time, θ_1 should not be set too close to 0 nor θ_2 too close to 2π, because an excessively sharp barrier can cause a nonlinear solver to step over the stiffness spike and allow penetration [93]. Practical values used in the verification examples include $(\theta_1, \theta_2) = (\pi/2,\, 7\pi/6)$; see §4 of [93].

Remarks on energy. The energy $\psi(\theta)$ associated with (2.48) is obtained by integrating $M(\theta)$ piecewise with respect to θ. For the linear middle interval this yields a quadratic contribution $\frac{1}{2}L^{(r)}k_0(\theta - \theta_0)^2$; the barrier intervals integrate to smooth functions involving $\log\cos(\cdot)$, ensuring continuity of ψ, M, and k_θ across $\theta = \theta_1$ and $\theta = \theta_2$. Because the analysis and implementation require M and k_θ (and their continuity), explicit closed forms of ψ are not necessary for the quasi-static formulation. Equations (2.48)–(2.50) complete the constitutive description of rotational springs used in §2.5. The formulation is compatible with the global assembly of the bar–and–hinge model (§2.4, §2.5) and provides a consistent way to regularize near-contact configurations by means of the hinge law itself [93].

2.6 Solution strategy for quasi-static analysis

The nonlinear equilibrium equation of the bar–and–hinge system,

$$\mathbf{R}(\mathbf{u}, \lambda) = \mathbf{T}_{\text{bar}}(\mathbf{u}) + \mathbf{T}_{\text{spr}}(\mathbf{u}) - \lambda\, \mathbf{F}_0 = \mathbf{0}, \tag{2.51}$$

is solved incrementally by means of a modified Newton–Raphson scheme combined with the *Modified Generalized Displacement Control Method* (MGDCM) [152, 153]. In Eq. (2.51), λ is a scalar load (or displacement) parameter and $\mathbf{F}_0$ is a normalized reference load vector.

2.6.1 Incremental–iterative Newton–Raphson scheme

At iteration i of the n-th load step, the residual vector and tangent stiffness are

$$\mathbf{R}_n^{(i)} = \mathbf{T}_{\text{bar}}(\mathbf{u}_n^{(i)}) + \mathbf{T}_{\text{spr}}(\mathbf{u}_n^{(i)}) - \lambda_n^{(i)}\, \mathbf{F}_0, \qquad \mathbf{K}_n^{(i)} = \mathbf{K}_{\text{bar}}(\mathbf{u}_n^{(i)}) + \mathbf{K}_{\text{spr}}(\mathbf{u}_n^{(i)}). \tag{2.52}$$

A standard Newton–Raphson correction would update the state as

$$\begin{bmatrix} \mathbf{K}_n^{(i)} & -\mathbf{F}_0 \\ \mathbf{c}^{\mathrm{T}} & 0 \end{bmatrix} \begin{bmatrix} \Delta\mathbf{u} \\ \Delta\lambda \end{bmatrix} = - \begin{bmatrix} \mathbf{R}_n^{(i)} \\ g_n^{(i)} \end{bmatrix}, \tag{2.53}$$

where the additional equation $g_n^{(i)} = 0$ enforces the displacement-control constraint through the control vector $\mathbf{c}$ (defined below). The increments $\Delta\mathbf{u}$ and $\Delta\lambda$ are then applied to update

$$\mathbf{u}_n^{(i+1)} = \mathbf{u}_n^{(i)} + \Delta\mathbf{u}, \qquad \lambda_n^{(i+1)} = \lambda_n^{(i)} + \Delta\lambda. \tag{2.54}$$

2.6.2 Modified Generalized Displacement Control Method (MGDCM)

Because bar–and–hinge structures may undergo large geometric nonlinearity and even fold inversion, load-controlled schemes often fail to trace equilibrium paths beyond limit points. The MGDCM overcomes this by expressing the constraint in terms of a *weighted combination of nodal displacements*, allowing automatic load reversal and stable path-following through limit points. The displacement constraint function is defined as

$$g(\mathbf{u}, \lambda) = \mathbf{c}^{\mathrm{T}}(\mathbf{u} - \mathbf{u}_{n-1}) - \Delta\bar{u} = 0, \tag{2.55}$$

where $\Delta\bar{u}$ is the prescribed control increment (usually a scalar displacement magnitude), and $\mathbf{c}$ is a control vector normalized as

$$\mathbf{c} = \frac{\mathbf{u}_n^{(0)} - \mathbf{u}_{n-1}}{\|\mathbf{u}_n^{(0)} - \mathbf{u}_{n-1}\|}, \tag{2.56}$$

representing the tangent direction of the displacement path at the beginning of step n.

Equation (2.53) can then be rewritten explicitly as the MGDCM iteration system:

$$\boxed{\begin{bmatrix} \mathbf{K}_n^{(i)} & -\mathbf{F}_0 \\ \mathbf{c}^{\mathrm{T}} & 0 \end{bmatrix} \begin{bmatrix} \Delta\mathbf{u} \\ \Delta\lambda \end{bmatrix} = - \begin{bmatrix} \mathbf{R}_n^{(i)} \\ \mathbf{c}^{\mathrm{T}}(\mathbf{u}_n^{(i)} - \mathbf{u}_{n-1}) - \Delta\bar{u} \end{bmatrix}.} \tag{2.57}$$

The system (2.57) is symmetric and of order $(3n+1)$; it is solved at each iteration by direct or iterative methods depending on the problem size. After convergence, the control vector $\mathbf{c}$ is updated for the next step based on the last two converged configurations, providing an adaptive load–displacement direction.

2.6.3 Iterative algorithm for MGDCM

For clarity, the MGDCM quasi-static analysis can be summarized by the following algorithm.

Algorithm 1 MGDCM quasi-static solution for bar–and–hinge systems

Input: initial configuration $\mathbf{u}_0 = \mathbf{0}$, $\lambda_0 = 0$, prescribed increment $\Delta\bar{u}$, maximum number of iterations $N_{\mathrm{it,max}}$, tolerance ε.
$n \leftarrow 1$
while $n \le N_{\mathrm{steps}}$ **do**
  Predict $\mathbf{u}_n^{(0)} \leftarrow \mathbf{u}_{n-1}$, $\lambda_n^{(0)} \leftarrow \lambda_{n-1}$
  Compute $\mathbf{c}$ from Eq. (2.56)
  for $i \leftarrow 0,1,2,\ldots$ **do** ▷ until convergence or $i = N_{\mathrm{it,max}}$
    Assemble $\mathbf{R}_n^{(i)}$ and $\mathbf{K}_n^{(i)}$ using Eq. (2.52)
    Form and solve the augmented system (2.57) for $(\Delta\mathbf{u}, \Delta\lambda)$
    Update the state using Eq. (2.54)
    if $\|\mathbf{R}_n^{(i)}\|/\|\mathbf{F}_0\| < \varepsilon$ **then**
      break ▷ converged
    end if
  end for
  Store converged $(\mathbf{u}_n, \lambda_n)$ and update $\mathbf{c}$ for the next load step
  $n \leftarrow n+1$
end while
Output: equilibrium configurations $\{(\mathbf{u}_n, \lambda_n)\}$

2.6.4 Convergence and continuation behaviour

The MGDCM permits automatic transition through limit points (snap-through or snap-back) by allowing the load factor λ to reverse sign according to the displacement path. The step size $\Delta\bar{u}$ may be adapted dynamically, typically reduced when the Newton iterations exceed a predefined number $N_{\mathrm{it,max}}$, or increased after rapid convergence. Convergence is generally quadratic near equilibrium, provided that the consistent tangent stiffness matrices $\mathbf{K}_{\mathrm{bar}}$ and $\mathbf{K}_{\mathrm{spr}}$ (Eqs. (2.22) and (2.34)) are used.

2.6.5 Implementation remarks

The numerical implementation closely follows the MERLIN MATLAB environment reported by [93], where bars and rotational springs are implemented as element functions returning internal forces and consistent tangents. The MGDCM solution strategy is compatible with any constitutive law introduced in Section 2.5.6 and provides robust path-following for strongly nonlinear folding processes. In particular, the asymptotic hinge stiffness (Eq. (2.49)) ensures smooth convergence near self-contact configurations without explicit contact constraints.

2.6.6 Summary of governing relations

The complete quasi–static bar–and–hinge formulation can be summarized as:

$$\text{Kinematics:} \quad \mathbf{u} = \mathbf{x} - \mathbf{X}, \tag{2.58}$$

$$\text{Energy:} \quad \Pi = U_{\mathrm{bar}} + U_{\mathrm{spr}} - V_{\mathrm{ext}}, \tag{2.59}$$

$$\text{Equilibrium:} \quad \mathbf{R}(\mathbf{u}) = \frac{\partial \Pi}{\partial \mathbf{u}} = 0, \tag{2.60}$$

$$\text{Tangent stiffness:} \quad \mathbf{K}(\mathbf{u}) = \frac{\partial^2 \Pi}{\partial \mathbf{u}^2} = \mathbf{K}_{\mathrm{bar}} + \mathbf{K}_{\mathrm{spr}}, \tag{2.61}$$

$$\text{Constitutive relations:} \quad S_X = \frac{\partial W}{\partial E_X},\ C = \frac{\partial^2 W}{\partial E_X^2},\ M(\theta) = \frac{\mathrm{d}\psi}{\mathrm{d}\theta},\ k_\theta(\theta) = \frac{\mathrm{d}^2\psi}{\mathrm{d}\theta^2}. \tag{2.62}$$

These relations, together with the MGDCM procedure described in Section 2.6, completely define the nonlinear static solution process for bar–and–hinge assemblies.

2.7 Creation of the bar and hinge simulation software framework

2.7.1 Preliminary one–dimensional formulation and extension to 3D

The development of the numerical framework began with the formulation of a two–dimensional bar element based on the principle of virtual work. This preliminary step served as a reference for verifying the correctness of all the core finite element operations, evaluation of the internal virtual work, derivation of the element internal force vector, and consistent tangent stiffness matrix, within a simplified kinematic setting.
Starting from this planar case allowed full analytical control over the nonlinear terms and facilitated debugging of the implementation. Once the 2D procedure was validated, the same mathematical structure was generalised to the three–dimensional case by extending the displacement field, strain measure, and transformation operators to vectorial form. The following section reports the 2D formulation used to construct and verify the code, followed by its 3D extension.

Bar element in 2D: virtual work, internal force, and tangent stiffness

For a single 2D bar element in the local coordinate system (x_1, x_2) with undeformed length L_e and cross–sectional area A_e, the internal virtual work is

$$\delta W^e_{\text{int}} = \int_{V_0^e} \mathbf{S}_e : \delta\mathbf{E}_e \, \mathrm{d}V = \int_0^{L_e} A_e \, S_e \, \delta E_e \, \mathrm{d}x, \tag{2.63}$$

where S_e is the (axial) second Piola–Kirchhoff stress, E_e is the axial Green–Lagrange strain, and (for a 1D bar in a Saint–Venant–Kirchhoff material)

$$S_e = C \, E_e, \qquad C \equiv E \, A_e. \tag{2.64}$$

Let the element nodal displacement vector in the *local* CS be

$$\mathbf{u}_e = \begin{bmatrix} u_{1i} & u_{2i} & u_{1j} & u_{2j} \end{bmatrix}^T.$$

Using linear shape functions (Galerkin discretization), the displacement gradient along the local axis is

$$\frac{\mathrm{d}\mathbf{u}}{\mathrm{d}x} = \mathbf{B}_e \, \mathbf{u}_e, \qquad \mathbf{B}_e \;=\; \frac{1}{L_e} \begin{bmatrix} -1 & 0 & 1 & 0 \\ 0 & -1 & 0 & 1 \end{bmatrix}. \tag{2.65}$$

The axial Green–Lagrange strain for a 2D bar undergoing large displacements is

$$E_e = \frac{\mathrm{d}u_1}{\mathrm{d}x} + \frac{1}{2} \left[\left(\frac{\mathrm{d}u_1}{\mathrm{d}x} \right)^2 + \left(\frac{\mathrm{d}u_2}{\mathrm{d}x} \right)^2 \right] = \mathbf{B}_1 \, \mathbf{u}_e + \frac{1}{2} \, \mathbf{u}_e^T \, \mathbf{B}_2 \, \mathbf{u}_e, \tag{2.66}$$

with

$$\mathbf{B}_1 = \frac{1}{L_e}\begin{bmatrix}-1 & 0 & 1 & 0\end{bmatrix}, \qquad \mathbf{B}_2 = \frac{1}{L_e^2}\begin{bmatrix}1 & 0 & -1 & 0\\ 0 & 1 & 0 & -1\\ -1 & 0 & 1 & 0\\ 0 & -1 & 0 & 1\end{bmatrix}. \tag{2.67}$$

The first variation (total derivative) of E_e is obtained by $\delta E_e = \frac{\mathrm{d}}{\mathrm{d}\alpha} E_e(\mathbf{u}_e + \alpha\,\delta\mathbf{u}_e)\big|_{\alpha=0}$, which yields

$$\delta E_e = \mathbf{B}_1\,\delta\mathbf{u}_e + \delta\mathbf{u}_e^T\,\mathbf{B}_2\,\mathbf{u}_e = \big(\mathbf{B}_1^T + \mathbf{B}_2\,\mathbf{u}_e\big)^T\delta\mathbf{u}_e. \tag{2.68}$$

Substituting (2.68) in (2.63) and using (2.64) gives, for a constant–strain one–point element,

$$\delta W_{\text{int}}^e = \big[\,S_e\,A_e\,L_e\,\big]\,\big(\mathbf{B}_1^T + \mathbf{B}_2\,\mathbf{u}_e\big)^T\delta\mathbf{u}_e. \tag{2.69}$$

Hence the *element internal force vector* in the local CS is

$$\boxed{\mathbf{f}_{\text{int}}^e = S_e\,A_e\,L_e\,\big(\mathbf{B}_1^T + \mathbf{B}_2\,\mathbf{u}_e\big)} \qquad \text{with} \quad S_e = E\,E_e = E\big(\mathbf{B}_1\,\mathbf{u}_e + \tfrac{1}{2}\mathbf{u}_e^T\mathbf{B}_2\mathbf{u}_e\big)\,. \tag{2.70}$$

Linearizing (2.70) gives the consistent element tangent $\mathbf{K}_e = \dfrac{\partial\mathbf{f}_{\text{int}}^e}{\partial\mathbf{u}_e}$. Let

$$\mathbf{g}(\mathbf{u}_e) \;=\; \mathbf{B}_1^T + \mathbf{B}_2\,\mathbf{u}_e \quad (4\times 1).$$

Using $\dfrac{\partial S_e}{\partial\mathbf{u}_e} = E\,\dfrac{\partial E_e}{\partial\mathbf{u}_e} = E\,\big(\mathbf{B}_1 + \mathbf{B}_2\,\mathbf{u}_e\big)^T$ and the product rule,

$$\boxed{\mathbf{K}_e = E\,A_e\,L_e\,\mathbf{g}(\mathbf{u}_e)\,\mathbf{g}(\mathbf{u}_e)^T \;+\; S_e\,A_e\,L_e\,\mathbf{B}_2.} \tag{2.71}$$

The first term is the *material* (or constitutive) part, the second is the *geometric* stiffness associated with the current axial force S_eA_e.
Let the element make an angle θ_e with the global X_1-axis. The (block–diagonal) rotation mapping global nodal displacements $\mathbf{u}$ to local ones is

$$\mathbf{u}_e = \mathbf{T}_e\,\mathbf{u}, \qquad \mathbf{T}_e = \begin{bmatrix}\mathbf{R}(\theta_e) & \mathbf{0}\\ \mathbf{0} & \mathbf{R}(\theta_e)\end{bmatrix}, \qquad \mathbf{R}(\theta_e) = \begin{bmatrix}\cos\theta_e & \sin\theta_e\\ -\sin\theta_e & \cos\theta_e\end{bmatrix}. \tag{2.72}$$

Equivalently, using the nodal reference coordinates $\mathbf{X}_i = (X_{1i}, X_{2i})^T$, $\mathbf{X}_j = (X_{1j}, X_{2j})^T$, the direction cosines can be written as

$$\cos\theta_e = \frac{X_{1j} - X_{1i}}{L_e}, \qquad \sin\theta_e = \frac{X_{2j} - X_{2i}}{L_e}, \qquad L_e = \big\|\mathbf{X}_j - \mathbf{X}_i\big\|.$$

For convenience in assembly, define

$$\widetilde{\mathbf{B}}_1 = \mathbf{B}_1\,\mathbf{T}_e, \qquad \widetilde{\mathbf{g}}(\mathbf{u}) = \widetilde{\mathbf{B}}_1^T + \mathbf{B}_2\,\mathbf{u}_e = (\mathbf{B}_1\,\mathbf{T}_e)^T + \mathbf{B}_2\,(\mathbf{T}_e\,\mathbf{u}). \tag{2.73}$$

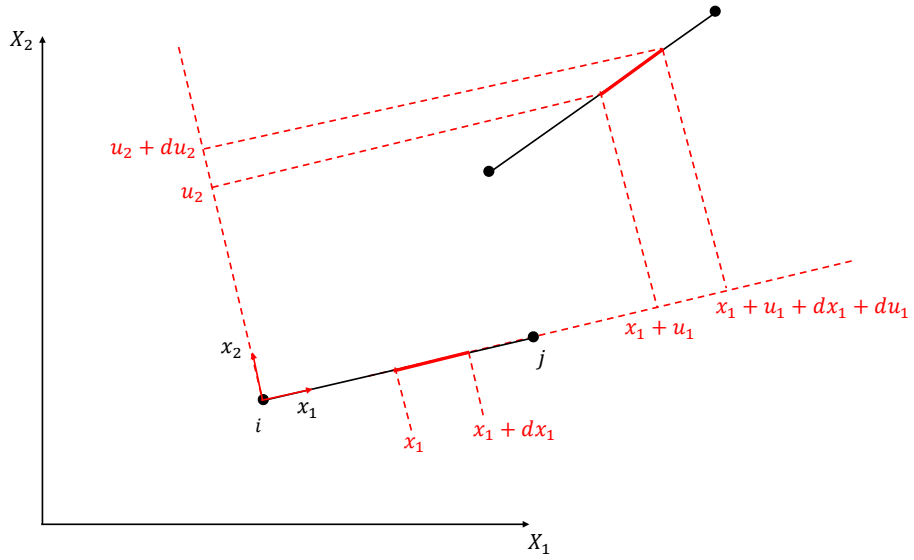

Figure 2.3: Schematic representation of a deforming 2D bar element. The infinitesimal slice of the element is shown in its reference (black) and deformed (red) configurations. The quantities u_1, u_2 and their variations $\mathrm{d}u_1, \mathrm{d}u_2$ represent the displacement field used to derive the Green–Lagrange strain E_e and its first variation δE_e in the nonlinear formulation of the internal virtual work.

Then the element contributions written directly in global DOFs are

$$\boxed{\mathbf{f}^e_{\text{int}}(\mathbf{u}) = S_e\, A_e\, L_e\, \widetilde{\mathbf{g}}(\mathbf{u})} \tag{2.74}$$

$$\boxed{\mathbf{K}_e(\mathbf{u}) = E\, A_e\, L_e\, \widetilde{\mathbf{g}}(\mathbf{u})\, \widetilde{\mathbf{g}}(\mathbf{u})^T \;+\; S_e\, A_e\, L_e\, \mathbf{B}_2.} \tag{2.75}$$

With your corrected operators

$$\mathbf{B}_e = \frac{1}{L_e}\begin{bmatrix} -1 & 0 & 1 & 0 \\ 0 & -1 & 0 & 1 \end{bmatrix}, \quad \mathbf{B}_1 = \frac{1}{L_e}\begin{bmatrix} -1 & 0 & 1 & 0 \end{bmatrix}, \quad \mathbf{B}_2 = \frac{1}{L_e^2}\begin{bmatrix} 1 & 0 & -1 & 0 \\ 0 & 1 & 0 & -1 \\ -1 & 0 & 1 & 0 \\ 0 & -1 & 0 & 1 \end{bmatrix},$$

the strain and its variation used in the implementation are precisely

$$E_e = \mathbf{B}_1\, \mathbf{u}_e + \tfrac{1}{2}\, \mathbf{u}_e^T \mathbf{B}_2 \mathbf{u}_e, \qquad \delta E_e = \left(\mathbf{B}_1^T + \mathbf{B}_2 \mathbf{u}_e\right)^T \delta \mathbf{u}_e,$$

leading to (2.70)–(2.75).

Generalisation to the 3D case

In three dimensions, each bar element connects two nodes i and j with undeformed coordinates $\mathbf{X}_i$ and $\mathbf{X}_j$, and current coordinates $\mathbf{x}_i = \mathbf{X}_i + \mathbf{u}_i$, $\mathbf{x}_j = \mathbf{X}_j + \mathbf{u}_j$. The

local direction vector and its unit form are defined as

$$\mathbf{l}_e = \mathbf{x}_j - \mathbf{x}_i, \qquad \mathbf{n}_e = \frac{\mathbf{l}_e}{\|\mathbf{l}_e\|}, \qquad L_e = \|\mathbf{l}_e\|.$$

The Green–Lagrange axial strain for the 3D bar reads

$$E_e = \frac{1}{2}\left(\mathbf{n}_e \cdot \mathbf{n}_e - 1\right) = \frac{1}{2L_0^2}\left[(\mathbf{x}_j - \mathbf{x}_i)\cdot(\mathbf{x}_j - \mathbf{x}_i) - (\mathbf{X}_j - \mathbf{X}_i)\cdot(\mathbf{X}_j - \mathbf{X}_i)\right], \quad (2.76)$$

which, linearised with respect to the nodal displacements, gives

$$\delta E_e = \frac{1}{L_e}\,\mathbf{n}_e^T\,\delta(\mathbf{u}_j - \mathbf{u}_i) = \mathbf{B}_e\,\delta\mathbf{u}_e, \qquad \mathbf{B}_e = \frac{1}{L_e}\begin{bmatrix}-\mathbf{n}_e^T & \mathbf{n}_e^T\end{bmatrix}. \quad (2.77)$$

The element internal virtual work is then

$$\delta W_{\text{int}}^e = \int_0^{L_e} A_e\,S_e\,\delta E_e\,\mathrm{d}x \simeq A_e\,L_e\,S_e\,\mathbf{B}_e\,\delta\mathbf{u}_e, \quad (2.78)$$

from which the element internal force vector follows as

$$\boxed{\mathbf{f}_{\text{int}}^e = A_e\,L_e\,S_e\,\mathbf{B}_e^T = A_e\,L_e\,E\,E_e\,\mathbf{B}_e^T,} \quad (2.79)$$

where E is the Young's modulus.
Linearising (2.79) with respect to $\mathbf{u}_e$ gives the consistent tangent matrix:

$$\boxed{\mathbf{K}_e = A_e\,E\,L_e\,\mathbf{B}_e^T\mathbf{B}_e + A_e\,S_e\,L_e\,\mathbf{G}_e,} \quad (2.80)$$

where the first term is the material stiffness, and the second term is the geometric stiffness, with

$$\mathbf{G}_e = \frac{1}{L_e}\begin{bmatrix}\mathbf{I} - \mathbf{n}_e\mathbf{n}_e^T & -(\mathbf{I} - \mathbf{n}_e\mathbf{n}_e^T)\\ -(\mathbf{I} - \mathbf{n}_e\mathbf{n}_e^T) & \mathbf{I} - \mathbf{n}_e\mathbf{n}_e^T\end{bmatrix}. \quad (2.81)$$

This formulation maintains the same structure as the 2D derivation and allows direct extension to general three–dimensional truss or bar networks. It represents the foundation upon which the dynamic bar–and–hinge solver was constructed and later extended to complex origami topologies.

2.7.2 Implementation of the 3D static framework in MATLAB

The three–dimensional static version of the framework, complete with the assembly of the internal forces derived from the expressions introduced in Section 2.5 and solved using the algorithms presented in Section 2.6, was implemented as a stand–alone finite element code developed in MATLAB. The framework performs a total Lagrangian nonlinear analysis based on Green–Lagrange strains and second Piola–Kirchhoff stresses for the bar elements, combined with rotational spring models for bending and folding hinges. It allows the simulation of generic bar–and–hinge assemblies in three dimensions, with automatic computation of the tangent stiffness matrix and full Newton–Raphson, Arc–Length, and MGDCM solvers for static equilibrium.

Framework structure. The developed code is organised into five main blocks:

1. **Pre–processing.** The script defines material constants (E, ν, t), geometry, and connectivity matrices for nodes, elements, and panels. The code automatically constructs the panel centres, bending hinges, and folding hinges, and computes cross–sectional areas based on geometric proportions.

2. **Assembly operators.** Element connectivity and hinge panels are expanded into assembly matrices that map local element quantities to the global finite element vectors and matrices. Hinge lengths and reference dihedral angles are computed directly from the undeformed geometry.

3. **Constitutive definitions.** Each bar element follows a Green–Lagrange strain formulation, with internal forces and tangent stiffness matrices evaluated as Eq. 2.79 and Eq. 2.80. Rotational springs for bending and folding hinges are introduced through moment–rotation laws defined by three stiffness regions (as defined in Section 2.5.6), whose tangent stiffness and internal moments are computed at each iteration.

4. **Global assembly and boundary conditions.** The global tangent stiffness matrix $\mathbf{K}_t$ and internal force vector $\mathbf{F}_i$ are obtained by assembling the contributions of all bars and rotational springs. Displacement boundary conditions and external forces are applied through index vectors.

5. **Nonlinear solution.** The equilibrium equations are solved incrementally using one of three available strategies: Newton–Raphson, Arc–Length, or MGDCM. Each iteration updates the global displacements and load factor λ until the residual force norm satisfies a specified tolerance. The framework also tracks internal energies of bars, bending and folding springs, and the external work for convergence and verification.

The implementation is designed for modularity, allowing straightforward substitution of constitutive laws or solution strategies. The framework serves as the foundation for the later dynamic extension described in Section 3.7.4.

2.7.3 Transition to dynamic formulation and deployment analysis

The quasi–static framework developed in this chapter provides the theoretical basis for reduced–order modeling of foldable structures through coupled bar and rotational hinge elements. Its formulation of stiffness matrices, equilibrium relations,

and energy consistency enables efficient simulation of large deformations while preserving the essential mechanical behavior of origami assemblies. Numerical demonstrations of this quasi-static framework are present on different case studies in Chapter 5.
The next chapter extends this formulation to include inertial and damping effects, introducing a dynamic bar–and–hinge framework capable of capturing transient deployment, oscillations, and post-deployment response. This transition marks the progression from static characterization to a full dynamic analysis environment, forming the foundation for the creation of the reduced order dynamical framework presented in this dissertation.

Chapter 3

Dynamic formulation of the bar–and–hinge model

3.1 Introduction

The quasi–static bar–and–hinge formulation described in Chapter 2 provides an efficient reduced–order framework for analysing large–displacement folding and deployment of origami–inspired structures. However, many structural responses of interest, such as deployment, transient oscillations, or impacts, require a dynamic extension capable of capturing inertial and damping effects in addition to the geometric nonlinearities. The dynamic version of the bar–and–hinge method presented here builds upon the quasi–static energy framework and extends it to time–dependent motion through Hamilton's principle.
In this formulation, each node of the bar–and–hinge network is endowed with translational degrees of freedom and a lumped mass that represents the combined contribution of the adjacent facets. Bars are treated as rigid mass–carrying links that resist axial deformation, while rotational hinges introduce localized bending or folding compliance. The resulting system of equations of motion couples inertia, damping, and nonlinear internal forces arising from both bars and hinges.

3.1.1 Scope and assumptions

The following assumptions define the dynamic framework:

- Bars are axially deformable but otherwise rigid in rotation and shear.
- Hinges are torsional springs capable of large rotations; their moment–angle laws are defined by the same constitutive models introduced in Section 2.5.6.
- Material damping is represented by proportional (Rayleigh) damping, while numerical dissipation is introduced by the integration algorithm.

- The system is conservative in the absence of external forcing and damping, such that total mechanical energy is preserved under exact integration.

The purpose of this chapter is to derive the governing equations of motion from first principles, define the mass and damping matrices, and describe the time–integration algorithm used for transient simulation. Formulations that remain identical to those in the quasi–static analysis (such as the element strain energy and stiffness definitions) are only briefly recalled, whereas new expressions, kinetic energy, mass matrix, damping and time integration, are presented in full detail.

3.2 Governing equations of motion

The equations of motion of the bar–and–hinge system follow directly from Hamilton's principle, which requires the action integral

$$\mathcal{S} = \int_{t_0}^{t_1} (T - U_{\text{int}} + W_{\text{ext}})\, \mathrm{d}t \tag{3.1}$$

to be stationary with respect to admissible variations of the nodal displacements $\delta\mathbf{u}(t)$ that vanish at the temporal boundaries t_0 and t_1.
The variation of the action reads

$$\delta\mathcal{S} = \int_{t_0}^{t_1} (\delta T - \delta U_{\text{int}} + \delta W_{\text{ext}})\, \mathrm{d}t = 0. \tag{3.2}$$

The kinetic energy of the discrete system is

$$T = \tfrac{1}{2}\, \dot{\mathbf{u}}^{\mathrm{T}} \mathbf{M}\, \dot{\mathbf{u}}, \tag{3.3}$$

where $\mathbf{M}$ is the global mass matrix and $\dot{\mathbf{u}}$ is the vector of nodal velocities. The internal potential energy U_{int} and the external potential W_{ext} have the same form as in Eq. (2.4) of the quasi–static formulation.
Taking the first variation of Eq. (3.3) yields

$$\delta T = \dot{\mathbf{u}}^{\mathrm{T}} \mathbf{M}\, \delta\dot{\mathbf{u}} = -\,\delta\mathbf{u}^{\mathrm{T}} \mathbf{M}\, \ddot{\mathbf{u}} + \frac{\mathrm{d}}{\mathrm{d}t}\big(\dot{\mathbf{u}}^{\mathrm{T}} \mathbf{M}\, \delta\mathbf{u}\big), \tag{3.4}$$

where the second equality follows from integration by parts in time, and the boundary term vanishes due to $\delta\mathbf{u}(t_0) = \delta\mathbf{u}(t_1) = \mathbf{0}$.
Substituting Eqs. (3.4) and (2.10) into Eq. (3.2) gives

$$\int_{t_0}^{t_1} \delta\mathbf{u}^{\mathrm{T}} \Big(-\,\mathbf{M}\, \ddot{\mathbf{u}} - \,\mathbf{R}(\mathbf{u}) + \mathbf{F}_{\text{ext}}(t) \Big) \mathrm{d}t = 0. \tag{3.5}$$

Since $\delta\mathbf{u}$ is arbitrary within (t_0, t_1), the governing equations of motion follow as

$$\boxed{\mathbf{M}\,\ddot{\mathbf{u}} + \mathbf{R}(\mathbf{u}) = \mathbf{F}_{\text{ext}}(t).} \tag{3.6}$$

To account for damping effects, a viscous term proportional to velocity is added, leading to the final form:

$$\boxed{\mathbf{M}\,\ddot{\mathbf{u}} + \mathbf{C}\,\dot{\mathbf{u}} + \mathbf{R}(\mathbf{u}) = \mathbf{F}_{\text{ext}}(t),} \tag{3.7}$$

where $\mathbf{C}$ is the global damping matrix. Equation (3.7) represents the complete nonlinear dynamic equilibrium for the bar–and–hinge model. The residual vector $\mathbf{R}(\mathbf{u})$ retains the same definition as in Eq. (2.6), i.e.

$$\mathbf{R}(\mathbf{u}) = \mathbf{T}_{\text{bar}}(\mathbf{u}) + \mathbf{T}_{\text{spr}}(\mathbf{u}) - \mathbf{F}_{\text{ext}}.$$

3.2.1 Interpretation

Equation (3.7) generalises the quasi–static formulation to dynamic problems by introducing inertia and damping forces. The term $\mathbf{M}\ddot{\mathbf{u}}$ represents the nodal inertial forces, $\mathbf{C}\dot{\mathbf{u}}$ the viscous damping forces, and $\mathbf{R}(\mathbf{u})$ the nonlinear internal elastic forces originating from bars and rotational hinges. This formulation remains fully compatible with the previously defined element libraries and stiffness matrices, ensuring that the transition from quasi–static to dynamic simulation requires only the additional definition of $\mathbf{M}$ and $\mathbf{C}$.
The subsequent section derives the consistent mass matrix formulation for the bar–and–hinge network, including both lumped and distributed representations, and introduces the damping model used for dynamic analysis.

3.3 Kinetic energy and mass matrix formulation

The introduction of inertia in the bar–and–hinge framework requires the consistent definition of the system's kinetic energy and the corresponding discrete mass matrix. The kinetic energy is expressed in terms of the translational degrees of freedom of the nodal network, while the bars are assumed to remain axially deformable but rotationally rigid.

3.3.1 Kinetic energy of the discrete system

The total kinetic energy of the origami structure is obtained as the sum of the translational kinetic energies associated with all n nodes of the bar–and–hinge network:

$$T = \frac{1}{2}\sum_{a=1}^{n} m_a\,\dot{\mathbf{u}}_a^{\mathrm{T}}\dot{\mathbf{u}}_a = \tfrac{1}{2}\dot{\mathbf{u}}^{\mathrm{T}}\mathbf{M}\dot{\mathbf{u}}, \tag{3.8}$$

where m_a is the equivalent lumped mass assigned to node a, $\dot{\mathbf{u}}_a$ is its velocity vector, and $\mathbf{M}$ is the global mass matrix of order $3n$. The matrix $\mathbf{M}$ is symmetric and positive–definite, ensuring that the system's kinetic energy remains strictly non–negative during motion.

3.3.2 Elemental mass contribution and lumped formulation

Each panel of the origami structure is modeled as a homogeneous, isotropic sheet of thickness t, area A_p, and material density ρ. The total mass of the panel is therefore

$$m_p = \rho\, t\, A_p. \tag{3.9}$$

Following the N5B8 discretization scheme [62], each quadrilateral panel is represented by five nodes: four at the corners and one at the centre. Because corner and centre nodes have different topological connectivities (each outer node is shared by three bars, whereas the central node connects to four), the nodal mass distribution must account for this uneven participation to preserve both mass conservation and dynamic consistency.

A *topology–aware lumped mass model* is therefore adopted. The total panel mass m_p is first divided uniformly among the five nodes ($m_p/5$ per node), and then weighted by the number of bars incident to each node:

$$m_{\text{out}} = \frac{m_p}{5} \cdot \frac{1}{3} = \frac{m_p}{15}, \qquad m_{\text{cent}} = \frac{m_p}{5} \cdot \frac{1}{4} = \frac{m_p}{20}. \tag{3.10}$$

This approach ensures that outer nodes, which connect to a larger number of neighboring panels, naturally carry a higher effective mass contribution ($m_{\text{out}} = 1.33\, m_{\text{cent}}$).

3.3.3 Local and global mass assembly

Each bar element e connecting two nodes i and j (either outer or central) receives a local diagonal mass matrix in its local coordinate system:

$$\mathbf{M}^{(e)}_{\text{local}} = \begin{bmatrix} m_\alpha\, \mathbf{I}_3 & \mathbf{0}_3 \\ \mathbf{0}_3 & m_\beta\, \mathbf{I}_3 \end{bmatrix}, \qquad (\alpha, \beta) \in \{\text{o}, \text{c}\}, \tag{3.11}$$

where $\mathbf{I}_3$ is the 3×3 identity matrix and m_α, m_β denote the corresponding nodal masses assigned from Eq. (3.10).

The global mass matrix is then assembled by summing all elemental contributions:

$$\mathbf{M} = \text{diag}[m_1,\, m_1,\, m_1,\, m_2,\, m_2,\, m_2, \ldots, m_n,\, m_n,\, m_n], \tag{3.12}$$

resulting in a fully diagonal (lumped) matrix that preserves total system mass while maintaining numerical sparsity and stability for large-scale transient simulations.

This topology–aware lumped model provides an optimal compromise between accuracy and efficiency: it retains the correct total mass and relative nodal weighting dictated by structural connectivity, yet avoids the computational cost and coupling introduced by a fully consistent mass matrix.

3.3.4 Energy consistency and momentum conservation

Both the consistent and lumped mass definitions satisfy the fundamental energy equivalence:

$$\frac{\partial T}{\partial \dot{\mathbf{u}}} = \mathbf{M}\dot{\mathbf{u}}, \qquad \frac{\partial^2 T}{\partial \dot{\mathbf{u}}^2} = \mathbf{M}, \tag{3.13}$$

which ensures that the inertial forces $\mathbf{M}\ddot{\mathbf{u}}$ are exactly conjugate to the nodal accelerations $\ddot{\mathbf{u}}$. The momentum of the discrete system is defined as

$$\mathbf{p} = \mathbf{M}\dot{\mathbf{u}}, \tag{3.14}$$

and satisfies global conservation in the absence of external and damping forces:

$$\frac{\mathrm{d}\mathbf{p}}{\mathrm{d}t} = \mathbf{F}_{\text{ext}} - \mathbf{C}\dot{\mathbf{u}} - \mathbf{R}(\mathbf{u}). \tag{3.15}$$

3.3.5 Assembly of the global mass matrix

The global mass matrix is assembled by summing the contributions of all panels or bars that share a common node. Denoting by $\mathbf{P}_p$ the Boolean extractor matrix that maps the panel degrees of freedom to the global vector $\mathbf{u}$, the assembled matrix reads

$$\mathbf{M} = \sum_{p=1}^{N_p} \mathbf{P}_p^{\mathrm{T}} \mathbf{M}_p \mathbf{P}_p. \tag{3.16}$$

When the lumped definition is used, this summation simply accumulates scalar contributions to the diagonal terms corresponding to each node.

3.3.6 Coupling with the stiffness formulation

The dynamic bar–and–hinge formulation remains fully compatible with the stiffness operators derived in Chapter 2. The inertial term $\mathbf{M}\ddot{\mathbf{u}}$ is computed at each time step and added to the residual equilibrium equation

$$\mathbf{R}_{\text{dyn}}(\mathbf{u}, \dot{\mathbf{u}}, \ddot{\mathbf{u}}, t) = \mathbf{M}\ddot{\mathbf{u}} + \mathbf{C}\dot{\mathbf{u}} + \mathbf{R}(\mathbf{u}) - \mathbf{F}_{\text{ext}}(t) = \mathbf{0}. \tag{3.17}$$

This expression provides the governing residual for transient analyses, with $\mathbf{M}$ is computed once at initialization and reused throughout the time–integration process.

3.4 Time integration scheme

The governing dynamic equilibrium equation of the bar–and–hinge system is expressed as

$$\mathbf{M}\,\ddot{\mathbf{u}} + \mathbf{C}\,\dot{\mathbf{u}} + \mathbf{R}(\mathbf{u}) = \mathbf{F}_{\text{ext}}(t), \tag{3.18}$$

where $\mathbf{M}$ and $\mathbf{C}$ are the global mass and damping matrices, $\mathbf{R}(\mathbf{u})$ is the nonlinear internal force vector, and $\mathbf{F}_{\text{ext}}(t)$ is the time–dependent external force vector. The numerical solution of Eq. (3.18) requires the adoption of a time–integration algorithm that advances the kinematic variables $\mathbf{u}$, $\dot{\mathbf{u}}$, and $\ddot{\mathbf{u}}$ in discrete time steps Δt, ensuring both numerical stability and controlled dissipation.
The dynamic formulation we present supports three families of integration schemes:

1. an explicit *Forward Euler* scheme for small systems or short transient responses,

2. the implicit *Newmark–β* method for unconditionally stable integration,

3. the *Hilber–Hughes–Taylor* α (HHT–α) algorithm for improved numerical damping of high–frequency oscillations.

All schemes operate within the same residual–based iterative structure and employ the consistent tangent stiffness $\mathbf{K}(\mathbf{u}) = \mathbf{K}_{\text{bar}} + \mathbf{K}_{\text{spr}}$ derived in Chapter 2.

3.4.1 Explicit Forward Euler integration

The simplest time–integration approach updates nodal states using explicit finite differences:

$$\dot{\mathbf{u}}_{n+1} = \dot{\mathbf{u}}_n + \Delta t\,\ddot{\mathbf{u}}_n, \tag{3.19}$$

$$\mathbf{u}_{n+1} = \mathbf{u}_n + \Delta t\,\dot{\mathbf{u}}_n. \tag{3.20}$$

The acceleration $\ddot{\mathbf{u}}_n$ is obtained directly from Eq. (3.18):

$$\ddot{\mathbf{u}}_n = \mathbf{M}^{-1}(\mathbf{F}_{\text{ext},n} - \mathbf{C}\dot{\mathbf{u}}_n - \mathbf{R}(\mathbf{u}_n))\,. \tag{3.21}$$

Although computationally inexpensive, the explicit Euler scheme is only conditionally stable, with a maximum stable time increment approximately satisfying $\Delta t < 2/\omega_{\max}$, where $\omega_{\max}$ is the largest natural frequency of the system. For origami structures with high stiffness contrasts, this condition can be restrictive, motivating the use of implicit integration.

3.4.2 Implicit Newmark–β method

The implicit Newmark–β method provides unconditional stability and second–order accuracy for linear systems, making it the preferred baseline for dynamic folding simulations. The kinematic update relations are

$$\mathbf{u}_{n+1} = \mathbf{u}_n + \Delta t\, \dot{\mathbf{u}}_n + \tfrac{1}{2}\Delta t^2 \left[(1-2\beta)\ddot{\mathbf{u}}_n + 2\beta\, \ddot{\mathbf{u}}_{n+1}\right], \tag{3.22}$$

$$\dot{\mathbf{u}}_{n+1} = \dot{\mathbf{u}}_n + \Delta t \left[(1-\gamma)\ddot{\mathbf{u}}_n + \gamma\, \ddot{\mathbf{u}}_{n+1}\right], \tag{3.23}$$

where β and γ are integration parameters controlling stability and numerical damping. Typical choices are $\beta = 1/4$ and $\gamma = 1/2$, corresponding to the average–acceleration scheme.
Substituting Eqs. (3.22)–(3.23) into Eq. (3.18) gives the residual equilibrium at time t_{n+1}:

$$\mathbf{R}_{n+1} = \mathbf{M}\,\ddot{\mathbf{u}}_{n+1} + \mathbf{C}\,\dot{\mathbf{u}}_{n+1} + \mathbf{R}(\mathbf{u}_{n+1}) - \mathbf{F}_{\text{ext},n+1} = \mathbf{0}. \tag{3.24}$$

The corresponding effective stiffness matrix for the Newton iteration is

$$\mathbf{K}_{\text{eff}} = \frac{1}{\beta\Delta t^2}\mathbf{M} + \frac{\gamma}{\beta\Delta t}\mathbf{C} + \mathbf{K}(\mathbf{u}_{n+1}^{(i)}), \tag{3.25}$$

where $\mathbf{K}(\mathbf{u}_{n+1}^{(i)})$ is the tangent stiffness evaluated at the current iteration i.

3.4.3 Hilber–Hughes–Taylor (HHT–α) method

The HHT–α algorithm generalizes Newmark–β by introducing a controlled algorithmic dissipation of high–frequency components while preserving second–order accuracy for the low–frequency response [154]. The modified dynamic equilibrium is evaluated at an intermediate point $t_{n+1-\alpha} = t_{n+1} - \alpha\Delta t$:

$$\mathbf{M}\,\ddot{\mathbf{u}}_{n+1-\alpha} + \mathbf{C}\,\dot{\mathbf{u}}_{n+1-\alpha} + \mathbf{R}(\mathbf{u}_{n+1-\alpha}) = \mathbf{F}_{\text{ext},n+1-\alpha}, \tag{3.26}$$

with

$$\begin{aligned} \mathbf{R}(\mathbf{u}_{n+1-\alpha}) &= (1-\alpha)\,\mathbf{R}(\mathbf{u}_{n+1}) + \alpha\,\mathbf{R}(\mathbf{u}_n), \\ \mathbf{F}_{\text{ext},\,n+1-\alpha} &= (1-\alpha)\,\mathbf{F}_{\text{ext},\,n+1} + \alpha\,\mathbf{F}_{\text{ext},\,n}. \end{aligned} \tag{3.27}$$

The algorithm reduces to the classical Newmark–β scheme for $\alpha = 0$. Typical parameters ensuring unconditional stability and optimal dissipation are $\alpha = -0.1$, $\beta = (1-\alpha)^2/4$, and $\gamma = 1/2 - \alpha$.
The corresponding effective stiffness matrix solved at each iteration is

$$\mathbf{K}_{\text{eff}} = (1-\alpha)\left[\frac{1}{\beta\Delta t^2}\mathbf{M} + \frac{\gamma}{\beta\Delta t}\mathbf{C}\right] + (1-\alpha)\,\mathbf{K}(\mathbf{u}_{n+1}^{(i)}). \tag{3.28}$$

At convergence, the algorithm guarantees controlled numerical damping of spurious oscillations without distorting the physically meaningful response.

3.4.4 Algorithmic implementation

For clarity, the complete dynamic time–integration loop implemented in the dynamic framework is presented below with both algorithms.

Algorithm 2 Explicit dynamic time–integration (Forward Euler)

Input: initial state $\mathbf{u}_0$, $\dot{\mathbf{u}}_0$; mass $\mathbf{M}$, damping $\mathbf{C}$, internal force $\mathbf{R}(\cdot)$, external load $\mathbf{F}_{\text{ext},n}$; time step Δt; number of steps N_{steps}.
$n \leftarrow 0$
while $n < N_{\text{steps}}$ **do**
    Assemble internal forces at t_n: $\mathbf{R}_n \leftarrow \mathbf{R}(\mathbf{u}_n)$.
    Compute acceleration at t_n: $\ddot{\mathbf{u}}_n = \mathbf{M}^{-1}\big(\mathbf{F}_{\text{ext},n} - \mathbf{C}\,\dot{\mathbf{u}}_n - \mathbf{R}_n\big)$.
    Update velocity (Forward Euler): $\dot{\mathbf{u}}_{n+1} = \dot{\mathbf{u}}_n + \Delta t\,\ddot{\mathbf{u}}_n$.
    Update displacement (Forward Euler): $\mathbf{u}_{n+1} = \mathbf{u}_n + \Delta t\,\dot{\mathbf{u}}_n$.
    Post–update acceleration at t_{n+1} (for storage/output):
    $\mathbf{R}_{n+1} \leftarrow \mathbf{R}(\mathbf{u}_{n+1}), \quad \ddot{\mathbf{u}}_{n+1} = \mathbf{M}^{-1}\big(\mathbf{F}_{\text{ext},n+1} - \mathbf{C}\,\dot{\mathbf{u}}_{n+1} - \mathbf{R}_{n+1}\big)$.
    $n \leftarrow n + 1$
end while
Output: time histories $\{\mathbf{u}_n, \dot{\mathbf{u}}_n, \ddot{\mathbf{u}}_n\}_{n=0}^{N_{\text{steps}}}$.

Algorithm 3 Implicit dynamic time–integration (HHT–α/Newmark–β)

Input: initial state $\mathbf{u}_0$, $\dot{\mathbf{u}}_0$, $\ddot{\mathbf{u}}_0$; mass $\mathbf{M}$, damping $\mathbf{C}$, internal force $\mathbf{R}(\cdot)$, external load $\mathbf{F}_{\text{ext},n}$; parameters (α, β, γ); tolerance ε; maximum iterations $N_{\text{it,max}}$; number of steps N_{steps}.
$n \leftarrow 0$
while $n < N_{\text{steps}}$ **do**
    Predictor: $\mathbf{u}_{n+1}^{(0)} = \mathbf{u}_n + \Delta t\,\dot{\mathbf{u}}_n + \frac{1}{2}\Delta t^2(1-2\beta)\ddot{\mathbf{u}}_n, \quad \dot{\mathbf{u}}_{n+1}^{(0)} = \dot{\mathbf{u}}_n + \Delta t(1-\gamma)\ddot{\mathbf{u}}_n$.
    $i \leftarrow 0$
    repeat ▷ until convergence or $i = N_{\text{it,max}}$
        Compute residual $\mathbf{R}_{n+1-\alpha}^{(i)}$ and tangent $\mathbf{K}_{\text{eff}}^{(i)}$.
        Solve: $\mathbf{K}_{\text{eff}}^{(i)}\Delta\mathbf{u} = -\mathbf{R}_{n+1-\alpha}^{(i)}$.
        Update: $\mathbf{u}_{n+1}^{(i+1)} = \mathbf{u}_{n+1}^{(i)} + \Delta\mathbf{u}$.
        Check: if $\|\mathbf{R}_{n+1-\alpha}^{(i)}\|/\|\mathbf{F}_{\text{ext},n+1}\| < \varepsilon$ then break.
        $i \leftarrow i + 1$
    until false
    Accept step: update $\ddot{\mathbf{u}}_{n+1}$ and $\dot{\mathbf{u}}_{n+1}$ (Newmark relations).
    $n \leftarrow n + 1$
end while
Output: time histories $\{\mathbf{u}_n, \dot{\mathbf{u}}_n, \ddot{\mathbf{u}}_n\}$.

3.4.5 Stability and algorithmic dissipation

The HHT–α method provides unconditional stability for $-1/3 \leq \alpha \leq 0$ and introduces algorithmic damping proportional to α. The spectral radius of the amplification matrix, ρ_∞, controlling high–frequency decay, is related to α by

$$\rho_\infty = \frac{1 - 2\alpha}{1 + 2\alpha}. \tag{3.29}$$

Typical values $\alpha = -0.1$ to -0.15 correspond to $\rho_\infty \approx 0.8$, which ensures rapid attenuation of non–physical oscillations without distorting the low–frequency dynamics of folding.

3.4.6 Remarks on numerical implementation

The implicit integration algorithms are implemented in the dynamic framework using the same element–level modularity as the quasi–static solver. Each time step requires the assembly of $\mathbf{M}$, $\mathbf{C}$, and $\mathbf{K}(\mathbf{u})$, the computation of residual forces $\mathbf{R}_{n+1-\alpha}$, and the solution of a single linearized system. The global convergence tolerance ε is typically set to 10^{-6}, and adaptive time–stepping can be employed for strongly nonlinear events. This unified structure enables seamless transition between quasi–static continuation and fully dynamic transient analyses.

3.5 Damping model and energy dissipation

In addition to inertia and elastic restoring forces, the dynamic formulation requires the inclusion of energy–dissipating mechanisms to ensure numerical stability and to approximate material and structural damping effects. We introduce a linear viscous damping model, expressed in matrix form as

$$\mathbf{C}\,\dot{\mathbf{u}}, \tag{3.30}$$

where $\mathbf{C}$ is the global damping matrix and $\dot{\mathbf{u}}$ the nodal velocity vector. The damping term represents internal energy loss and provides critical damping control of spurious oscillations, especially during large folding–unfolding motions.

3.5.1 Rayleigh damping model

We model the global damping matrix using a Rayleigh (proportional) combination of the mass and stiffness matrices,

$$\mathbf{C} = \alpha_M\,\mathbf{M} + \beta_K\,\mathbf{K}, \tag{3.31}$$

where α_M and β_K are non–negative scalar coefficients defining the contribution of mass– and stiffness–proportional damping, respectively. The Rayleigh model offers

computational simplicity and ensures that the damping matrix remains symmetric and positive semi–definite.
The damping ratio ζ_i associated with the i–th vibration mode is given by

$$\zeta_i = \tfrac{1}{2}\left(\frac{\alpha_M}{\omega_i} + \beta_K\,\omega_i\right), \tag{3.32}$$

where ω_i is the natural frequency of the corresponding mode, obtained from the eigenvalue problem

$$\mathbf{K}\,\boldsymbol{\phi}_i = \omega_i^2\,\mathbf{M}\,\boldsymbol{\phi}_i. \tag{3.33}$$

By selecting two target frequencies ω_1 and ω_2 and their corresponding desired damping ratios ζ_1 and ζ_2, the coefficients α_M and β_K are obtained by solving

$$\begin{bmatrix} 1/(2\omega_1) & \omega_1/2 \\ 1/(2\omega_2) & \omega_2/2 \end{bmatrix} \begin{bmatrix} \alpha_M \\ \beta_K \end{bmatrix} = \begin{bmatrix} \zeta_1 \\ \zeta_2 \end{bmatrix}. \tag{3.34}$$

Typical damping levels used in our simulations range from $\zeta_i = 0.02$ to 0.05, corresponding to lightly damped thin–film structures. The resulting α_M and β_K coefficients are then directly substituted into Eq. (3.31) to construct $\mathbf{C}$ once at initialization.

3.5.2 Modal damping representation

When specific damping ratios are required for a limited number of vibration modes, a modal damping model can be employed. The global damping matrix is expressed as

$$\mathbf{C} = \boldsymbol{\Phi}\,\mathbf{C}_\xi\,\boldsymbol{\Phi}^{\mathrm{T}}, \tag{3.35}$$

where $\boldsymbol{\Phi} = [\boldsymbol{\phi}_1, \boldsymbol{\phi}_2, \dots]$ is the matrix of mass–orthonormal mode shapes satisfying $\boldsymbol{\Phi}^{\mathrm{T}}\mathbf{M}\boldsymbol{\Phi} = \mathbf{I}$, and $\mathbf{C}_\xi = 2\,\mathrm{diag}(\zeta_i\omega_i)$ is a diagonal matrix containing the modal damping constants. This formulation provides a more accurate representation of structural damping for selected modes but requires the solution of the eigenvalue problem Eq. (3.33), which increases computational cost. For most dynamic origami simulations, proportional damping according to Eq. (3.31) offers an adequate balance between accuracy and efficiency.

3.5.3 Energy dissipation and stability

The instantaneous mechanical energy of the discrete system is defined as

$$\mathcal{E}(t) = T + U_{\mathrm{int}} - W_{\mathrm{ext}} = \tfrac{1}{2}\dot{\mathbf{u}}^{\mathrm{T}}\mathbf{M}\dot{\mathbf{u}} + U_{\mathrm{int}}(\mathbf{u}) - \mathbf{F}_{\mathrm{ext}}^{\mathrm{T}}\mathbf{u}. \tag{3.36}$$

Taking its time derivative and substituting the equations of motion Eq. (3.7), we obtain

$$\frac{\mathrm{d}\mathcal{E}}{\mathrm{d}t} = -\,\dot{\mathbf{u}}^{\mathrm{T}}\mathbf{C}\dot{\mathbf{u}}, \tag{3.37}$$

which demonstrates that the damping term always removes energy from the system and that $\mathcal{E}(t)$ decreases monotonically when no external work is applied. Equation (3.37) guarantees unconditional stability in the absence of external excitation provided that $\mathbf{C}$ is positive semi–definite.

3.5.4 Interpretation

The damping model defined above reproduces the global dissipative behaviour of flexible, foldable structures without introducing artificial stiffness. In dynamic folding and deployment simulations, it prevents non–physical high–frequency oscillations of the nodes and ensures that the total mechanical energy remains bounded. The damping parameters (α_M, β_K) are calibrated to achieve realistic transient responses that replicate the viscoelastic characteristics of lightweight composite laminates and textile–reinforced substrates typically used in origami–based systems.

3.6 Energy conservation and stability analysis

A central requirement for the dynamic bar–and–hinge formulation is that the time–integration algorithm maintains stable behaviour while providing controlled algorithmic dissipation. We therefore analyse the evolution of the discrete total energy under HHT–α integration and establish its unconditional stability for a proper choice of parameters (α, β, γ).

3.6.1 Discrete mechanical energy

The instantaneous mechanical energy of the system is defined as

$$\mathcal{E}(t) = T(t) + U_{\text{int}}(t) - W_{\text{ext}}(t) = \tfrac{1}{2}\dot{\mathbf{u}}^{\mathrm{T}}\mathbf{M}\dot{\mathbf{u}} + U_{\text{int}}(\mathbf{u}) - \mathbf{F}_{\text{ext}}^{\mathrm{T}}\mathbf{u}. \tag{3.38}$$

During exact integration, $\mathcal{E}$ remains constant for a conservative system. In a discrete time–stepping algorithm, the variation of $\mathcal{E}$ between two successive steps defines the numerical energy error.
Using the HHT–α equilibrium Eq. (3.39), the discrete energy increment between t_n and t_{n+1} can be written as

$$\Delta\mathcal{E} = \mathcal{E}_{n+1} - \mathcal{E}_n = -\,(1+\alpha)\,\Delta t\,\dot{\mathbf{u}}_{n+1-\alpha}^{\mathrm{T}}\,\mathbf{C}\,\dot{\mathbf{u}}_{n+1-\alpha} - \alpha\,\Delta t\,\dot{\mathbf{u}}_{n+1-\alpha}^{\mathrm{T}}\,\mathbf{K}\,\dot{\mathbf{u}}_{n+1-\alpha}, \tag{3.39}$$

where $\dot{\mathbf{u}}_{n+1-\alpha} = (1-\alpha)\dot{\mathbf{u}}_{n+1} + \alpha\,\dot{\mathbf{u}}_n$. The first term represents physical damping, while the second term accounts for algorithmic dissipation introduced by $\alpha < 0$. For $\alpha = 0$, the method reduces to the classical Newmark–β scheme, which conserves energy exactly in the absence of damping.

3.6.2 Unconditional stability

The HHT–α method is unconditionally stable for linear systems when the parameters satisfy

$$\alpha \in [-1/3,\, 0], \qquad \beta \geq \tfrac{1}{4}(1+\alpha)^2, \qquad \gamma = \tfrac{1}{2} + \alpha. \tag{3.40}$$

These relations ensure that the amplification matrix of the integration scheme has a spectral radius less than or equal to unity for any time step Δt, making the algorithm suitable for large–scale nonlinear dynamic problems with severe stiffness contrasts, such as origami folding and snap–through events.

3.6.3 Algorithmic dissipation control

The parameter α determines the level of numerical damping applied to high–frequency components of the response. Its effect is quantified by the spectral radius at infinity ρ_∞, related to α by

$$\alpha = \frac{1-\rho_\infty}{1+\rho_\infty}. \tag{3.41}$$

For $\rho_\infty = 1$, no algorithmic dissipation is introduced and the scheme is energy–conserving. Typical choices $\rho_\infty = 0.8$–0.9 yield mild damping of spurious oscillations without affecting the low–frequency response of the structure.
The combination of Eqs. (3.39)–(3.41) demonstrates that the total mechanical energy decreases monotonically for $\alpha < 0$, ensuring robust stability even for highly nonlinear transient events.

3.6.4 Discussion

In dynamic folding simulations, energy consistency and monotonic dissipation are fundamental to avoid artificial oscillations and divergence near contact–like configurations. The present formulation achieves this by combining a consistent mass representation, a Rayleigh damping matrix, and the HHT–α integration algorithm. The result is a numerically stable and physically consistent scheme capable of capturing both quasi–static and transient nonlinear behaviours of origami structures.

3.7 Numerical behaviour, convergence, and transition to applications

3.7.1 Iterative convergence characteristics

The nonlinear coupling between bar elongations and hinge rotations requires iterative correction within each time step. Convergence is monitored through the

relative residual norm

$$\frac{\|\mathbf{R}_{n+1-\alpha}^{(i)}\|}{\|\mathbf{F}_{\text{ext},\,n+1}\|} < \varepsilon_{\text{dyn}},$$

with ε_{dyn} typically between 10^{-4} and 10^{-6}. The convergence rate is quadratic near equilibrium owing to the consistent tangent matrix $\mathbf{K}_{\text{eff}}$ defined in Eq. (3.28). For strongly nonlinear events, such as multiple fold activations or snap–through transitions, adaptive control of the time step Δt ensures robust and efficient performance.

3.7.2 Influence of model and integration parameters

The stability and accuracy of the dynamic simulation depend on both physical and numerical parameters:

- **Mass scaling.** The lumped mass distribution controls the natural frequencies of the model and should reflect realistic areal densities of the substrate.
- **Damping.** Parameters α_M and β_K are tuned to reproduce observed decay rates without suppressing global dynamics.
- **Time step.** The integration time step Δt must satisfy $\Delta t < 0.2\,T_{\text{min}}$, where T_{min} is the smallest characteristic vibration period of the system, ensuring sufficient temporal resolution.
- **Integration parameters.** For typical values $\alpha = -0.1$, $\beta = 0.25(1+\alpha)^2$, and $\gamma = 0.5 + \alpha$, the algorithm achieves stable, accurate results with mild high–frequency damping.

Sensitivity analyses performed during development confirmed that the dynamic response converges with mesh refinement and that the integration parameters affect only the transient damping of high–frequency components, without altering the overall folding kinematics.

3.7.3 Computational performance

The computational cost of the dynamic bar–and–hinge formulation scales linearly with the number of degrees of freedom due to the sparse and banded structure of the global matrices $\mathbf{M}$, $\mathbf{C}$, and $\mathbf{K}$. This efficiency allows time–accurate simulation of large deployable systems with complex folding topologies.

3.7.4 Dynamic bar–and–hinge framework implementation in MATLAB

The MATLAB framework for the dynamic bar-and-hinge method implements the equations of motion derived in Section 3.2. The equations are integrated in time

through the schemes described in Section 3.4. The implementation builds directly upon the 3D static framework, augmenting it with inertial effects and mass matrix contributions formulated in Section 3.3. The resulting code constitutes a general nonlinear dynamic solver for bar–and–hinge assemblies, written entirely in MATLAB.

Overview. The framework performs nonlinear dynamic simulations of 3D bar-and-hinge structures under arbitrary time–dependent loads. All material and geometric parameters (E, ν, t, ρ), together with nodal coordinates, element connectivity, and panel definitions, are read or generated during the pre–processing stage. At this level, the user also specifies the excitation function $F(t)$, the total simulation time, and the integration time step Δt, along with the preferred time–integration scheme. Three solvers are implemented and can be selected at runtime: *Forward Euler*, *Newmark–β*, and *HHT–α*.

Kinematic and constitutive formulation. The bar elements retain the total–Lagrangian Green–Lagrange strain formulation derived in the static framework. Internal forces and consistent tangent stiffness matrices are computed according to the same expressions used in Section 2.5, ensuring exact compatibility between static and dynamic analyses. Rotational spring elements model the bending and folding stiffness of the hinges through the nonlinear moment–rotation laws already defined, and their contributions are assembled together with those of the bar elements into the global internal force vector $\mathbf{F}_{\text{int}}$ and tangent matrix $\mathbf{K}_t$.

Mass matrix and inertial terms. The transition from the static to the dynamic framework is achieved by introducing a global mass matrix $\mathbf{M}$, consistently derived from the kinetic energy expression presented in Section 3.3. Element masses are distributed to the corresponding nodal degrees of freedom through assembly operators analogous to those used for stiffness. Inertial forces are then computed as $\mathbf{F}_{\text{in}} = \mathbf{M}\,\ddot{\mathbf{u}}$, and automatically included in the residual of the global equilibrium equations.

Time integration and solution procedure. Time discretisation of the equations of motion follows the general scheme described in Section 3.4. At each time step t_{n+1}, the global residual and effective tangent matrix are assembled according to the chosen algorithm:

- *Forward Euler* – a first–order explicit scheme for preliminary validation and small–scale problems;
- *Newmark–β* – an unconditionally stable implicit integrator based on constant–average acceleration ($\beta = 0.25$, $\gamma = 0.5$);

- *HHT–α* – a dissipative variant of Newmark's method, improving high–frequency numerical damping and stability.

For each step, the nonlinear equilibrium $\mathbf{R}_{n+1} = \mathbf{M}\,\ddot{\mathbf{u}}_{n+1} + \mathbf{F}_{\text{int}}(\mathbf{u}_{n+1}) - \mathbf{F}_{\text{ext}}(t_{n+1}) = 0$ is solved iteratively by a Newton–Raphson procedure until convergence in the residual norm. After convergence, the displacement, velocity, and acceleration vectors are updated and stored for post–processing.

Outputs and validation. The framework records the complete time history of nodal displacements, velocities, and accelerations, as well as the evolution of internal, kinetic, and external energies. These results are subsequently used to validate both the static and dynamic solvers. A detailed verification of the framework, including benchmark case studies and comparison against high–fidelity finite element simulations, is reported in Chapter 5.

3.7.5 Transition to dynamic applications

The dynamic framework derived in this chapter provides the foundation for the simulation of transient folding and deployment phenomena in origami–inspired systems. In the following chapter, the formulation is applied to representative geometries to analyse their dynamic response, including deployment speed, hinge moment evolution, and energy transfer between panels. These numerical studies demonstrate the capability of the developed model to predict the full time–dependent mechanics of foldable structures with high fidelity, bridging the gap between reduced–order analytical models and experimentally validated prototypes.

Chapter 4

Experimental activities and implementation of the bar–and–hinge framework

This chapter presents two main objectives: to introduce the experimental activities carried out throughout the research, and to describe the numerical bar–and–hinge frameworks developed for the analysis of origami-inspired structures. The experimental work was aimed at providing a physical basis for the definition and validation of the numerical model, while the static and dynamic frameworks, implemented in MATLAB, were conceived to reproduce and predict the observed mechanical behaviour.

The first part of the chapter presents the overall workflow adopted for experimental validation, with particular attention to the identification of the torsional stiffness of folding hinges. Determining an equivalent hinge stiffness from the intrinsic material properties represents a well-known challenge in bar–and–hinge modelling [62], and a dedicated experimental campaign (currently ongoing) has been therefore designed out to directly measure this parameter. This activity aims to provide both insight into the physical behaviour of the folds and the quantitative data required to calibrate the numerical framework.

The second part of the chapter describes the design and construction of a dedicated Mechanical Ground Support Equipment (MGSE) for the deployment of origami structures. The MGSE was developed to provide controlled boundary conditions and actuation for both quasi-static and dynamic tests. Its design process, which was guided by the numerical results obtained from the bar–and–hinge simulations carried out in MERLIN2, is presented in detail and represents a validation of the quasi-static bar and hinge results.

The third part introduces the computer–vision–based tracking algorithm developed to measure the kinematics of the origami prototypes during experimental testing. This system allows the automatic detection and tracking of key features on the

panels, providing time-resolved displacement data that can be directly compared with the results of the dynamic simulations.

Finally, the last section of the chapter summarises the implementation of the bar–and–hinge framework in MATLAB, in both its static and dynamic formulations. The underlying mathematical models are presented in Chapter 2 and 3, while this section focuses on the experimental workflow, and description of the computational implementation of the framework. The numerical results obtained with these formulations are validated in Chapter 5 through comparison with finite element simulations and the experimental data obtained following the procedure detailed in this chapter.

4.1

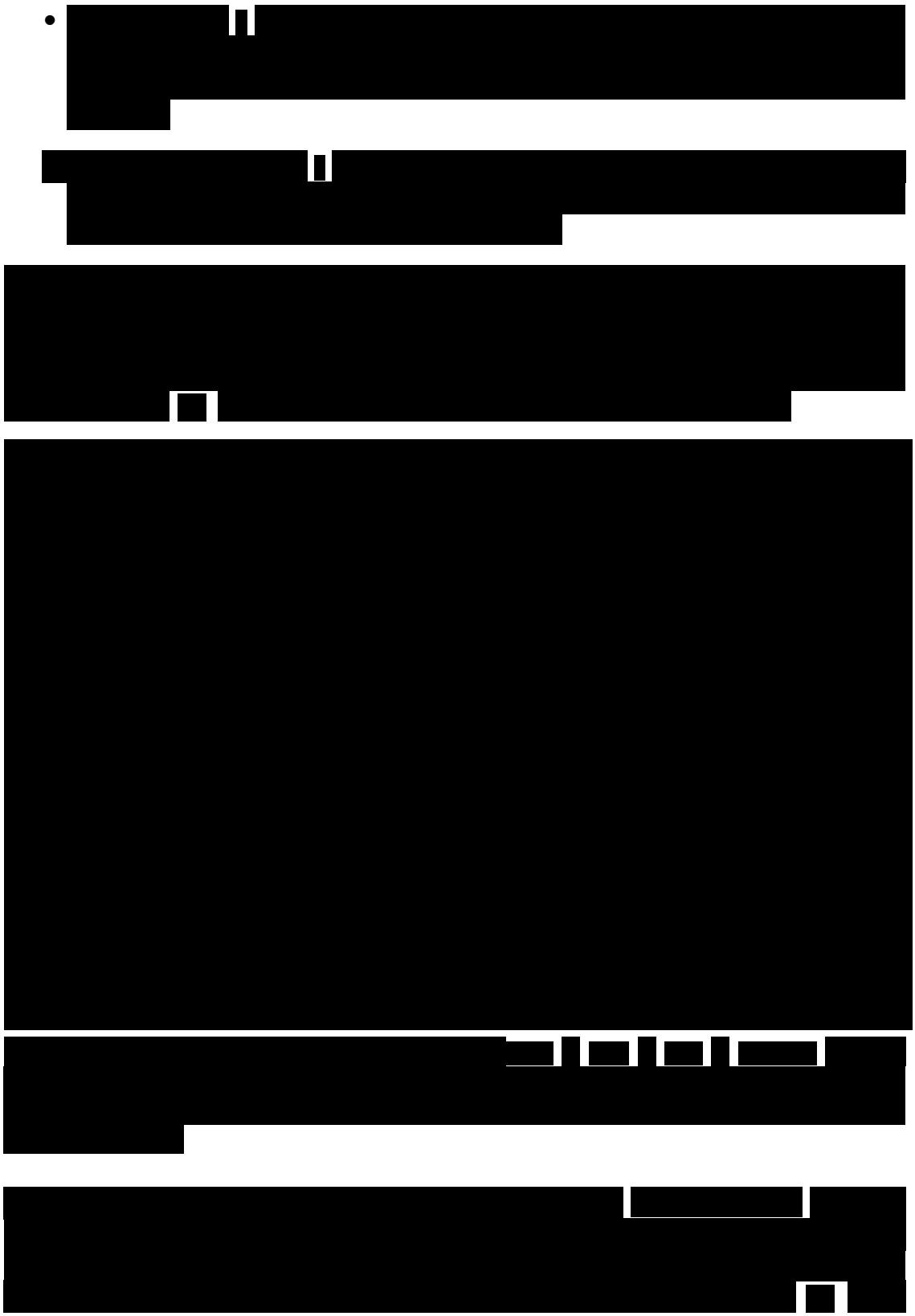

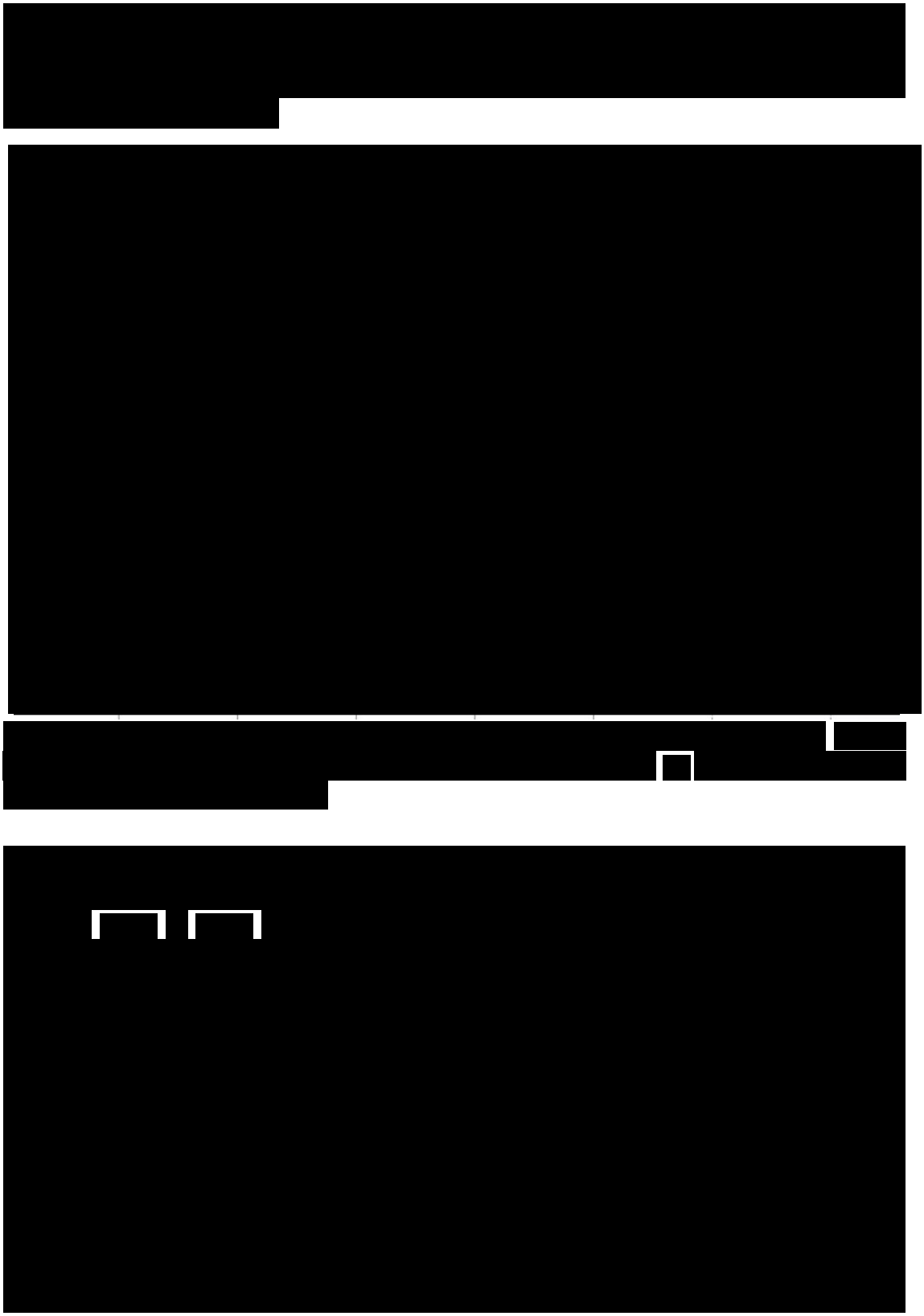

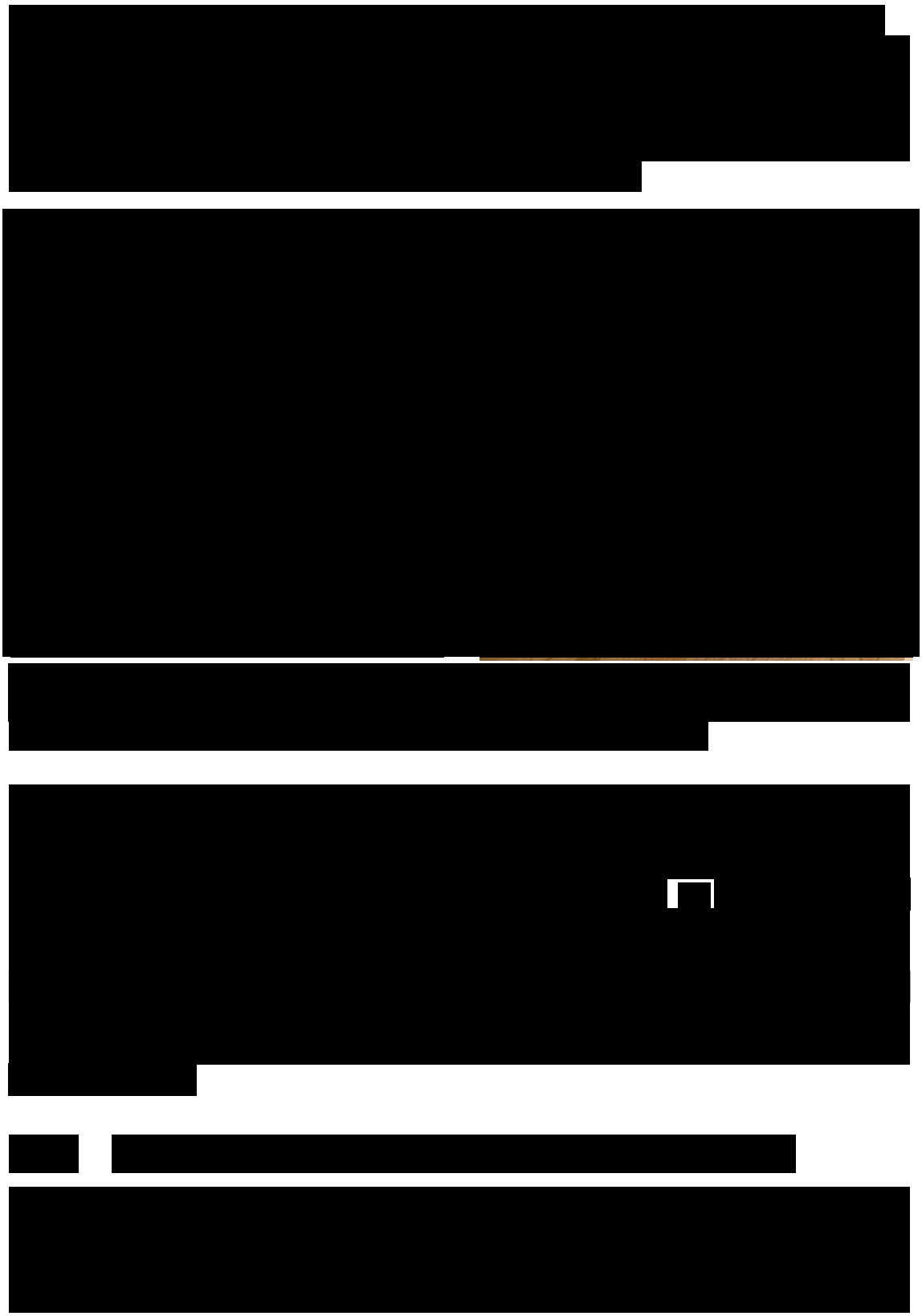

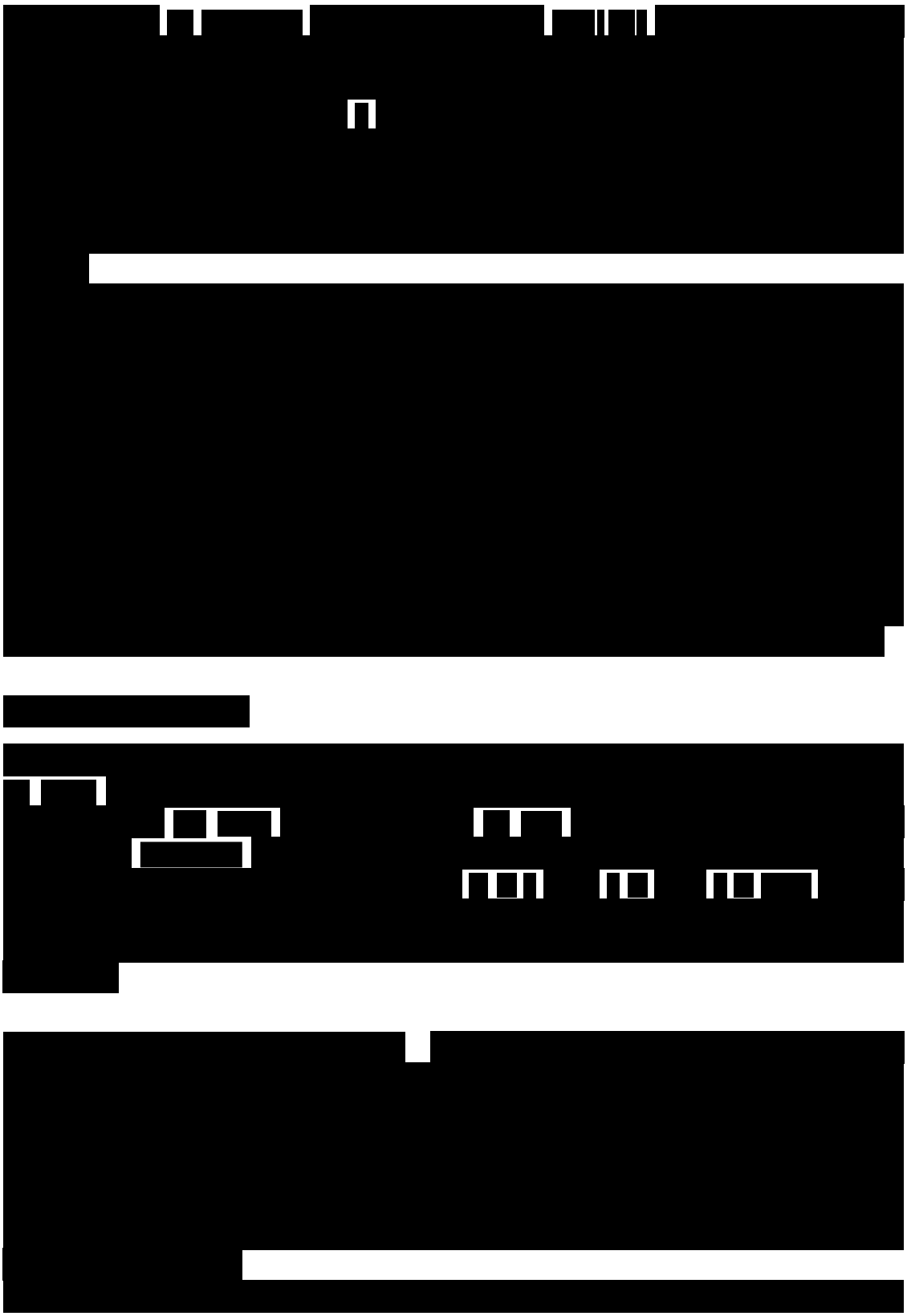

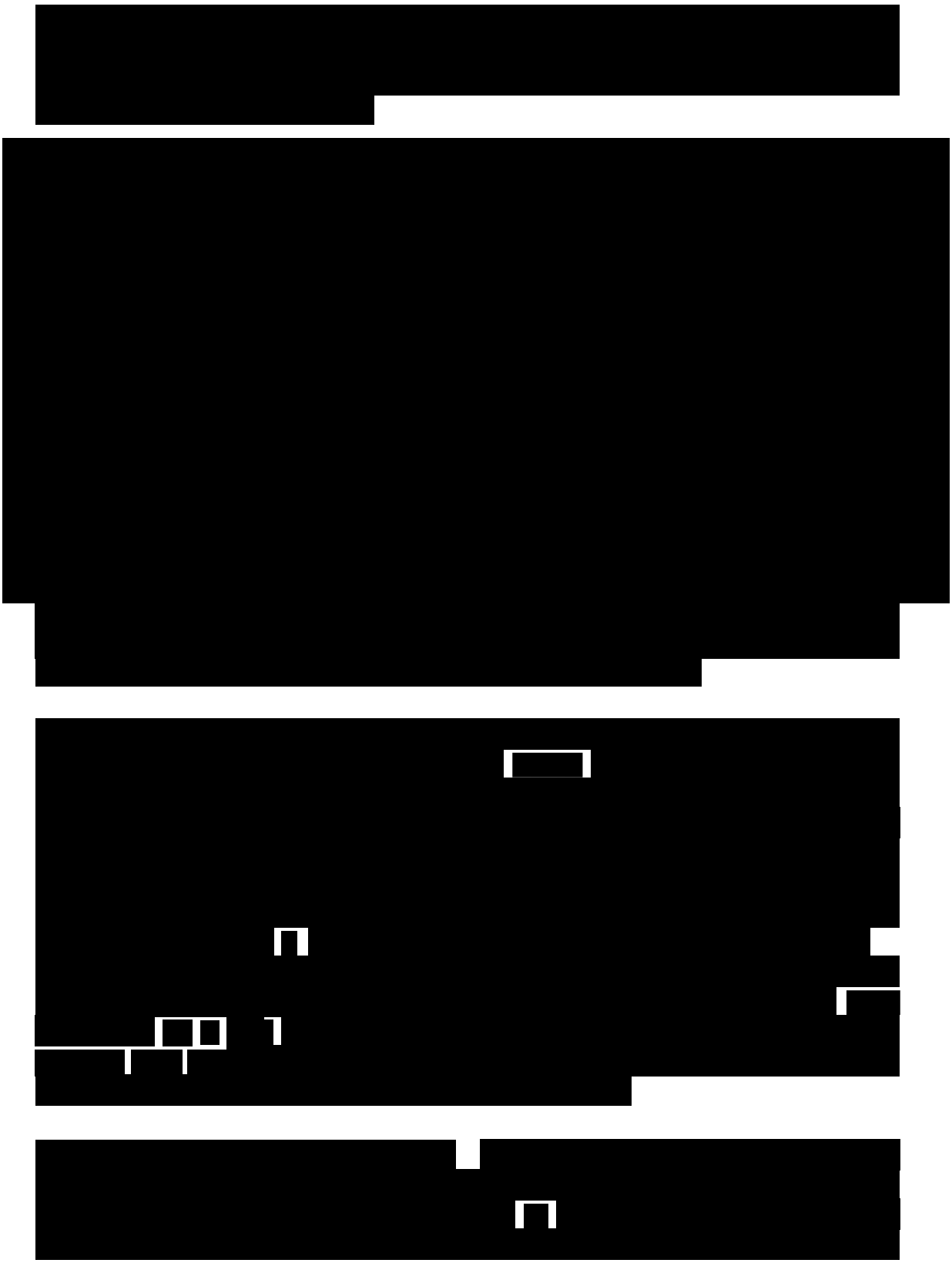

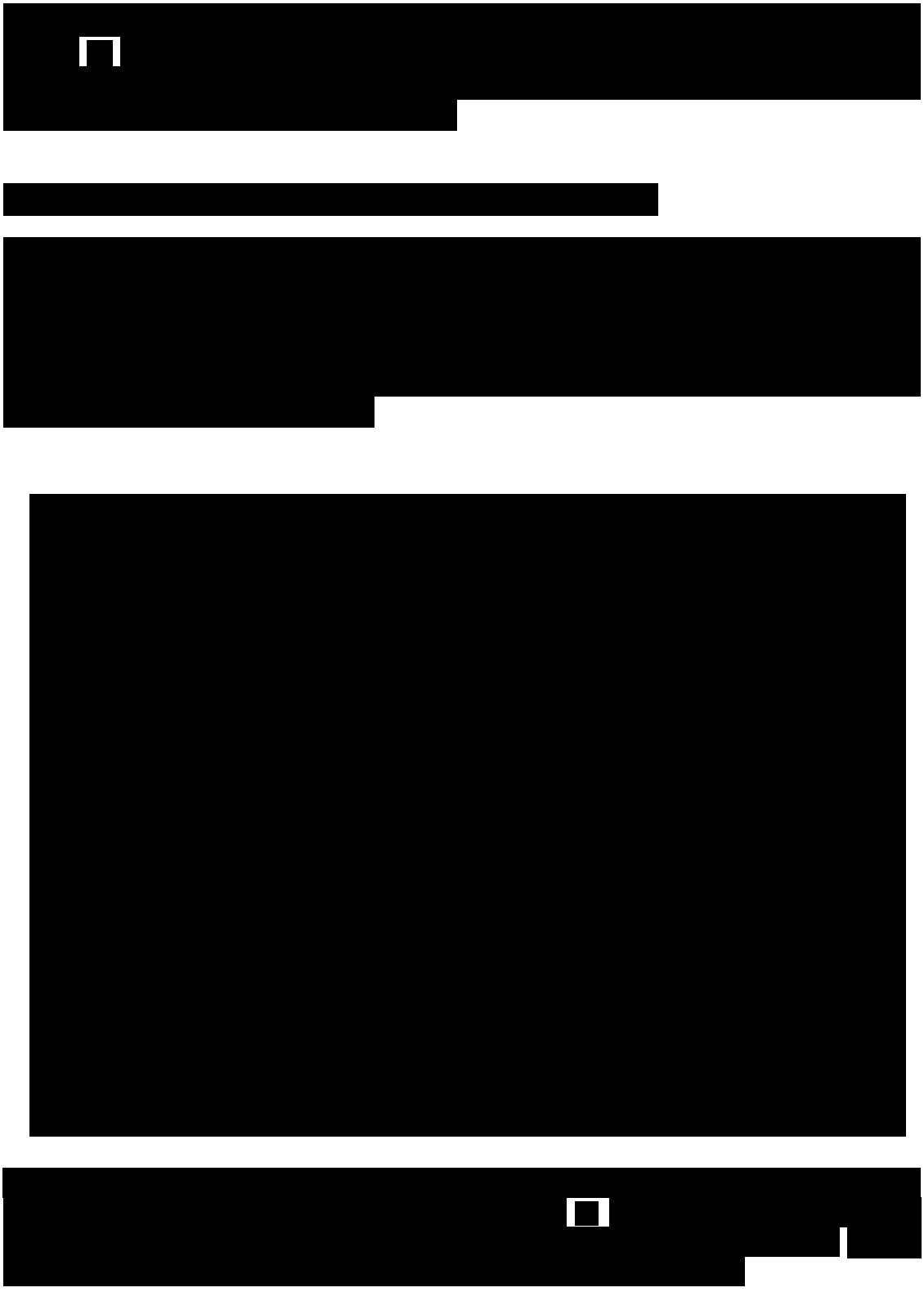

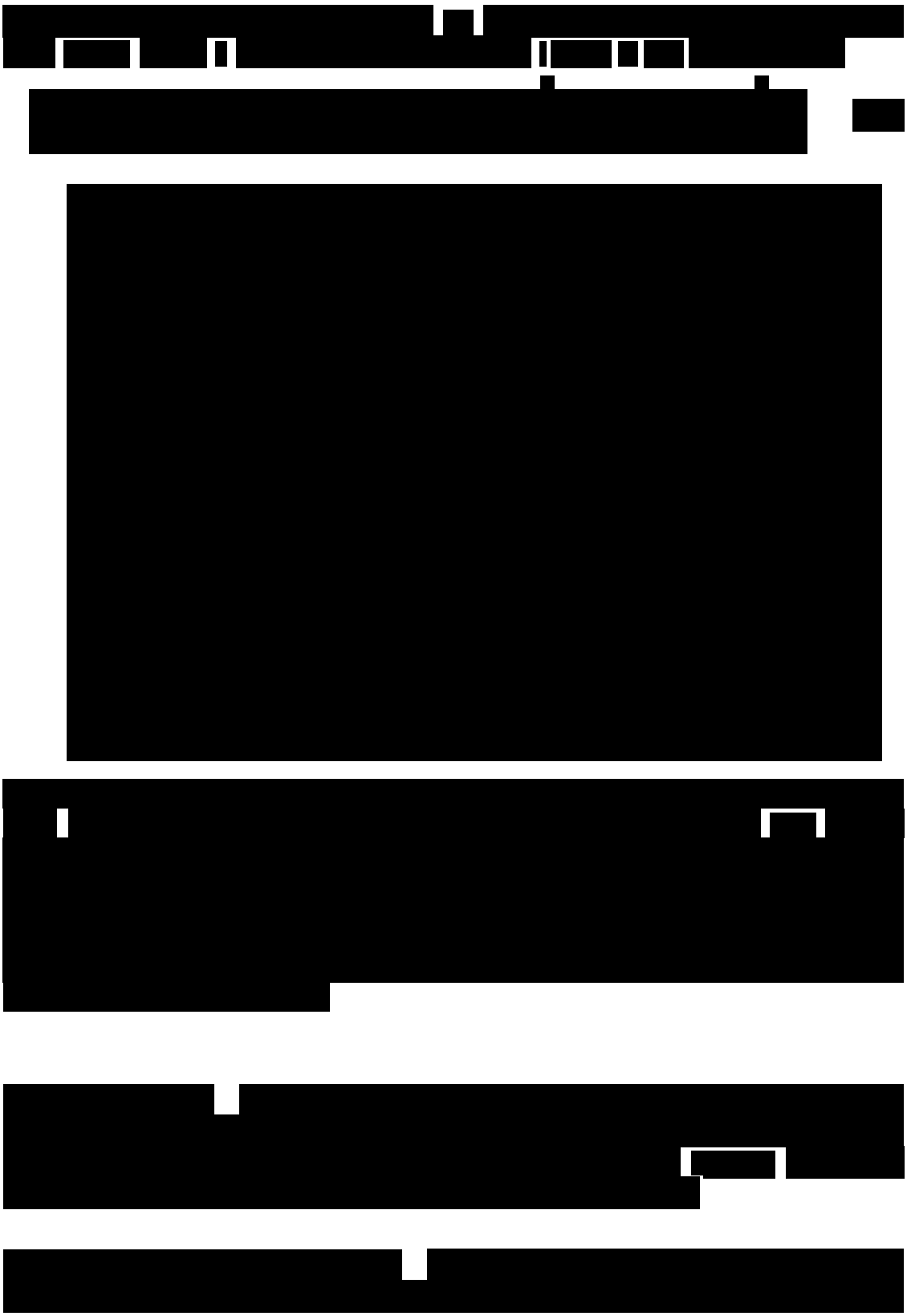

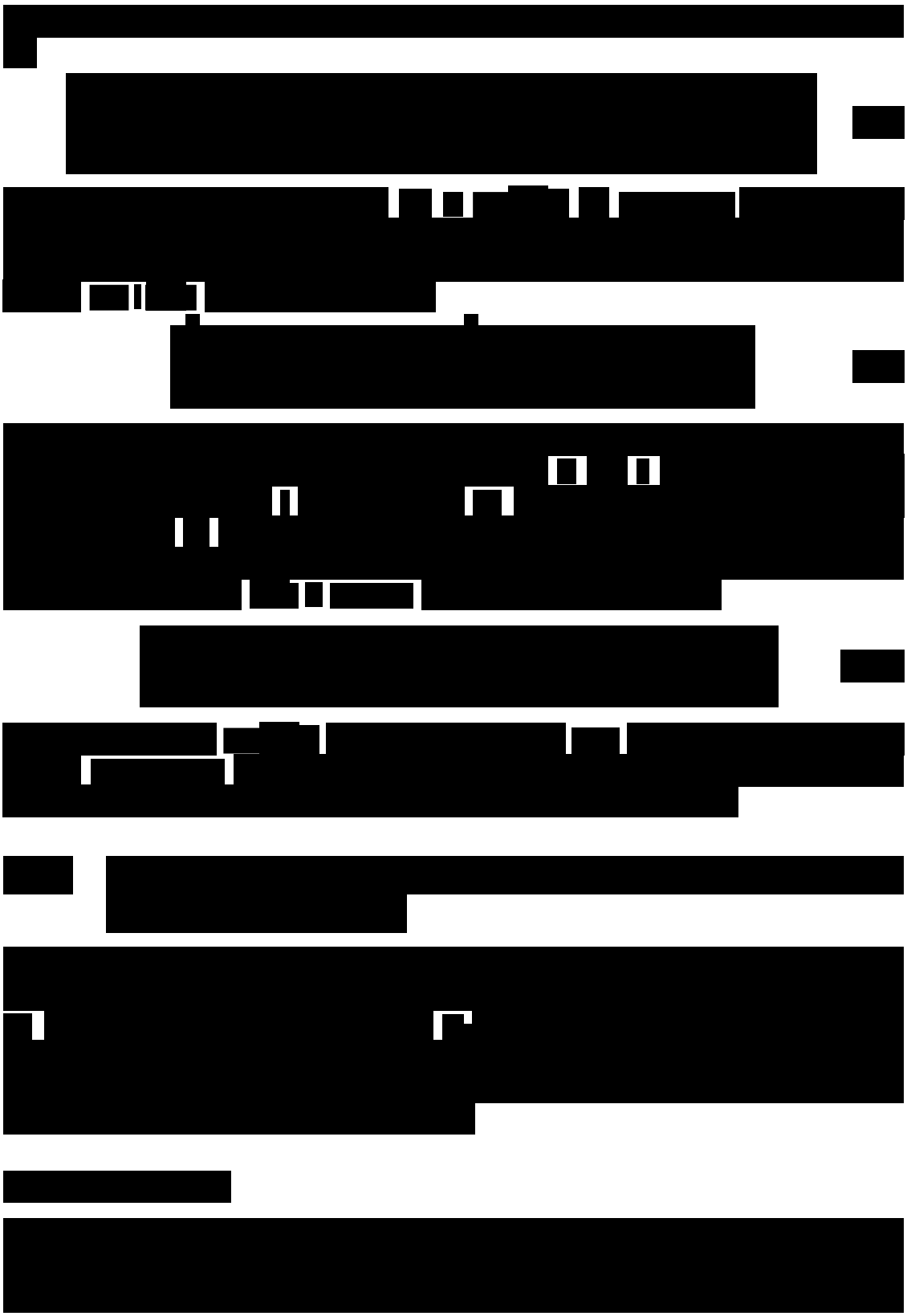

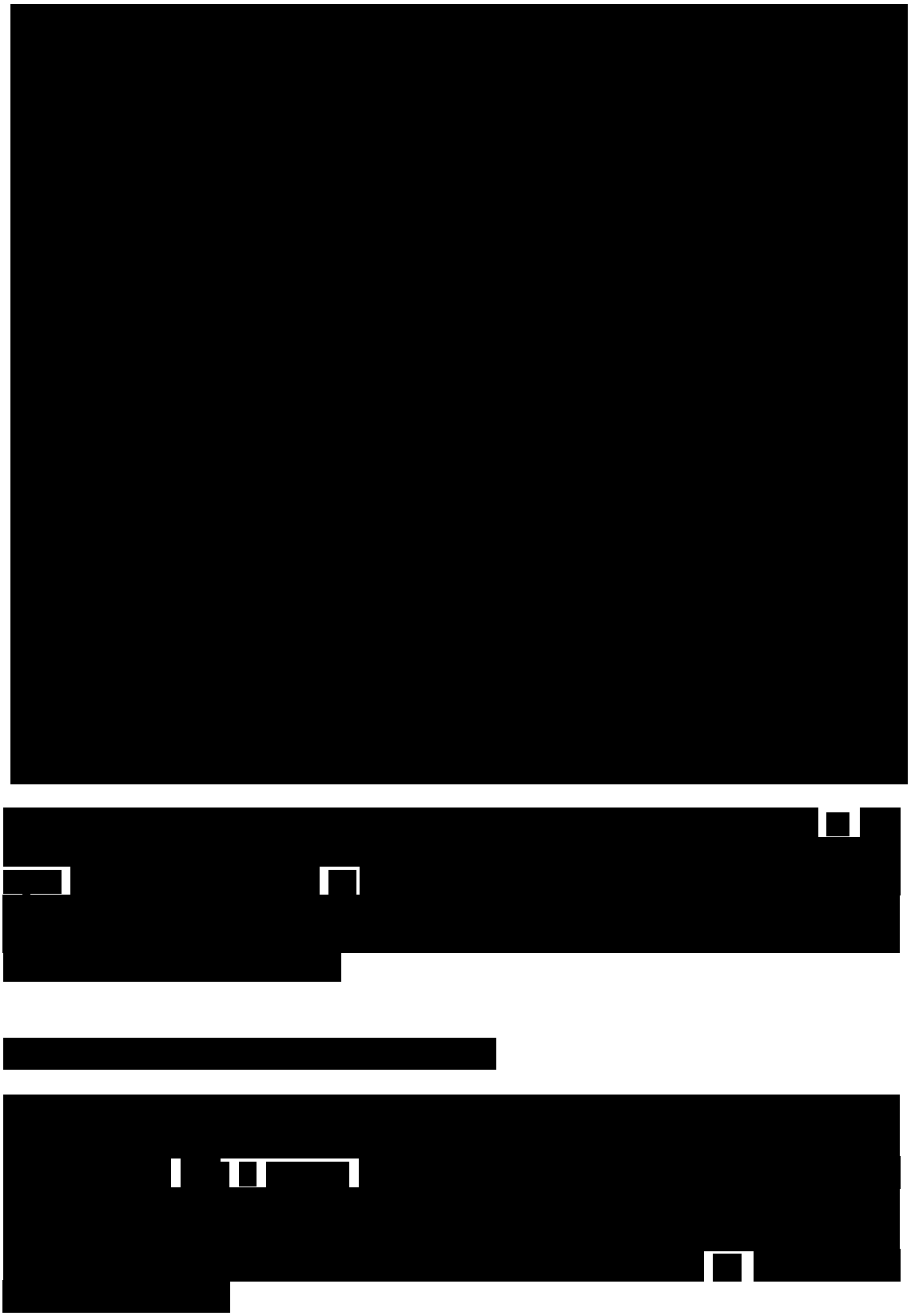

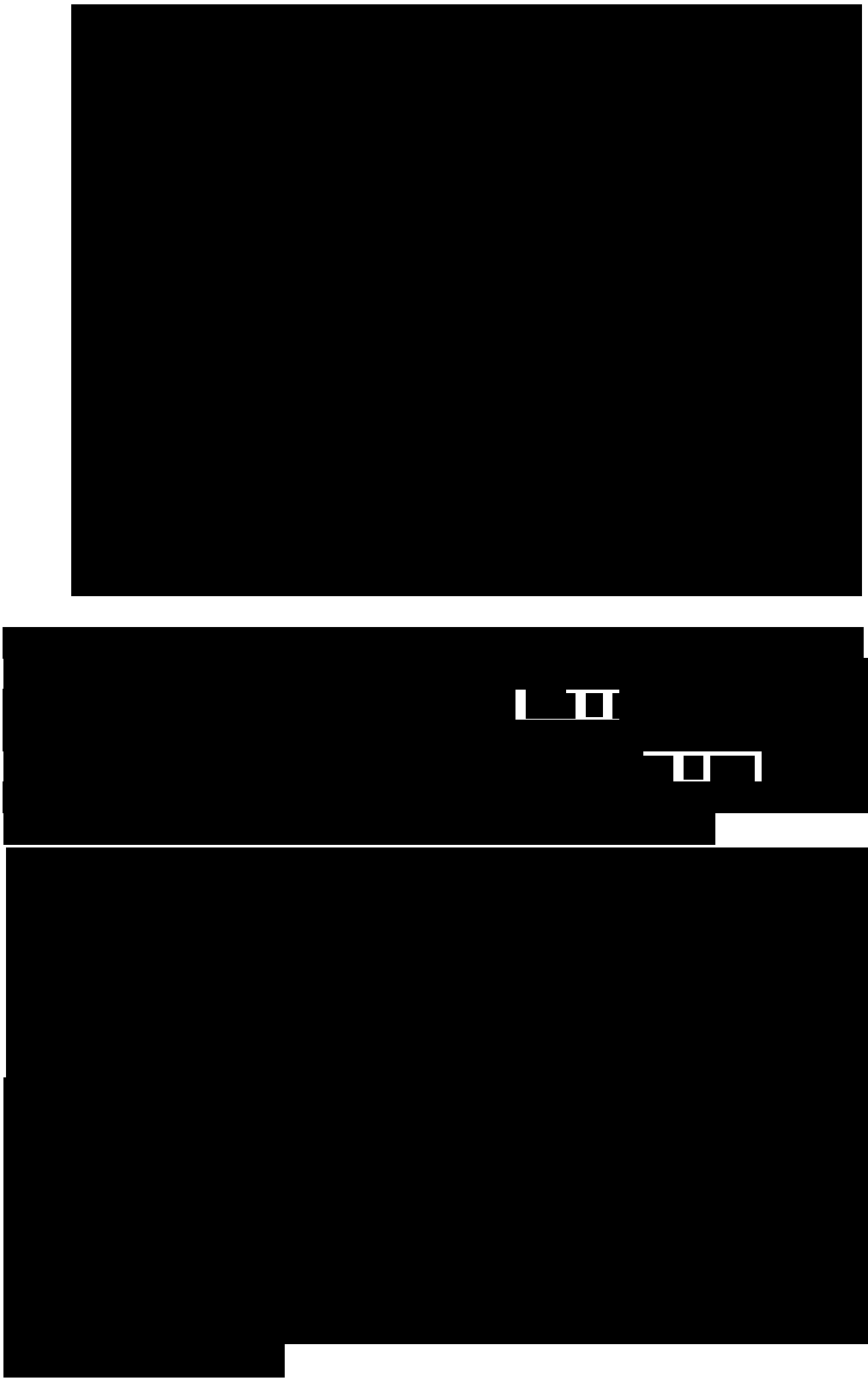

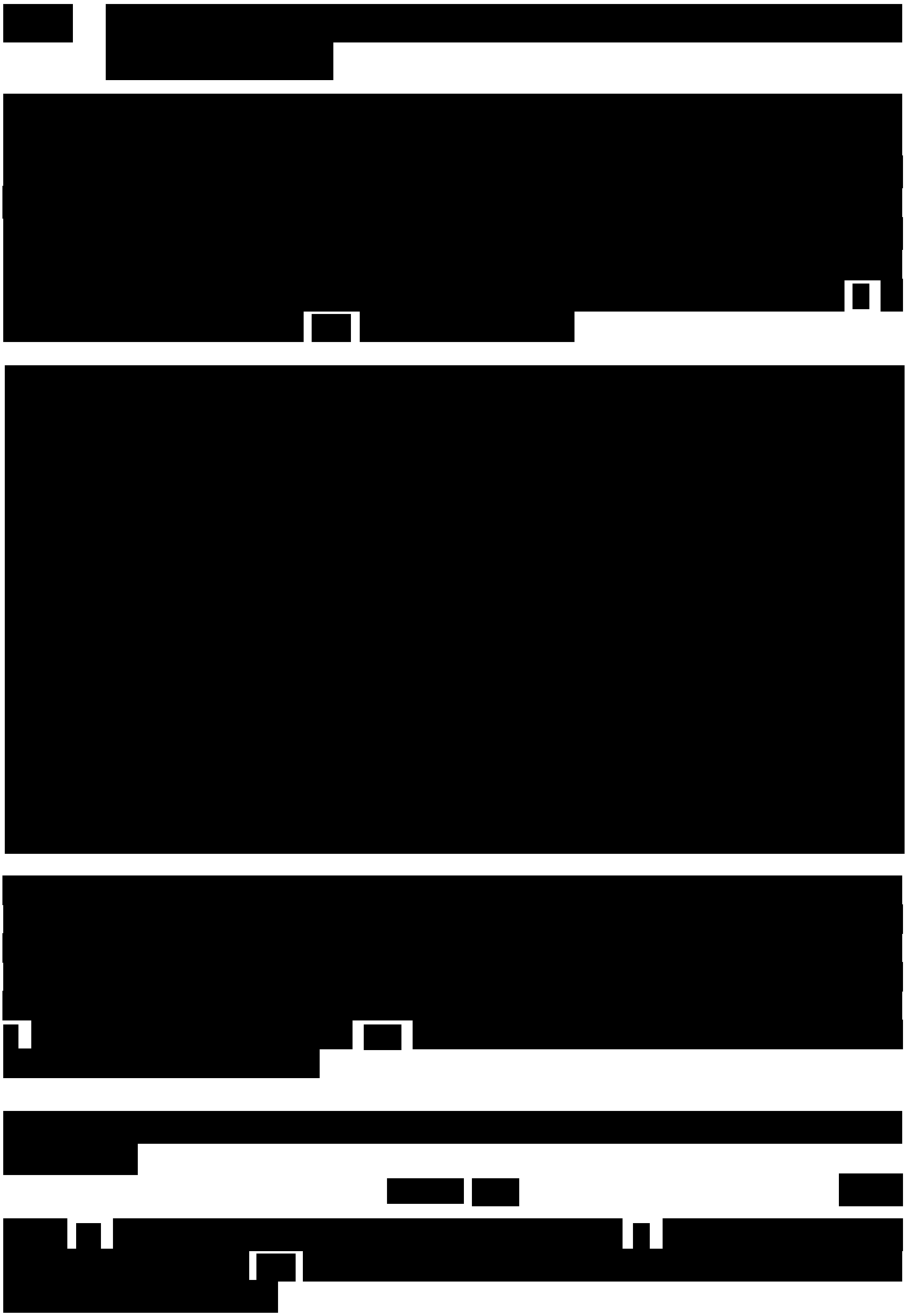

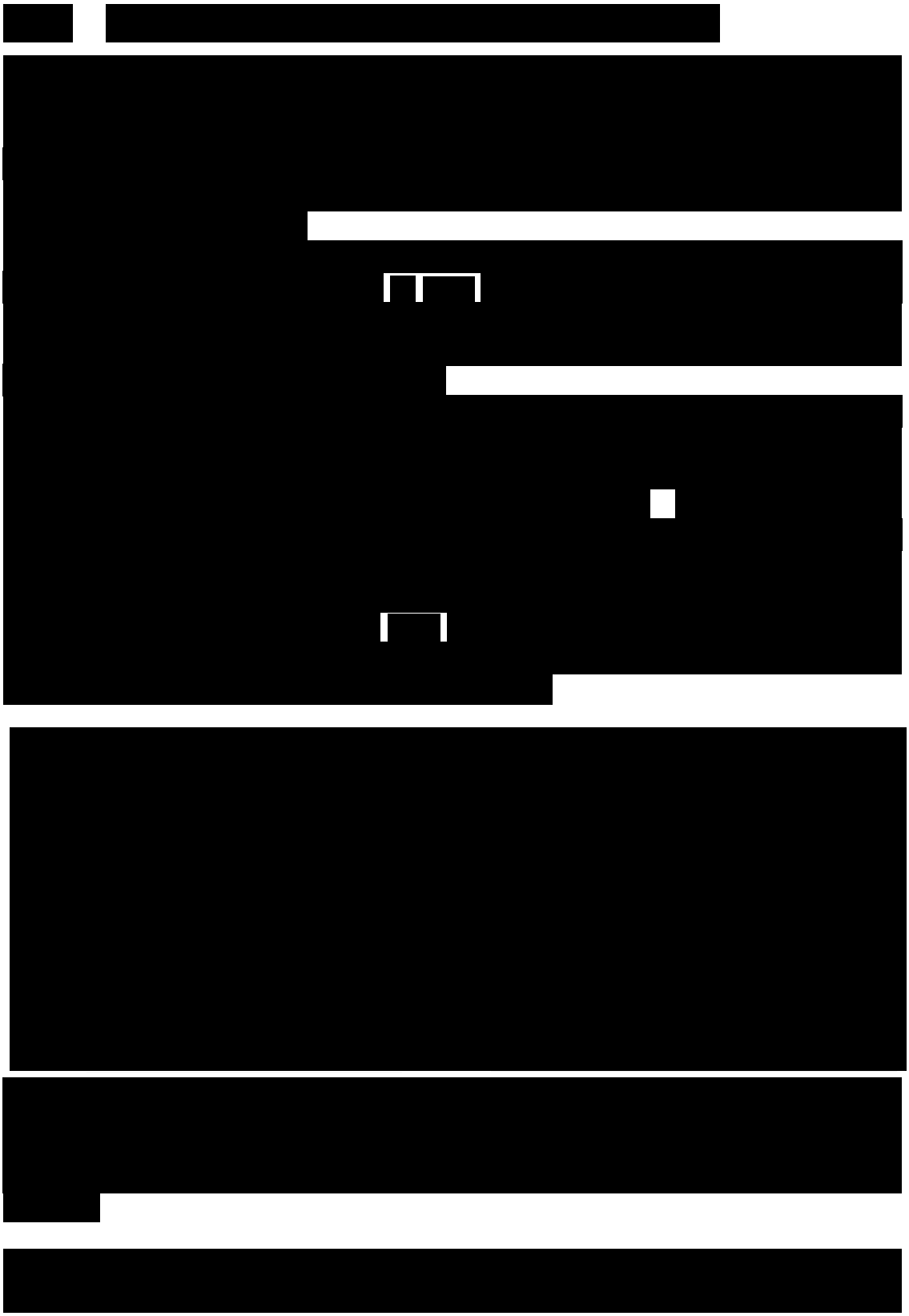

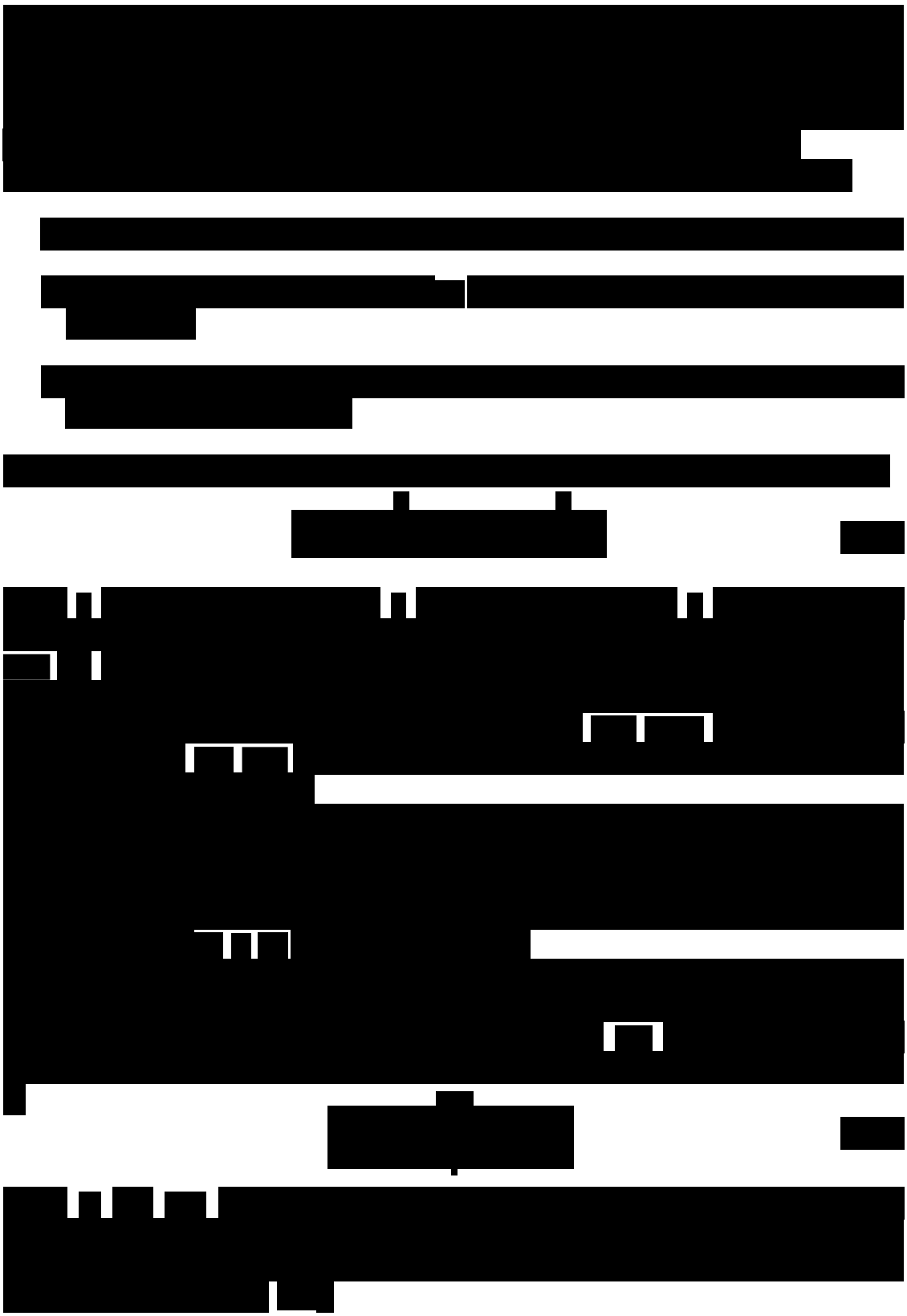

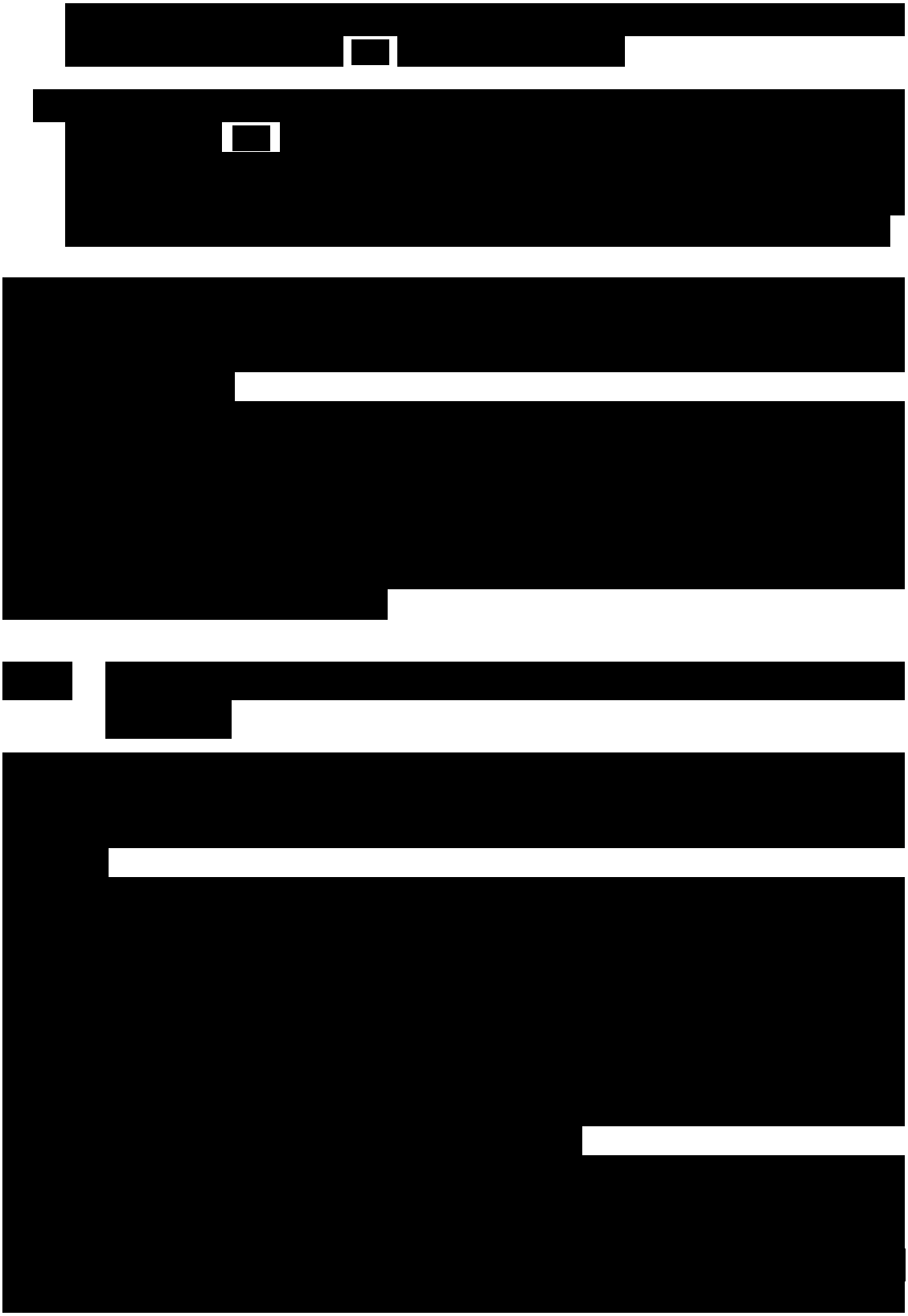

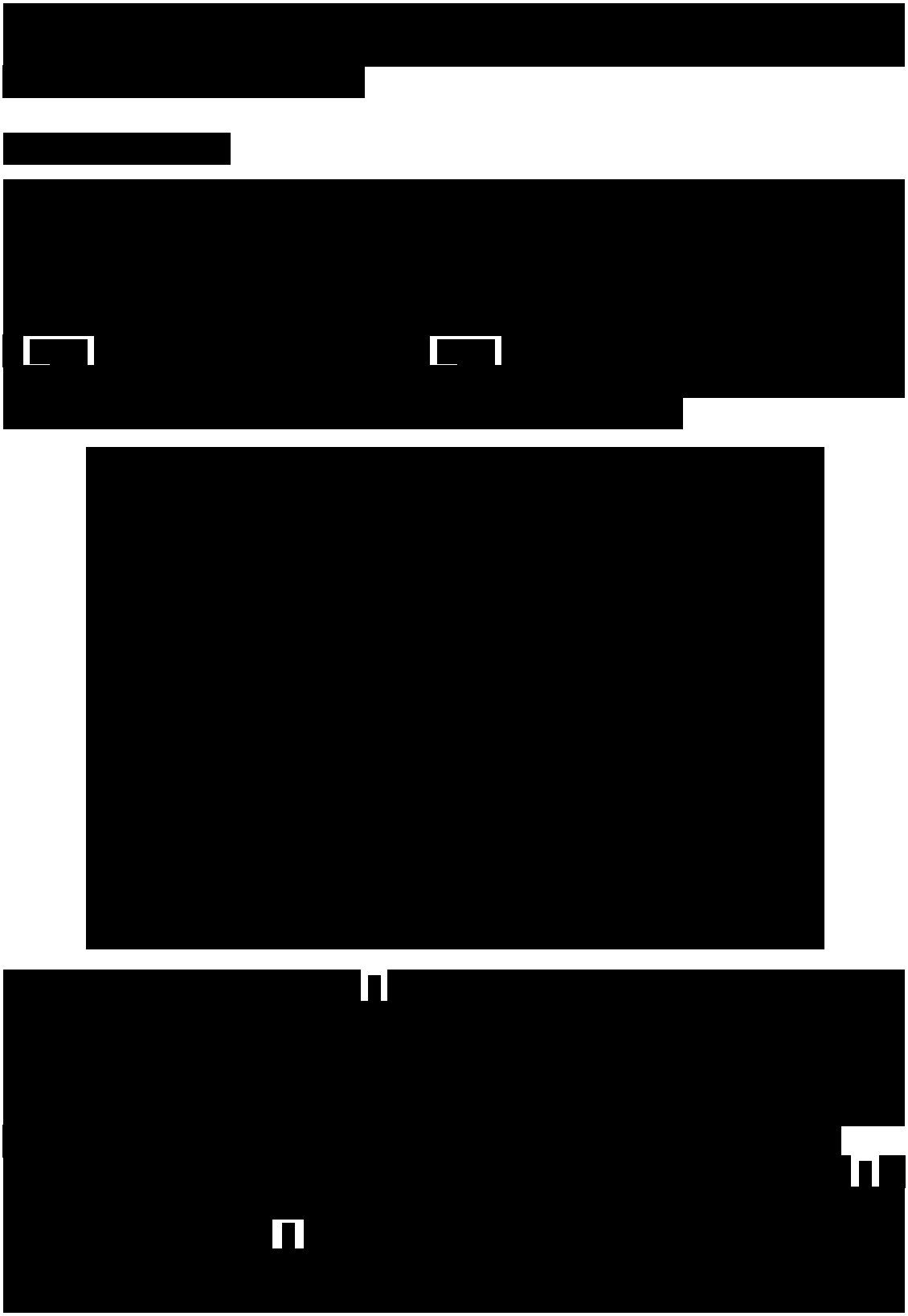

4.3 Computer vision tracking algorithm for dynamic characterisation

To enable quantitative analysis of the dynamic behaviour of origami structures, a dedicated computer–vision algorithm was developed in MATLAB. The objective

of this tool is to extract time–resolved displacement and rotation data of selected points directly from video recordings of dynamic experiments. This approach enables fully non–intrusive motion tracking, eliminating the need for physical sensors or markers integrated into the prototype.

The algorithm operates in four main stages: (i) video import and region definition, (ii) interest–point detection, (iii) feature tracking, and (iv) data post–processing. The workflow begins with the acquisition of a video sequence, processed frame by frame using dedicated MATLAB system objects. In the first frame, the user defines a region of interest (ROI) around the feature to be tracked, either manually or by specifying coordinates. Within this ROI, distinctive image features—typically corners or regions with strong intensity gradients—are detected using the Minimum Eigenvalue method [159], which provides robust point tracking even under moderate changes in illumination or orientation.

Once the initial features are detected, a point–tracking object is initialised with their coordinates. The tracker employs an optical–flow–based method to compute the displacement of each feature between consecutive frames, enforcing bidirectional consistency through a maximum bidirectional error criterion. For each frame, the updated positions of all valid features are recorded, displayed in real time, and stored for subsequent analysis.

In the post–processing stage, the algorithm reconstructs the trajectories of all tracked points and computes their displacements with respect to a reference origin defined in the image plane. From these trajectories, instantaneous direction vectors between the reference and each feature point are calculated, enabling the derivation of the rotation angle $\theta(t)$ as a function of time. Missing or invalid detections are automatically interpolated or flagged to prevent artefacts. By averaging the angular evolution of multiple tracked points, the algorithm provides a representative estimate of the overall rotational response of the structure, together with additional parameters such as oscillation amplitude and damping ratio.

The algorithm outputs time–series plots of angular displacement and centroid motion, allowing direct visualisation of the dynamic behaviour throughout the experiment. The decay of oscillation peaks is fitted using logarithmic decrement techniques to estimate the equivalent damping coefficient of the structure. This enables first–order dynamic characterisation directly from video data, without the need for external instrumentation.

Although currently applied to proof–of–concept videos of simplified prototypes, the framework establishes a foundation for future dynamic validation of origami–inspired mechanisms. The objective of this tool is to extract detailed displacements, velocities and accelerations of specific tracking points under realistic operating conditions. This methodology thus represents a crucial complement to the reduced–order bar–and–hinge simulations, effectively bridging numerical predictions with experimentally observed dynamic behaviour.

4.3.1 Experimental validation on a simple fold

As validation of the computer–vision algorithm, a dynamic experiment conducted on a simple fold specimen is presented here to demonstrate its capability in reconstructing angular motion and estimating damping parameters. The test setup consisted of a single fold origami element suspended horizontally and held in the folded position by a thin thread. Upon cutting the thread, the structure was released and allowed to oscillate freely under gravity and its own elastic restoring moment, producing a characteristic damped rotational motion (Fig. 4.19). The test was recorded using a high–definition c
motion plane, ensuring that all relevant d
frame.

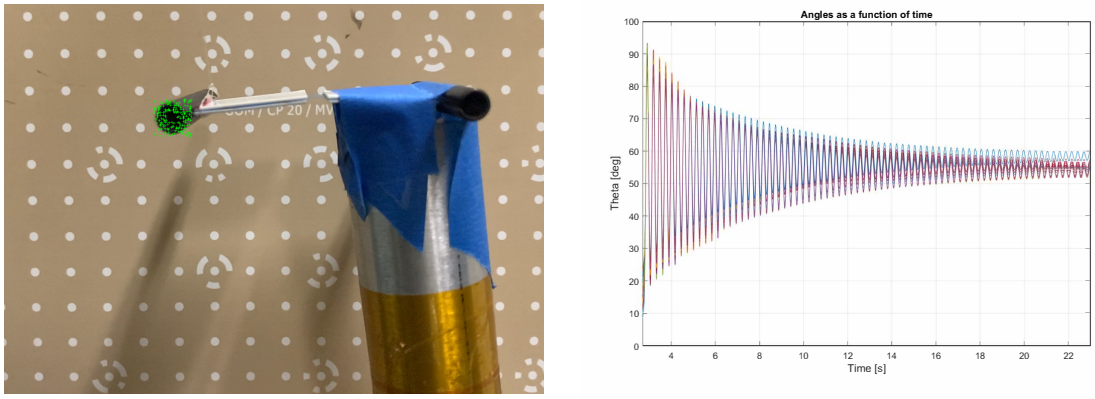

Figure 4.19: Dynamic measurement of damping coefficient on a simple origami fold: On the left - Setup for the dynamic validation of the computer–vision algorithm on a simple fold specimen. The green markers indicate the features automatically detected and tracked during the experiment. On the right - Angular displacement $\theta(t)$ showing the damped oscillatory motion.

After importing the video into MATLAB, the algorithm automatically detected a dense cluster of feature points near the fold tip (shown on the left in green in Fig. 4.19). The trajectory of each point was tracked frame–by–frame using the optical–flow–based point tracker, from which the direction vector $\mathbf{v}(t)$ connecting the origin (fixed base) to each tracked point was reconstructed. The instantaneous rotation angle $\theta(t)$ was computed as the angle between $\mathbf{v}(t)$ and the horizontal reference vector $\mathbf{x} = [-1, 0]$. The result is a time–resolved evolution of $\theta(t)$ for all tracked features, as shown on the right in Fig. 4.19, where the collective oscillation and its gradual decay are clearly visible.
From the time history of $\theta(t)$, the algorithm computed the centroid of all angular trajectories to obtain a representative global response of the system. Successive oscillation peaks were extracted from this averaged signal to evaluate the logarithmic

decrement, defined as

$$\delta = \ln\left(\frac{\theta_i}{\theta_{i+1}}\right),$$

which quantifies the exponential rate of decay of the oscillation amplitude. In this specific experiment, the computed value of $\delta = 0.0628$ corresponds to a damping ratio ζ obtained from the classical relationship

$$\delta = \frac{2\pi\zeta}{\sqrt{1-\zeta^2}},$$

yielding $\zeta \approx 0.01$. This result is consistent with the expected low damping of lightweight foldable laminates, confirming that the vision–based tracking algorithm can reliably capture the oscillatory motion and extract meaningful dynamic parameters directly from video data.

Although this test was conducted on a simplified specimen, it demonstrates the algorithm's effectiveness in retrieving angular displacement, oscillation frequency, and damping behaviour without any physical sensors. This approach will be extended in future experiments to the full origami prototypes tested on the MGSE, enabling complete dynamic characterisation through purely optical measurements.

4.3.2 Discussion and future implementations

The computer–vision tracking algorithm described in this section was developed as a preparatory tool to complement the experimental infrastructure introduced earlier in this chapter. It has already been used for other dynamic measurements in an industrial environment within Astradyne, but has not yet been applied directly to complex origami deployment experiments for validation against the bar–and–hinge results. Although no dynamic measurements have yet been performed for this specific purpose, the algorithm represents a key component of the broader validation framework designed for future testing campaigns.

At the current stage, the experimental activities related to this research have primarily focused on the characterisation of folding stiffness, which remains the dominant uncertainty in the bar–and–hinge formulation. Consequently, the dynamic testing phase, requiring synchronised video acquisition and actuation through the MGSE (Sec. 4.2.4), has been postponed until the completion and consolidation of the ongoing stiffness calibration campaign.

During deployment, the system will operate with a fixed camera positioned perpendicularly above the MGSE plane, providing a full–field view of the origami structure during actuation. Frame timestamps will be synchronised with actuator control signals through a shared trigger line managed by the microcontroller unit, ensuring temporal alignment between image acquisition and mechanical input. By combining optical data with actuation logs, the algorithm will enable the reconstruction

of time–resolved displacement, velocity, and acceleration fields for selected nodes of the structure.
Such experimental campaigns are planned as part of the future developments of this research, in which the computer–vision system will be employed in conjunction with the MGSE to provide quantitative validation of the dynamic bar–and–hinge framework.
In summary, the present work establishes the methodological foundation and software architecture necessary for subsequent experimental verification. While not yet applied to full–scale measurements, the algorithm constitutes an essential step toward a complete experimental–numerical pipeline for the dynamic characterisation of origami–inspired structures.

Chapter 5

Validation of the dynamic bar–and–hinge framework

The final chapter of this dissertation presents the numerical validation of the dynamic bar–and–hinge framework developed during the three-years study. After deriving the governing equations of motion, formulating the mass and damping matrices, and implementing the time-integration algorithms in Chapter 3, and after introducing the numerical framework at the end of Chapter 4, this chapter closes the methodological loop by demonstrating that the proposed formulation can reliably reproduce the nonlinear dynamics of canonical origami structures under both quasi-static and transient loading.

The chapter therefore serves two complementary purposes. First, it evaluates the performance of different time-integration schemes, explicit and implicit, within the dynamic bar–and–hinge solver, analysing their respective accuracy, stability, and computational cost. Second, it benchmarks the complete simulation framework against high-fidelity finite-element models, thereby providing a rigorous quantitative validation of the formulation introduced in the earlier chapters.

The validation workflow begins with a discussion of the trade-offs between explicit and implicit integration strategies, where Forward Euler, Newmark-β, and HHT-α are compared in terms of convergence behaviour, numerical damping, and overall runtime. Subsequently, a systematic sequence of verification cases is presented, ranging from the simplest single-fold mechanism to the full multi-cell Miura-ori pattern. Each case is examined under static and dynamic conditions, allowing the solver to be assessed across increasing levels of geometric complexity and mechanical coupling. For all benchmarks, the same constitutive parameters are retained, ensuring that the comparisons isolate the numerical performance of the framework itself.

The verification procedure is carried out through direct cross-comparison with detailed Ansys Mechanical simulations, which serve as the reference baseline.

Displacement histories, load–displacement curves, and phase responses are monitored at selected nodes, and the percentage deviations are reported to quantify the model's predictive accuracy. Across all cases, the bar–and–hinge framework demonstrates excellent agreement with the reference data while achieving speed-ups of up to two orders of magnitude relative to shell-element analysis.

The results presented in this chapter consolidate the key achievement of the work: the development of a dynamic, energy-consistent, and computationally efficient bar–and–hinge framework that faithfully captures the nonlinear behaviour of deployable origami systems. The concluding section discusses the implications of these results and outlines further improvements, such as experimental calibration of hinge stiffness and damping, as well as the integration of the solver into design optimisation and control workflows. Together, these validation studies confirm that the dynamic bar–and–hinge approach constitutes a reliable and scalable foundation for the future simulation of lightweight, foldable structures in both academic and industrial applications.

5.1 Explicit vs. Implicit Time Integration

In dynamic simulations of origami-inspired structures, the choice between explicit and implicit time-integration schemes hinges on a balance of stability, efficiency and robustness. Explicit algorithms such as Forward Euler advance the solution with a low per-step cost because they bypass the solution of global equilibrium equations; however, their stability is conditional on the time step being smaller than the critical limit dictated by the highest natural frequency, forcing very fine step sizes for stiff systems. Implicit schemes, represented here by Newmark-β and HHT-α solve a (generally nonlinear) equilibrium problem at every increment, incurring a higher computational expense per step, yet they are unconditionally stable in the linear regime and, with appropriate parameter choices, remain robust for large-deformation nonlinearities typical of deployable origami. Consequently, implicit methods can employ time steps an order of magnitude larger than their explicit counterparts, often yielding shorter overall runtimes for stiff or highly nonlinear problems while providing superior energy behaviour and numerical damping control [160, 161].

In the present work that advantage is realised through an *iterative Newton–Raphson solver executed at every implicit step.* Although each increment now entails the assembly of a consistent tangent matrix and a certain number (typically 2 to 3) equilibrium iterations, the quadratic convergence of Newton–Raphson means that the extra cost is quickly amortised when the step size can be increased by a factor of ten or more. Our full-Miura dynamic benchmark (Section 5.2.6) illustrates the trade-off clearly: Newmark-β and HHT-α require only 1000 steps at $\Delta t = 0.01s$ and finish in $\approx 100s$, whereas Forward Euler must take several more steps to achieve

comparable accuracy. Thus the iterative implicit formulation delivers the same or better total runtime while retaining unconditional stability, controllable numerical damping and a rigorous treatment of the nonlinear residual.

5.2 Validation results

The bar–hinge formulation was implemented from scratch in a stand-alone MATLAB code equipped with independent static and dynamic solvers. Verification relies on a single, but rigorous, methodology: for every benchmark a companion high-fidelity model is built in Ansys Mechanical, using the same material data, boundary conditions and time-integration parameters; specific FEM-model details are reported in the corresponding case-study subsections. Nodal displacements obtained with the MATLAB framework are compared directly against the FEM results; a benchmark is deemed *validated* when the monitored quantities (load vs displacements curves) show good agreement with respect to the FEM simulation.

The individual case studies were selected to reproduce canonical tests previously published in the literature, thereby allowing indirect comparison with those works while maintaining a single verification pipeline based on FEM cross-checks. Specifically:

- The three single-panel *static* tests reported by Filipov *et al.* [62], traction, shear and bending, are recreated and documented in Appendix 6.1.
- The *dynamic* benchmarks follow the configuration of previous literature, like [162], but are validated exclusively against our own FEM models to keep the error assessment self-consistent.

The three case studies considered are:

1. Simple origami fold – static & dynamic;
2. Miura-ori unit cell – static & dynamic;
3. Full miura-ori – static & dynamic;

All benchmarks use the same material properties present in Table 5.1.

Hinge stiffness is linear in the range between θ_1 and θ_2, outside of the range it is defined in a nonlinear form, as in [93], bars carry only axial load; out-of-plane bending and folding resistance is concentrated in the respective rotational springs, defined as in [62]. These values remain unchanged for all validation cases.

Table 5.1: Constitutive and geometric parameters adopted throughout the static and dynamic validations (unless explicitly stated otherwise).

	Symbol	Value
Young's modulus	E	10^6 Pa
Poisson's ratio	ν	0.25
Thickness (flat facets)	t	0.01 m
Density*	ρ	1 kg m^{-3}
Bar length	l_{bar}	1 m
Bar area	A_{bar}	same as [62]
Hinge (fold) width	b_{h}	1 m
Hinge rotational stiffness†	k_θ	0.0639 N m rad^{-1}

*Parameter varied ±5% in dynamic simulations for results fitting.

†Same arbitrary folding stiffness value used in [162].

5.2.1 Simple fold — static verification

The simple–fold configuration serves as the first benchmark for verifying the accuracy of the dynamic bar–and–hinge framework in its quasi-static limit.

The model consists of two identical square panels, 1×1 m^2 each, joined along a single crease that forms a 60° dihedral angle in the undeformed state (Fig. **??**). Each panel follows the N5B8 scheme, and the crease is represented by one torsional spring hinge, for a total of 16 bars and 9 hinges (one fold hinge and eight panel-bending hinges).

Nodes 1 and 3, outer corners of the left and right panels, are fully clamped ($u_x = u_y = u_z = 0$). Nodes 5 and 6, crease-side corners, are restricted in the $x-y$ plane ($u_z = 0$), thereby mimicking a pinned edge while allowing out-of-plane folding.

Static point loads of 0.5 N are applied in the $+x$ direction at Nodes 5 and 6, placing the fold in tension (Fig. 5.1). All material constants coincide with Table 5.1.

A Newton–Raphson algorithm with a residual tolerance of 10^{-6} N is employed. The total load is ramped in 1000 equal increments, and quadratic convergence is achieved within three to six iterations per step. For all three benchmarks a common high-fidelity reference solution was generated with a shell formulation. Each facet is meshed with `SHELL281` elements of nominal side length 0.10 m, resulting in a 10×10 grid per 1×1 m^2 panel. The fold lines are represented by either a revolute joint or an `MPC184` multi-point constraint, whose rotational stiffness matches the hinge parameter in the bar–and–hinge model. This mesh resolution is used in Case Studies 1–3 (simple fold, Miura-cell and full Miura pattern), whereas the finer comparisons reported in Appendix 6.1 adopt a 0.05 m element size (20×20 elements per panel).

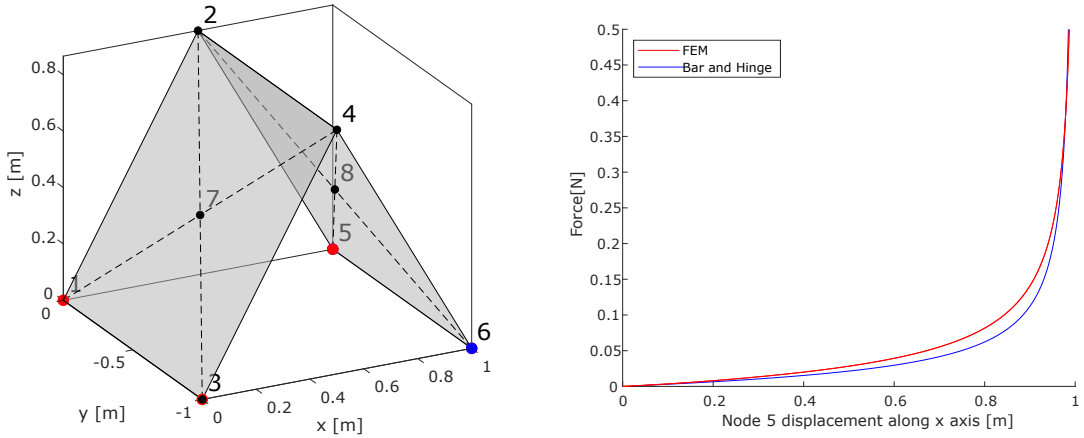

Figure 5.1: (Left) Comparison of displacement–load response and configuration for the simple fold. (Right) Displacement–load response at Node 5: bar–and–hinge (blue) versus FEM (red).

Figure 5.1 compares the bar–and–hinge solution (blue) with the reference finite-element data (red) for the displacements of Node 5 along the loaded x direction. The peak error value along the entire displacement-load curve is 8.76%, which is reasonable for the given nonlinear behaviour.

It can be noticed how, for small displacements, the bar and hinge performs virtually identically to the FEM reference model. in the nonlinear range, there is a slight increase in the error, which quickly returns to smaller values as the force increases, there may be several reasons for this, the authors deem the different mathematical model for the folding hinge in FEM and bar-and-hinge framework, the primary responsible for this type of behaviour.

5.2.2 Simple fold — dynamic verification

The simple–fold geometry of Section 5.2.1 is now excited dynamically with three Gaussian impulses of increasing peak force (0.0025 N, 0.01 N and 0.025 N). Each impulse has a centre frequency of 1 Hz and is applied in the $+x$-direction at Nodes 5 and 6. Four solution curves are reported for every load case: (i) FEM reference, (ii) Forward Euler with the "baseline" time step Δt, (iii) Forward Euler with a *smaller* Δt to illustrate the cost of enforcing stability, and (iv–v) the implicit Newmark-β and HHT-α schemes.

- **0.0025 N and 0.01 N cases.** Baseline $\Delta t = 0.02$ s for all integrators; the second Forward-Euler run uses $\Delta t = 0.008$ s.
- **0.025 N case.** Baseline $\Delta t = 0.008$ s; the refined Forward-Euler run drops to $\Delta t = 0.006$ s.

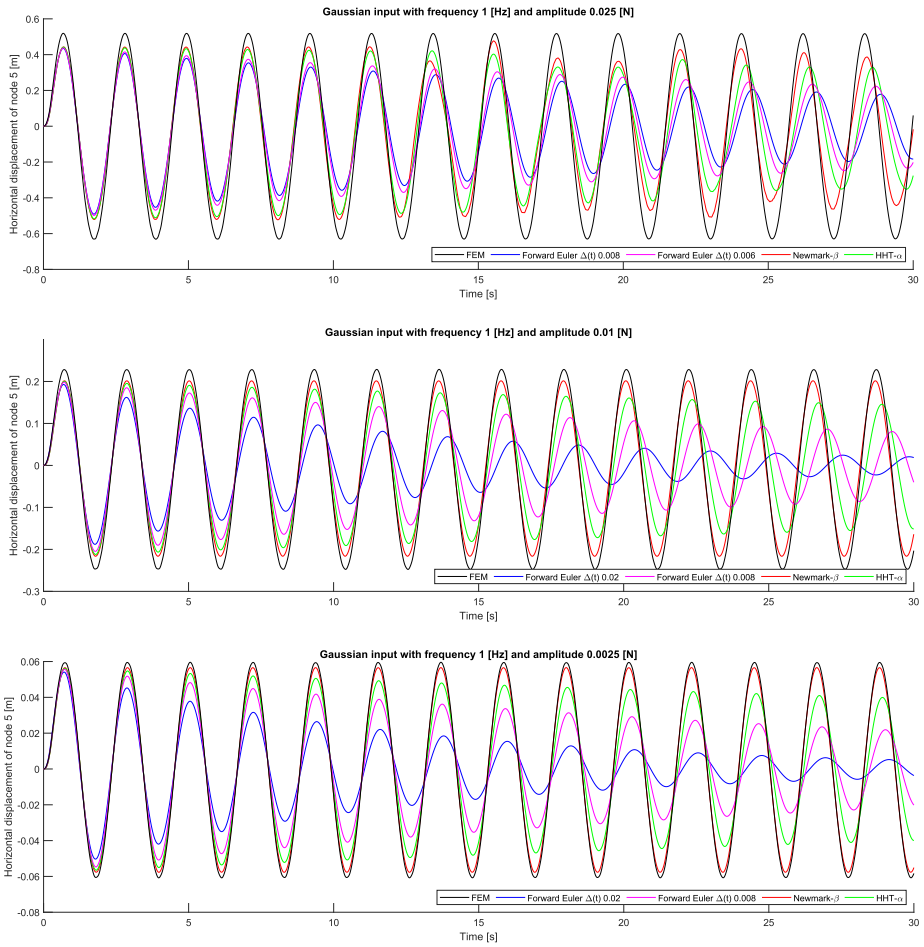

Figure 5.2: Horizontal displacement of Node 5 under Gaussian impulses of (a) 0.0025 N, (b) 0.01 N and (c) 0.025 N. Black: FEM; blue & magenta: Forward Euler with "large" and "small" Δt; red: Newmark-β; green: HHT-α.

Implicit parameters remain $\beta = 0.25,\ \gamma = 0.5$ for Newmark-β and $\alpha = -0.3$ ($\beta = 0.4225,\ \gamma = 0.8$) for HHT-$\alpha$.

Integrator	**Wall-clock time [s]**		
	0.0025 N	0.01 N	0.025 N
Forward Euler (Δt_1)	2.34	2.43	6.14
Forward Euler (Δt_2)	5.51	5.49	7.63
Newmark-β	2.29	2.83	9.51
HHT-α	5.41	6.35	17.03

Figure 5.2 confirms that all schemes capture the fundamental oscillation; differences arise in amplitude decay and phase error:

- **Forward Euler** with the larger Δt progressively drifts in amplitude and phase, especially for the 0.01 N and 0.0025 N impulses. Reducing Δt restores accuracy but increases runtime by $\sim 30\%$.
- **Newmark-β** tracks very well the FEM peak amplitudes for all impulses with no visible drift, maintaining the best accuracy–cost ratio overall.
- **HHT–α** introduces controlled high-frequency damping; the displacement envelopes sit slightly below those of Newmark, as predicted by the chosen spectral radius, while the fundamental period is reproduced with practically no phase error.

Aside from the $\pm 5\%$ density sweep listed in Table 5.1, no case-specific parameter fitting was performed; all stiffness values remain those obtained from the static calibration. The modest amplitude decay visible in every scheme stems from *algorithmic energy dissipation*: Forward Euler bleeds energy when its time step approaches the conditional-stability limit, Newmark-β is strictly energy-conserving only for *linear* systems, and HHT-α intentionally removes high-frequency energy through the chosen α. In practice, employing a smaller Δt for Forward Euler would greatly reduce the observed decay but at the cost of additional computational time. Further calibration, or time-step refinement, could narrow the residual amplitude gap with the FEM reference, yet the present comparison already shows that the implicit schemes, despite the added Newton–Raphson iterations, match or surpass Forward Euler in robustness and, for the higher load cases, even in overall runtime.

5.2.3 Miura-ori unit cell — static verification

The second reference targets the canonical *Miura-ori* unit cell [15], whose coupled folding mechanism is more demanding than the simple fold because in-plane stretching, out-of-plane bending and crease rotation interact simultaneously.

The unit cell comprises two rhomboidal facets joined by four mountain and valley folds, resulting in the node layout of Fig. 5.3. Each facet is modelled with the N5B8 discretisation, yielding 16 bars and 8 rotational hinges. The undeformed dihedral angle between the two facets is again 60°; the facet edge length is $L = 1.0$ m.

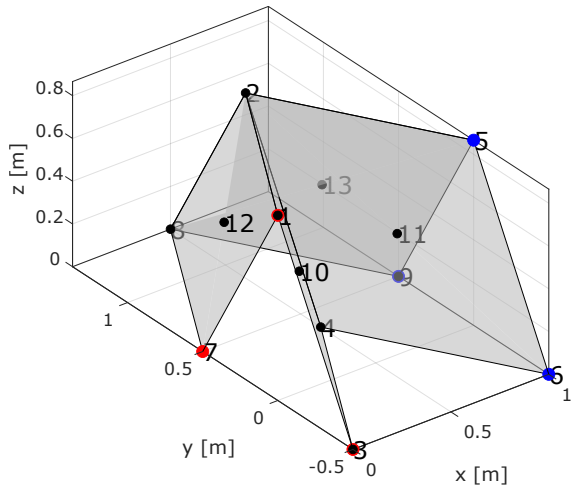

Figure 5.3: Bar–hinge discretisation, node numbering and boundary conditions for the Miura-ori unit cell.

The supports are chosen so that the single-degree-of-freedom Miura folding mechanism can develop without rigid-body motions:

- Node 3: fully clamped ($u_x = u_y = u_z = 0$);
- Node 1: fixed in x only;
- Node 7: fixed in x and z;
- Nodes 6 and 9: fixed in z.

A horizontal load of $P_x = 1.0$ N is applied at Nodes 5, 6 and 9 along the $+x$ axis, promoting the characteristic Miura unfolding.

Material data are identical to Table 5.1. The Newton–Raphson solver uses a residual tolerance of 10^{-6} N and 1000 load steps, achieving quadratic convergence within 4–7 iterations per step.

Figure 5.4 juxtaposes the bar–and–hinge prediction (round markers) with the nonlinear finite-element reference (squared markers) for the horizontal displacements of Nodes 5, 6 and 9 (respectively, red, blue and green). Agreement is excellent up to $u_x \approx 0.7$ m; beyond that, a slight stiffness underestimate appears, most noticeably at Node 6, where the bar–and–hinge curve lags the FEM response near the maximum load.

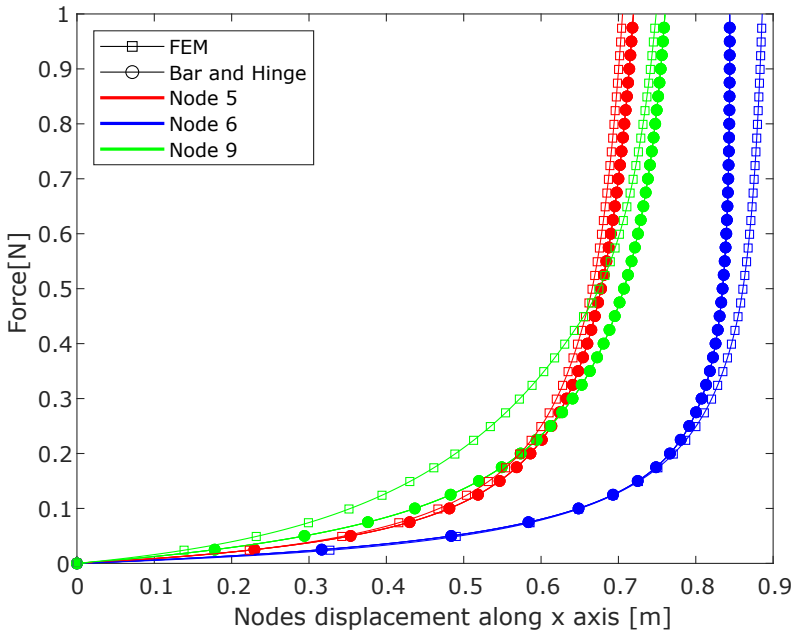

Figure 5.4: Force–displacement response of Nodes 5, 6 and 9: bar–and–hinge model (blue) vs. FEM reference (red).

The percentage displacement error is evaluated as

$$\text{Error}(\%) = \frac{u_{\text{BH}} - u_{\text{FEM, interp}}}{\max\left|u_{\text{FEM, interp}}\right|} \times 100,$$

where u_{BH} is the bar–and–hinge displacement at the final load step and $u_{\text{FEM, interp}}$ is the corresponding finite-element displacement interpolated at the same load level. Using this metric, the errors are 1.98 % for Node 5, 4.69 % for Node 6 and 11.75 % for Node 9. Therefore, the bar–and–hinge model reproduces the Miura kinematics with satisfactory accuracy.

Across the full loading path the bar–hinge predictions follow the FEM curves closely, yet the absolute error at Node 9 is slightly higher than at Nodes 5 and 6. Because Node 9 lies nearer the interior of the Miura crease pattern, its motion is influenced by a more complex combination of panel bending, in-plane shear and crease rotation. The present bar–and–hinge formulation idealises each facet with axial-only bars and torsional hinges, so its representation of coupled bending–shear effects is approximate; this may contribute to the under-prediction observed beyond $u_x \approx 0.7$ m. Other factors, such as local mesh density, hinge-stiffness calibration or numerical conditioning near the mechanism's locking limit, could also play a role.

5.2.4 Miura-ori unit cell — dynamic verification

The dynamic benchmark reuses the geometry and discretisation of the static Miura cell (Section 5.2.3) but now subjects the structure to a transient horizontal impulse so that the three time–integration algorithms can be compared against a shell–element reference solution.
To preserve the single-DOF Miura folding mechanism while eliminating rigid-body motion, the following supports are imposed (see Fig. 5.3 for node numbers):

- Node 3: $u_x = u_y = u_z = 0$;
- Node 1: $u_x = 0$;
- Node 7: $u_x = u_z = 0$;
- Nodes 6, 9: $u_z = 0$.

A smooth horizontal impulse of force $0.01N$ and $1Hz$ frequency acts along the global $+x$-direction at Nodes 5,6,9. All simulations employ a constant step size $\Delta t = 0.05$ s.

Forward Euler, follows the equations presented in Section 3.4.1. For *Newmark–β* the average-acceleration pair $\beta = 0.25,\ \gamma = 0.5$ is used. The *HHT–α* scheme adopts $\alpha = -0.2,\ \beta = ((1-\alpha)^2)/4 = 0.36,\ \gamma = (1-2\alpha)/2 = 0.6$, giving a high-frequency spectral radius $\rho_\infty = 0.5$.

Figure 5.5 plots the horizontal displacements of Nodes $5, 6$ and 9 over a 10 s interval. The finite-element reference (black) exhibits an undamped oscillation with a fundamental period of $\approx$ 2 s, which serves as the baseline for evaluating the numerical schemes.

All three bar–hinge solutions capture the qualitative response; however, systematic differences emerge:

- **Forward Euler** exhibits strong numerical damping: its amplitude decays within 4–5 cycles and the phase gradually lags the reference, illustrating the conditional stability and low accuracy of this first-order scheme at the chosen Δt.
- **Newmark–β** tracks the FEM envelope closely for every node, with a small phase lead after $t \approx 8$ s; the energy-conserving properties of the average-acceleration variant are evident.
- **HHT–α** yields peak amplitudes that are modestly lower than those of Newmark, in line with the prescribed spectral radius $\rho_\infty = 0.5$, while preserving the fundamental period. Although no high-frequency chatter is visible in this particular test, the built-in numerical damping provides a useful safety margin for load cases with richer frequency content.

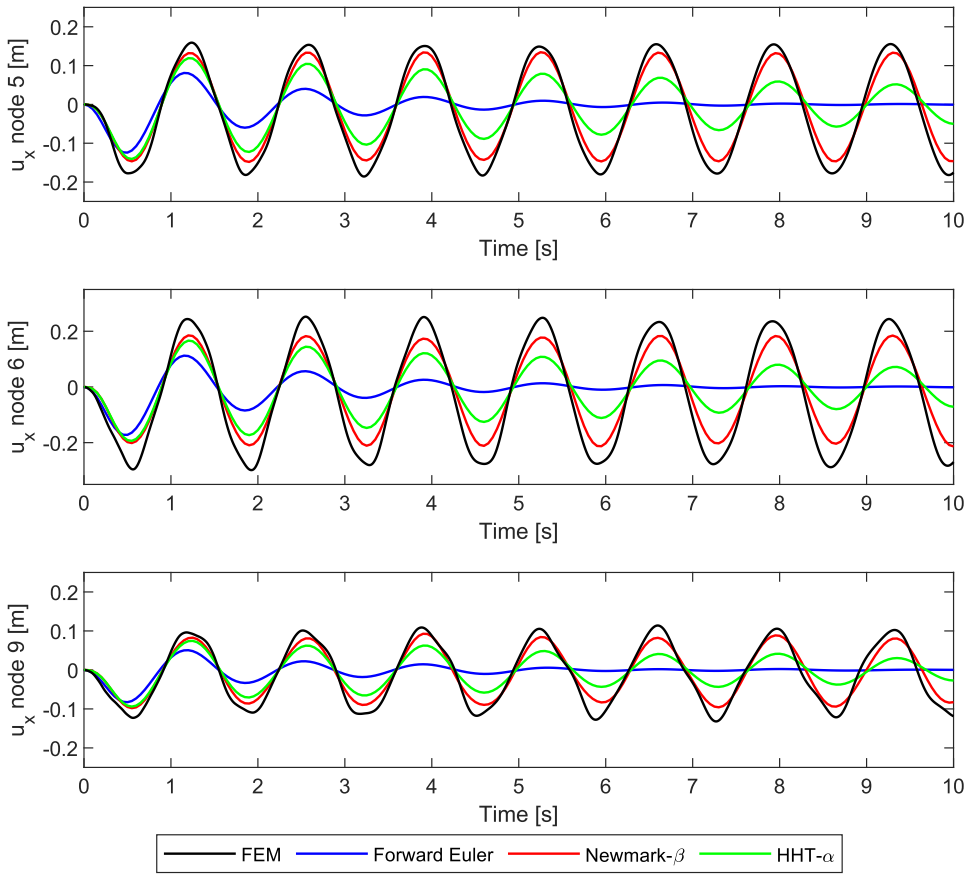

Figure 5.5: Time history of horizontal displacement at Nodes 5, 6 and 9: FEM (black), Forward Euler (blue), Newmark–β (red) and HHT–α (green); $\Delta t = 0.05$ s.

Qualitatively, the peak-to-peak amplitudes predicted by Newmark and HHT differ from the FEM values by an acceptable margin. The larger deviation at Node 6 mirrors the trend observed in the static benchmark and suggests that coupled bending–shear effects in the interior region remain the most challenging to model. Nonetheless, the overall agreement confirms that the proposed bar–and–hinge framework, combined with either Newmark–β or HHT–α, can reproduce the dominant dynamic characteristics of the Miura mechanism with acceptable accuracy.

5.2.5 Full Miura-ori structure — static verification

The third and most demanding benchmark is a 4×4 Miura-ori tessellation (Fig. 5.6), assembled by tiling the unit cell of Section 5.2.3. Each facet is modelled with the N5B8 discretisation, giving $8 \times 4 \times 16 = 512$ bars, 112 folding rotational hinges and 256 bending rotational hinges for the entire sheet.

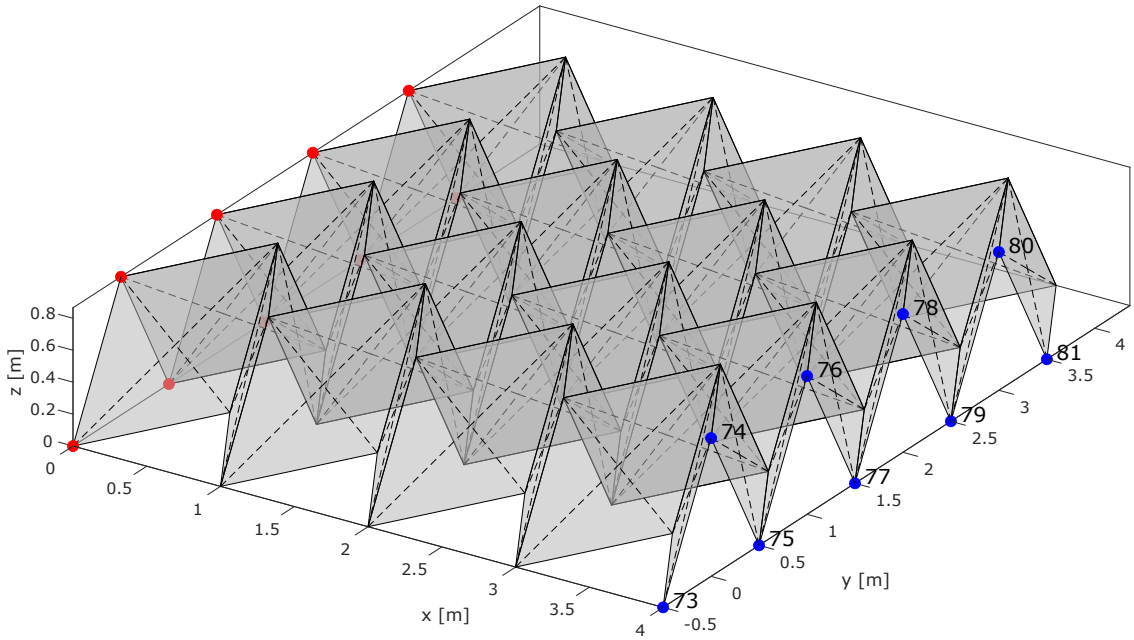

Figure 5.6: Bar–hinge discretisation of the 4×4 Miura sheet. Red nodes: fixed edge; blue nodes: loaded edge. Dashed lines denote crease lines, solid lines denote panel edges.

To reproduce the canonical "Miura mechanism" while preventing rigid- body motion, two opposite edges of the sheet are constrained as follows:

- **Fixed edge (red nodes).** Nodes with $z = 0$ are clamped in both x and z ($u_x = u_z = 0$); nodes with $z \neq 0$ are fixed in x only ($u_x = 0$). These supports mirror the kinematic assumptions commonly used in origami deployment studies.
- **Loaded edge (blue nodes).** The same rule is applied: if $z = 0$ the node remains fixed in z, otherwise it is free to move, ensuring that the fold-propagation mechanism is unobstructed.

A horizontal point load of 0.5 N is applied to each of the nine blue nodes on the free edge, producing a total horizontal forcing of 4.5 N in the global $+x$ direction. The load acts quasi-statically and drives the sheet toward its flattened configuration.

The Newton–Raphson algorithm with a residual tolerance of 10^{-6} N is employed; the total load is ramped in 1000 increments, achieving quadratic convergence within 5–8 iterations per step.

Figure 5.7 displays the force–displacement curves for all nine loaded nodes (73–81). The bar–and–hinge predictions (blue) overlay the nonlinear shell reference (red) almost everywhere. The close overlap confirms that the framework captures both the global deployment and the subtle variation in stiffness along the loaded edge.

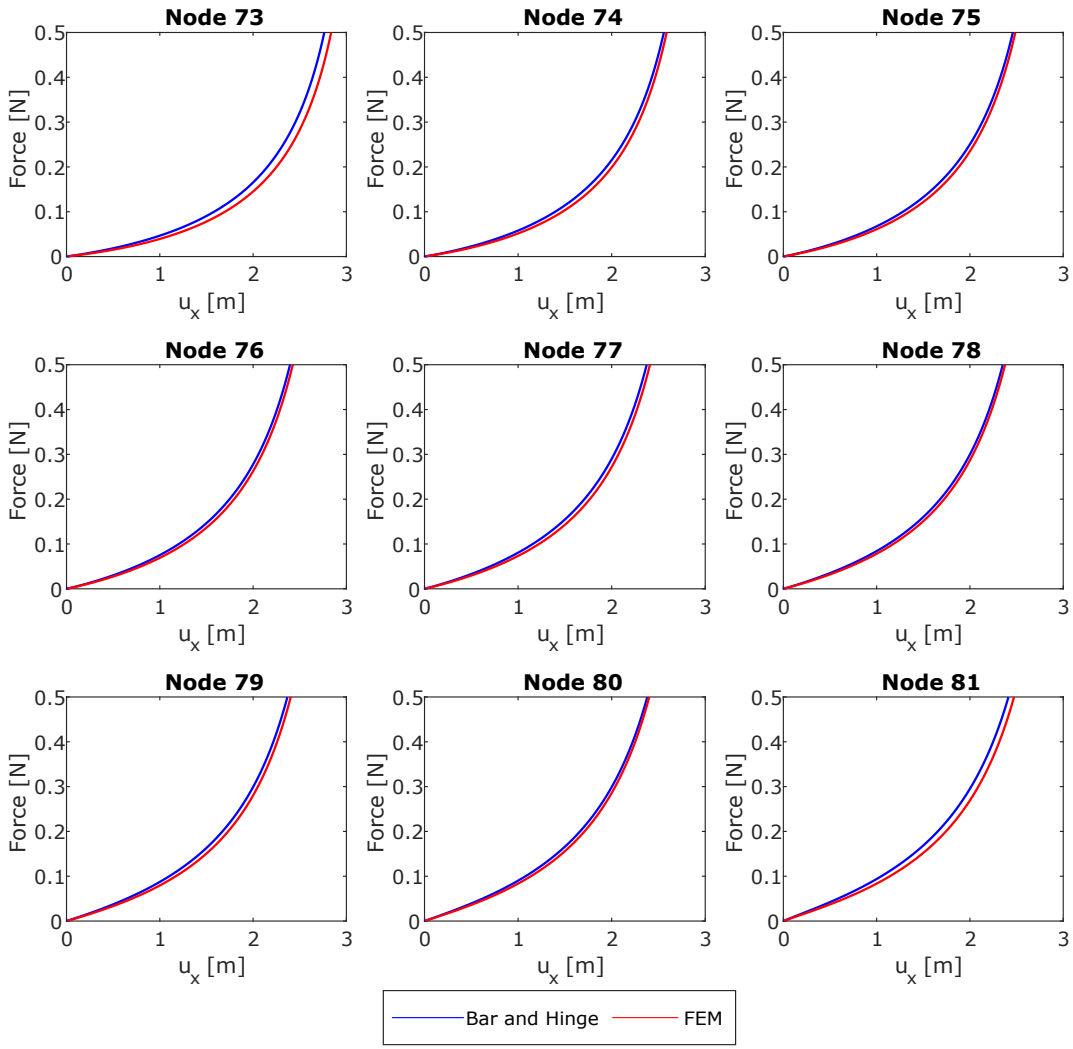

Figure 5.7: Total horizontal load versus displacement of the loaded corner node: bar–and–hinge model (blue) and FEM reference (red).

All curves exhibit the expected exponential stiffening as the pattern approaches the flattened configuration. The bar–and–hinge model is slightly stiffer than the shell reference for Nodes 73 and 76 and slightly softer for Nodes 79–81, but the discrepancies are limited. The node-to-node variation most likely reflects local differences in panel bending–shear coupling rather than a systematic bias, suggesting that the hinge-stiffness calibration used for the unit cell generalises well to the full sheet. Given the modest errors and the significant reduction in CPU time relative to the shell model, the case study is closed and the study moves to the dynamic case.

5.2.6 Full Miura-ori structure — dynamic response

The 4×4 Miura sheet of Section 5.2.5 is now subjected to a transient horizontal impulse so the three time–integration schemes can be benchmarked on a large, strongly coupled deployable system.

Supports replicate the static set-up to preserve the Miura mechanism: red-edge nodes are fixed ($u_x = u_z = 0$ when $z = 0$, otherwise $u_x = 0$); blue-edge nodes obey the same rule but remain free in the directions required for folding (see Fig. 5.6).

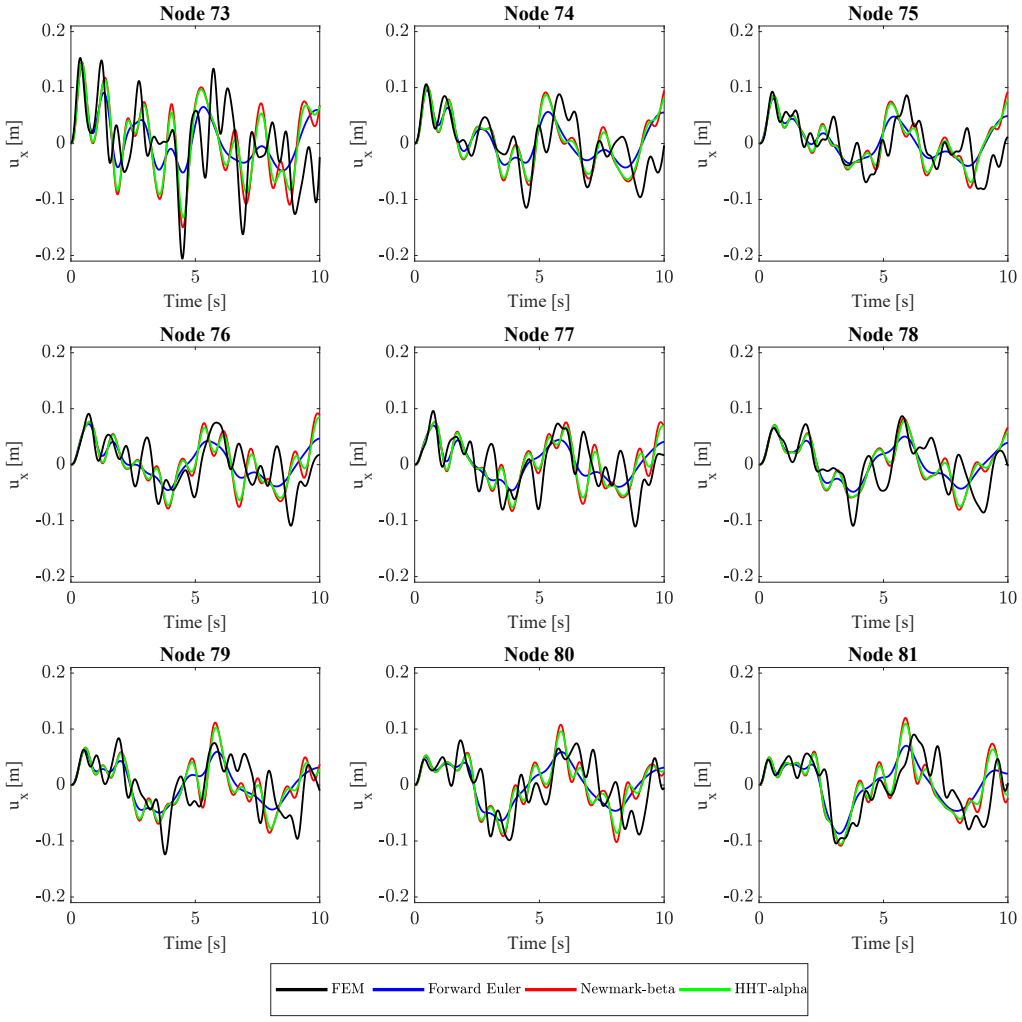

Figure 5.8: Time histories of horizontal displacement at the nine loaded nodes: FEM (black), Forward Euler (blue), Newmark–β (red) and HHT–α (green); $\Delta t = 0.01$ s.

A smooth Gaussian impulse with amplitude 0.01 N and 1 Hz is applied at all nine

blue nodes. All calculations use a uniform step size $\Delta t = 0.01$ s.

Forward Euler follows the equations presented in Section 3.4.1. *Newmark–β* employs the average-acceleration setting $\beta = 0.25,\ \gamma = 0.5$. *HHT–$\alpha$* adopts $\alpha = -0.1,\ \beta = ((1-\alpha)^2)/4 = 0.3025,\ \gamma = (1-2\alpha)/2 = 0.6$, yielding a high-frequency spectral radius $\rho_\infty \approx 0.67$.

Figure 5.8 presents the horizontal-displacement time histories of the nine loaded edge nodes (73–81) in the full Miura sheet. Each panel covers a 10 seconds interval and overlays the finite-element reference (black) with the bar-and-hinge predictions obtained using Forward Euler (blue), Newmark-β (red) and HHT-α (green). Across all nodes, the bar-and-hinge traces follow the FEM waveform closely: overall amplitude trends are well matched and only mild phase shifts appear toward the end of the record. The overall similarity confirms that the dynamic framework captures the multi-cell response with good fidelity.
All bar–and–hinge traces reproduce the dominant oscillatory behaviour:

- **Forward Euler** shows the strongest numerical damping, with amplitudes falling by $\sim 30\%$ by $t = 10$ s and a slight phase lag; nevertheless it captures the envelope of the fundamental mode.
- **Newmark–β** follows the FEM peaks closely for each node, with small amplitude error and minimal phase drift, confirming the energy-conserving character observed in the smaller benchmarks.
- **HHT–α** lies between the two: it damps the highest frequencies more than Newmark, suppressing the residual chatter present in the FEM trace, yet retains the correct global period. Amplitude errors remain limited.

These discrepancies are comparable to those seen in the static test and confirm that the bar–and–hinge model, combined with either Newmark–β or HHT–α, can faithfully simulate the transient deployment of large Miura assemblies while offering a substantial reduction in computational cost relative to shell-element analysis.

A key motivation for developing the bar–and–hinge framework is the sharp reduction in analysis time relative to high-fidelity finite-element models. Table 5.2 compares wall-clock times for the full 4×4 Miura sheet under the dynamic impulse considered in Section 5.2.6. All runs were carried out on the same workstation (Intel® i9-13900K, 32 GB RAM); the shell model used four parallel CPU cores, whereas the bar–and–hinge code executed in a single MATLAB thread.

5.2.7 Effectiveness of the proposed framework

Across six benchmarks (three static, three dynamic) the bar–and–hinge model matched finite-element reference solutions within the verification thresholds set in Section 5.2:

Table 5.2: Wall-clock time for the dynamic full-sheet simulation ($\Delta t = 0.01$ s, 1000 steps).

Integrator / Solver	**Time [s]**	**Speed-up vs. FEM**
Forward Euler	99	$\times 78$
Newmark–β	98	$\times 81$
HHT–α	189	$\times 42$
Nonlinear shell FEM*	7 620	—

* Ansys `SHELL281` mesh, 4 CPU cores.

- **Accuracy**: peak displacement errors never diverged from the FEM reference for all monitored nodes, even in the multi-modal full-sheet dynamics.
- **Integrator behaviour**: Newmark-β delivered the closest agreement overall, while HHT-α offered controlled high-frequency damping that suppressed numerical chatter at a modest amplitude cost. Forward Euler remained useful for preliminary sweeps thanks to its negligible per-step cost, provided a sufficiently small Δt was chosen.
- **Computational efficiency**: wall-clock times for the dynamic full-sheet problem were 99 s (Euler), 98 s (Newmark), and 189 s (HHT), versus 2 hrs for an Ansys `SHELL281` model on four CPU cores (Table 5.2). The resulting 40-80$\times$ speed-up enables design-space exploration and controller tuning loops that would be prohibitive with traditional FEM software.

Chapter 6

Conclusions and future developments

Origami–inspired deployable structures occupy a growing niche in applications where large surface areas or functional volumes must be compactly stowed and rapidly deployed. Their operational envelope is inherently *dynamic*: antenna reflectors unfold in seconds, foldable solar arrays vibrate under launch loads, and robotic surfaces undergo repeated shape reconfigurations. In this context, high–fidelity yet computationally efficient simulation tools are indispensable for design, control, and performance verification.
The present dissertation has contributed to this field by developing, implementing, and numerically validating a reduced–order dynamic framework based on a fully nonlinear bar–and–hinge formulation. The research originated from a concrete industrial requirement identified by *Astradyne*, which wanted to develop a predictive tool to simulate the mechanical behaviour of lightweight, textile–reinforced photovoltaic systems for space applications. From this practical motivation, the study evolved into a comprehensive investigation combining theoretical modelling, numerical implementation, and experimental validation.

Summary of contributions

The dissertation followed a logical progression from motivation to application. The **Preface** outlined the industrial and technological context linking Astradyne's textile–based solar array development to the need for efficient deployable–structure modelling. It presented the FRET (Flexible Reinforced Electronics with Textile) technology as the origin of the research problem and the rationale for developing a low–cost, high–accuracy simulation framework.
Chapter 1 reviewed the state of the art in the numerical modelling of origami–inspired systems, ranging from continuum mechanics and discrete–shell formulations to multibody and reduced–order approaches. Among these, the bar–and–hinge method was identified as an optimal compromise between computational efficiency and

physical fidelity. The review also revealed a key gap: the absence of robust dynamic formulations and publicly available implementations suitable for realistic engineering applications.

Chapter 2 developed the quasi–static formulation of the bar–and–hinge model. Starting from the principle of virtual work, the chapter derived the strain energy expressions of bars and hinges, established their consistent tangent stiffness matrices, and discussed the assembly and solution of nonlinear equilibrium equations. Special attention was devoted to the analytical calibration of fold and facet stiffnesses, ensuring mechanical consistency with finite–element benchmarks. These results established the static foundation on which the dynamic extension was built.

Chapter 3 extended the bar–and–hinge method to dynamic simulations, representing the core scientific contribution of this work. The equations of motion were derived by incorporating inertia and damping effects into the static formulation, and several time–integration schemes, Forward Euler, Newmark–β, and Hilber–Hughes–Taylor (HHT–α), were implemented and compared. A comprehensive study of numerical damping and energy conservation demonstrated that the framework can reproduce transient deployment and oscillatory behaviour with stability and accuracy. The resulting MATLAB solver is modular, computationally efficient, and energy–consistent, enabling large parametric studies of dynamic folding mechanisms.

Chapter 4 combined experimental and numerical investigations to characterise the mechanical response of flexible hinges. It detailed the design and fabrication of test specimens, the setup for measuring folding stiffness, and the post–processing procedure for computing both secant and tangent stiffnesses. The experimental data were complemented by a numerical study performed in Abaqus, in which the fold length was parametrically varied between 1 mm and 8 mm. The comparison with the theoretical model by Filipov *et al.* confirmed the dependence of stiffness on geometry and validated the analytical assumptions adopted in the framework. The chapter also introduced the complete MATLAB implementation integrating the static and dynamic solvers with experimental calibration data.

Chapter 5 validated the dynamic bar–and–hinge framework against a series of benchmark problems of increasing complexity, including single folds, Miura–ori unit cells, and complete multi–cell assemblies. The results were compared with high–fidelity finite–element simulations, demonstrating excellent agreement in both static and transient regimes while achieving speed–ups of up to two orders of magnitude relative to shell–based models. This confirmed the robustness, scalability, and engineering relevance of the proposed approach.

General conclusions

The research demonstrates that the bar–and–hinge paradigm, when extended to dynamic analysis, offers a powerful and versatile tool for simulating complex deployable mechanisms. It effectively bridges the gap between detailed finite–element models and purely kinematic representations, combining computational efficiency with mechanical accuracy. By integrating static and dynamic formulations within a unified MATLAB framework, the method enables the simulation of realistic folding sequences under external loads, boundary constraints, and large rotations, capabilities that are essential for next–generation deployable space systems.

The dynamic solver developed in this work advances the state of the art in reduced–order modelling. Its formulation, modular design, and compatibility with experimental data pipelines establish a solid foundation for future research and industrial application. Equally important, the synergy between numerical and physical testing has demonstrated the feasibility of using such frameworks for rapid prototyping, parameter identification, and early–stage design evaluation.

Future developments

Several promising directions emerge from this work:

- **Experimental validation of the dynamic solver:** upcoming tests will employ high–speed imaging and computer–vision tracking to capture time–resolved motion of deployable prototypes, enabling quantitative comparison between measured and simulated trajectories for model calibration.
- **Adaptive time–integration:** incorporating step–size control based on local error estimation will improve accuracy and efficiency during deployment and oscillation phases.
- **Multiphysics extensions:** coupling the solver with thermo–elastic or electro–mechanical effects will allow simulation of photovoltaic or shape–memory–based origami structures.
- **Design optimization:** integrating parameter sweeps and sensitivity analysis modules will enable inverse design and performance tuning for deployable mechanisms.

Finally, the framework will be progressively integrated into Astradyne's industrial workflow to support the design of next–generation foldable photovoltaic systems for both space and terrestrial applications. By enabling rapid simulation of deployment dynamics, stability, and energy dissipation, the solver will assist in the development

of high–performance textile–reinforced solar arrays and adaptive structural components.

In summary, this dissertation consolidates a unified methodology that merges theory, computation, and experimentation to advance the modelling of origami–inspired deployable structures. It establishes a bridge between conceptual design, numerical simulation, and experimental realisation, paving the way for future research and industrial innovation in adaptive and lightweight engineering systems.

Bibliography

[1] A. Kalantari, N. Cramer, J. Lee, A. Cangialosi, K. Chin, M. Edmonds, C. Fuller, T. Lu, M. Tolley, J. Werfel, R. Wood, Y. Yang, J. Zhu, and J. W. Burdick. PUFFER: An origami-inspired expandable robot for space exploration. In *Proc. IEEE Int. Conf. on Robotics and Automation (ICRA)*, pages 6836–6843, 2017.

[2] A. Buscicchio, D. Vittori, V. Netti, A. Troise, N. Mangialardi, D. Guaragnella, and M. Cinefra. FRET (flexible reinforced electronics with textile): A novel technology enabler for deployable origami-inspired lightweight aerospace structures. In *Proc. AIAA SciTech Forum*, 2023.

[3] N. Turner, B. Goodwine, and M. Sen. A review of origami applications in mechanical engineering. *Proc. Inst. Mech. Eng., Part C: J. Mechanical Engineering Science*, 230(14):2345–2362, 2016.

[4] K. Ikeya et al. Significance of 3U CubeSat OrigamiSat-1 for space demonstration of multifunctional deployable membrane. *Acta Astronautica*, 173:363–377, 2020.

[5] H. W. Brandhorst and J. A. Rodiek. Space solar array reliability: A study and recommendations. *Acta Astronautica*, 63(11):1233–1238, 2008.

[6] A. Pedivellano et al. Prototyping and engineering model test campaign of the 100W 1U PowerCube deployable solar array. In *Proc. AIAA SciTech Forum*, 2023.

[7] A. Buscicchio, G. Alessandrino, A. Troise, T. Sironi, and A. Gloder. SolarCube: An origami-inspired lightweight deployable solar panel for nanosatellites. In *Proc. 2023 European Space Power Conf. (ESPC)*, 2023.

[8] J. Maekawa. *Top Origami*. Sanrio Co., Ltd., Tokyo, Japan, 1985.

[9] T. Kawasaki. On the relation between mountain-creases and valley-creases of a flat Origami. In *Proc. Conf. on Origami and Its Applications*, 1990.

[10] T. C. Hull. Solving cubics with creases: The work of beloch and lill. *Amer. Math. Monthly*, 118(4):307–315, 2011.

[11] J. Justin. Mathematics of origami. *British Origami*, 118:28–30, 1986.

[12] Z. Abel, J. Cantarella, E. D. Demaine, D. Eppstein, T. C. Hull, J. S. Ku, R. J. Lang, and T. Tachi. Rigid origami vertices: Conditions and forcing sets. *J. Comput. Geometry*, 7(1):171–184, 2016.

[13] Y. Chen, R. Peng, and Z. You. Origami of thick panels. *Science*, 349(6246):396–400, 2015.

[14] Y. Chen, H. Feng, J. Ma, R. Peng, and Z. You. Symmetric waterbomb origami. *Proc. Roy. Soc. A: Math., Phys. and Eng. Sci.*, 472(2190):20150846, 2016.

[15] M. Schenk and S. D. Guest. Geometry of miura-folded metamaterials. *Proc. Nat. Acad. Sci.*, 110(9):3276–3281, 2013.

[16] S. D. Guest and S. Pellegrino. The folding of triangulated cylinders, part i: Geometric considerations. *J. Appl. Mech.*, 61(4):773–777, 1994.

[17] K. Miura. Method of packaging and deployment of large membranes in space. *Inst. of Space and Astronautical Sci. Rep.*, 618:1–9, 1985.

[18] G. Wei and J. S. Dai. A spatial eight-bar linkage and its association with the deployable platonic mechanisms. *J. Mech. Robotics*, 6(2):021010, 2014.

[19] Y. Chen, J. Feng, and Q. Sun. Lower-order symmetric mechanism modes and bifurcation behavior of deployable bar structures with cyclic symmetry. *Int. J. Solids and Struct.*, 139–140:1–14, 2018.

[20] B. J. Edmondson, R. J. Lang, M. R. Morgan, S. P. Magleby, and L. L. Howell. Thick rigidly foldable structures realized by an offset panel technique. In *Proc. 6th Int. Meeting on Origami Science, Mathematics, and Education (Origami 6)*, pages 149–161, Providence, RI, 2015. American Mathematical Society.

[21] R. J. Lang, M. R. Morgan, S. P. Magleby, and L. L. Howell. Towards developing product applications of thick Origami using the offset panel technique. *Mech. Sci.*, 7(1):69–77, 2016.

[22] B. J. Edmondson, R. J. Lang, S. P. Magleby, and L. L. Howell. An offset panel technique for thick rigidly foldable Origami. In *Proc. ASME Int. Design Eng. Tech. Conf.*, page V06BT07A030, 2013.

[23] T. Tachi. Rigid-foldable thick Origami. In *Proc. 5th Int. Meeting on Origami Science, Mathematics, and Education (Origami 5)*, pages 253–264. CRC Press, 2011.

[24] S. A. Zirbel, R. J. Lang, M. W. Thomson, D. A. Sigel, P. E. Walkemeyer, B. P. Trease, S. P. Magleby, and L. L. Howell. Accommodating thickness in Origami-based deployable arrays. *J. Mech. Des.*, 135(11):111005, 2013.

[25] R. Peng, J. Ma, and Y. Chen. Thick-panel Origami structures forming seamless surfaces. *Nat. Commun.*, 16:1256, 2025.

[26] C. Zhao, K. Zhang, J. Gao, Y. Yang, and Y. Song. One-degree-of-freedom flat-foldable thick-panel Origami structures. *Commun. Eng.*, 4:27, 2025.

[27] H. Fang, S. Li, H. Ji, and K. W. Wang. Dynamics of a bistable miura-Origami structure. *Phys. Rev. E*, 95(5):052211, 2017.

[28] Y. Xia and K.-W. Wang. Dynamics analysis of the deployment of miura-Origami sheets. In *Proc. ASME Int. Design Eng. Tech. Conf.*, 2019.

[29] Y. Yoshimura. On the mechanism of buckling of a circular cylindrical shell under axial compression. *NACA Tech. Memo.*, 1390, 1955.

[30] J. E. Suh, T. S. Kim, and J. H. Han. New approach to folding a thin-walled Yoshimura-patterned cylinder for spacecraft applications. *J. Spacecraft Rockets*, 58(2):516–530, 2021.

[31] J. Cai, X. Deng, J. Feng, and Y. Zhou. Geometric design and mechanical behavior of a deployable cylinder with miura-Origami. *Smart Mater. Struct.*, 24(12):125031, 2015.

[32] V. Deshpande, Y. Phalak, Z. Zhou, I. Walker, and S. Li. Golden ratio Yoshimura for meta-stable and massively reconfigurable deployment. *Philos. Trans. Roy. Soc. A: Math., Phys. and Eng. Sci.*, 382(2283):20240009, 2024.

[33] Ting-Uei Lee. *Elastic Energy Behaviours of Curved-Crease Origami*. PhD thesis, The University of Queensland, School of Civil Engineering, 2019.

[34] Koryo Miura and Tomohiro Tachi. Synthesis of rigid-foldable cylindrical polyhedra. *Symmetry: Art and Science*, pages 1–4, January 2010.

[35] B. Kresling. Natural twist buckling in shells: From the hawkmoth's bellows to the deployable kresling-pattern and cylindrical miura-Ori. In *Proc. IASS Symp.*, 2008.

[36] J. Ma and Z. You. Energy absorption of thin-walled square tubes with a prefolded Origami pattern—part i: Geometry and numerical simulation. *J. Appl. Mech.*, 81(1):011003, 2014.

[37] X. Jiang, C. Li, X. Zhou, P. Hao, and B. Wang. Harnessing the multistability of Kresling Origami for reconfigurable articulation in soft robotic arms. *Soft Robot.*, 9(2):212–222, 2022.

[38] L. Lu, X. Dang, F. Feng, P. Lv, and H. Duan. Conical Kresling Origami and its applications to curvature and energy programming. *Proc. Roy. Soc. A: Math., Phys. and Eng. Sci.*, 478(2257):20210712, 2022.

[39] H. Sharma, A. Chaudhary, and S. H. Upadhyay. Experimental verification of the bistable behavior of conical Kresling Origami. *Thin-Walled Struct.*, 190:110980, 2023.

[40] H. Yasuda and J. Yang. Reentrant Origami-based metamaterials with negative poisson's ratio and bistability. *Phys. Rev. Lett.*, 114(18):185502, 2015.

[41] Y. Li and S. Pellegrino. A theory for the design of multi-stable morphing structures. *J. Mech. Phys. Solids*, 136:103772, 2020.

[42] F. Feng, X. Dang, R. D. James, and P. Plucinsky. The designs and deformations of rigidly and flat-foldable quadrilateral mesh Origami. *J. Mech. Phys. Solids*, 142:104018, 2020.

[43] R. D. Resch. The topological design of sculptural and architectural systems. In *Proc. Assoc. Comput. Machinery*, New York, NY, USA, 1973. Association for Computing Machinery.

[44] F. Yang, Y. Chen, R. Kang, J. Ma, and Z. You. Design of single degree-of-freedom triangular Resch patterns with thick-panel Origami. *Mech. Mach. Theory*, 169:104650, 2022.

[45] On the design of Origami structures with a continuum of equilibrium shapes. *Compos. Part B: Eng.*, 115:144–150, 2017. Composite Lattices and Multiscale Innovative Materials and Structures.

[46] Y. Yu, S. Zang, H. Shen, Z. He, S. Li, J. Liu, J. Ma, and Y. Chen. Programming curvatures by unfolding of the triangular Resch pattern. *Int. J. Mech. Sci.*, 238:107861, 2022.

[47] A. E. H. Love. *A Treatise on the Mathematical Theory of Elasticity.* Cambridge Univ. Press, Cambridge, U.K., 1892.

[48] G. R. Kirchhoff. On the equilibrium and motion of an elastic disc. *J. für die Reine und Angewandte Math.*, 40:51–88, 1850. In German.

[49] Y. Vetyukov. Finite element modeling of Kirchhoff-Love shells as smooth material surfaces. *Z. Angew. Math. Mech. (ZAMM)*, 94(1–2):150–163, 2014.

[50] E. Reissner. The effect of transverse shear deformation on the bending of elastic plates. *J. Appl. Mech.*, 12:A69–A77, 1945.

[51] R. D. Mindlin. Influence of rotatory inertia and shear on flexural motions of isotropic, elastic plates. *J. Appl. Mech.*, 18:31–38, 1951.

[52] X. Y. Cui, G. R. Liu, and G. Y. Li. Analysis of Mindlin-Reissner plates using cell-based smoothed radial point interpolation method. *Int. J. Appl. Mech.*, 2(4):653–684, 2010.

[53] D. N. Arnold and F. Brezzi. Locking-free finite element methods for shells. *Math. Comput.*, 66(217):1–14, 1997.

[54] J. N. Reddy. A simple higher-order theory for laminated composite plates. *J. Appl. Mech.*, 51(4):745–752, 1984.

[55] J. L. Mantari, I. A. Ramos, and A. M. Zenkour. A unified formulation for laminated composite and sandwich plates subject to thermal load using various plate theories. *Int. J. Appl. Mech.*, 8(8):1650087, 2016.

[56] K.-J. Bathe. *Finite Element Procedures.* Prentice Hall, Englewood Cliffs, NJ, USA, 1st edition, 1996.

[57] C.-L. Liao. *An Incremental Total Lagrangian Formulation for General Anisotropic Shell-Type Structures.* PhD thesis, Texas A&M University, College Station, TX, USA, 1987.

[58] K.-J. Bathe and S. Bolourchi. A geometric and material nonlinear plate and shell element. *Comput. Struct.*, 11(1–2):23–48, 1980.

[59] F. López Jiménez and E. Oñate. A total lagrangian formulation for the geometrically nonlinear analysis of structures using finite elements. part i: Two-dimensional problems—shell and plate structures. *Int. J. Numer. Methods Eng.*, 20(12):2253–2281, 1984.

[60] H.-M. Jeon, Y. Lee, P.-S. Lee, and K.-J. Bathe. The MITC3+ shell element in geometric nonlinear analysis. *Comput. Struct.*, 146:91–104, 2015.

[61] F. Lechenault, B. Thiria, and M. Adda-Bedia. Mechanical response of a creased sheet. *Phys. Rev. Lett.*, 112(24):244301, 2014.

[62] E. T. Filipov, K. Liu, T. Tachi, M. Schenk, and G. H. Paulino. Bar and hinge models for scalable analysis of Origami. *Int. J. Solids Struct.*, 124:26–45, 2017.

[63] K.-J. Bathe. Measuring the convergence behavior of shell analysis schemes. *Comput. Struct.*, 89(3):285–301, 2011.

[64] J. Kiendl, M.-C. Hsu, M. C. H. Wu, and A. Reali. Isogeometric Kirchhoff-Love shell formulations for general hyperelastic materials. *Comput. Methods Appl. Mech. Eng.*, 291:280–303, 2015.

[65] T. J. R. Hughes, J. A. Cottrell, and Y. Bazilevs. Isogeometric analysis: CAD, finite elements, NURBS, exact geometry and mesh refinement. *Comput. Methods Appl. Mech. Eng.*, 194(39–41):4135–4195, 2005.

[66] J. A. Cottrell, T. J. R. Hughes, and Y. Bazilevs. *Isogeometric Analysis: Toward Integration of CAD and FEA*. John Wiley & Sons, 2009.

[67] J. Kiendl, K.-U. Bletzinger, J. Linhard, and R. Wüchner. Isogeometric shell analysis with Kirchhoff-Love elements. *Comput. Methods Appl. Mech. Eng.*, 198(49–52):3902–3914, 2009.

[68] M. Zareh and X. Qian. Kirchhoff-Love shell formulation based on triangular isogeometric analysis. *Comput. Methods Appl. Mech. Eng.*, 347:853–873, 2019.

[69] Z. Zou, M. A. Scott, D. Miao, M. Bischoff, B. Oesterle, and W. Dornisch. An isogeometric Reissner-Mindlin shell element based on Bézier dual basis functions: Overcoming locking and improved coarse mesh accuracy. *Comput. Methods Appl. Mech. Eng.*, 370:113283, 2020.

[70] N. Azizi and W. Dornisch. A rotation-based geometrically nonlinear spectral Reissner–Mindlin shell element. *Finite Elem. Anal. Des.*, 251:104416, 2025.

[71] S. R. Woodruff and E. T. Filipov. A bar and hinge model formulation for structural analysis of curved-crease Origami. *Int. J. Solids Struct.*, 204–205:114–127, 2020.

[72] P. Dieleman, N. Vasmel, S. Waitukaitis, and M. van Hecke. Jigsaw puzzle design of pluripotent Origami. *Nat. Phys.*, 16:63–68, 2020.

[73] Y. Zhu and E. T. Filipov. An efficient numerical approach for simulating contact in Origami assemblages. *Proc. Roy. Soc. A*, 475:20190366, 2019.

[74] F. Feng, P. Plucinsky, and R. D. James. Helical miura-Origami. *Phys. Rev. E*, 101(3):033002, 2020.

[75] A. A. Shabana. Definition of the slopes and the finite element absolute nodal coordinate formulation. *Multibody Syst. Dyn.*, 1(3):339–348, 1997.

[76] J. Gerstmayr, H. Sugiyama, and A. Mikkola. Review on the absolute nodal coordinate formulation for large deformation analysis of multibody systems. *J. Comput. Nonlinear Dyn.*, 8(3):031016, 2013.

[77] K. Otsuka, K. Makihara, and H. Sugiyama. Recent advances in the absolute nodal coordinate formulation: Literature review from 2012 to 2020. *J. Comput. Nonlinear Dyn.*, 17(8):080803, 2022.

[78] I. Stanciulescu, T. Mitchell, Y. Chandra, T. Eason, and M. Spottswood. A lower bound on snap-through instability of curved beams under thermomechanical loads. *Int. J. Non-Linear Mech.*, 47(5):561–575, 2012.

[79] G. R. Liu. *Meshfree Methods: Moving Beyond the Finite Element Method.* CRC Press, Boca Raton, FL, USA, 2nd edition, 2009.

[80] E. Carrera. Theories and finite elements for multilayered plates and shells: A unified compact formulation with numerical assessment and benchmarking. *Arch. Comput. Methods Eng.*, 10(3):215–296, 2003.

[81] E. Carrera, M. Cinefra, M. Petrolo, and E. Zappino. *Finite Element Analysis of Structures Through Unified Formulation.* John Wiley & Sons, 2014.

[82] E. Carrera and V. V. Zozulya. Carrera unified formulation (CUF) for shells of revolution. i. higher-order theory. *Acta Mech.*, 234:109–136, 2023.

[83] E. Carrera and V. V. Zozulya. Carrera unified formulation (CUF) for the composite plates and shells of revolution: Layer-wise models. *Compos. Struct.*, 329:117936, 2024.

[84] J. N. Reddy and Jr. D. H. Robbins. Theories and computational models for composite laminates. *Appl. Mech. Rev.*, 47(6):147–169, 1994.

[85] K. M. Liew, Z. Z. Pan, and L. W. Zhang. An overview of layerwise theories for composite laminates and structures: Development, numerical implementation and application. *Compos. Struct.*, 216:240–259, 2019.

[86] E. Carrera, A. Pagani, R. Augello, and B. Wu. Popular benchmarks of nonlinear shell analysis solved by 1d and 2d CUF-based finite elements. *Mech. Adv. Mater. Struct.*, 27(13):1098–1109, 2020.

[87] E. Grinspun, A. N. Hirani, M. Desbrun, and P. Schröder. Discrete shells. In *Proc. ACM SIGGRAPH/Eurographics Symp. Comput. Animation*, pages 62–67, San Diego, CA, USA, 2003. Eurographics Assoc.

[88] A. I. Bobenko and Y. B. Suris. *Discrete Differential Geometry: Integrable Structure.* Amer. Math. Soc., 2008.

[89] M. Bergou, M. Wardetzky, S. Robinson, B. Audoly, and E. Grinspun. Discrete elastic rods. *ACM Trans. Graph.*, 27(3):63, 2008.

[90] R. Narain, A. Samii, and J. F. O'Brien. Adaptive anisotropic remeshing for cloth simulation. *ACM Trans. Graph.*, 31(6):147:1–147:10, 2012.

[91] T. Takei and H. Koiso. Application of discrete differential geometry to Origami simulation. *J. Geom. Graph.*, 17(2):145–158, 2013.

[92] K. Liu and G. H. Paulino. Highly efficient nonlinear structural analysis of Origami assemblages using the MERLIN2 software. In *Origami 7: Proc. 7th Int. Meeting Origami Science, Mathematics, and Education*, pages 1167–1182, 2018.

[93] K. Liu and G. H. Paulino. Nonlinear mechanics of non-rigid Origami: An efficient computational approach. *Proc. Roy. Soc. A*, 473(2206):20170348, 2017.

[94] E. D. Demaine, M. L. Demaine, D. Koschitz, and T. Tachi. Curved-Crease folding: A review on art, design and mathematics. In *Proc. IABSE-IASS Symp.*, 2011.

[95] J. P. Duncan and J. L. Duncan. Folded developables. *Proc. Roy. Soc. A*, 383(1784):191–205, 1982.

[96] E. T. Filipov, T. Tachi, and G. H. Paulino. Origami tubes assembled into stiff, yet reconfigurable structures and metamaterials. *Proc. Natl. Acad. Sci.*, 112(40):12321–12326, 2015.

[97] S. D. Guest and J. W. Hutchinson. On the determinacy of repetitive structures. *J. Mech. Phys. Solids*, 51(3):383–391, 2003.

[98] Z. Y. Wei, Z. V. Guo, L. Dudte, H. Y. Liang, and L. Mahadevan. Geometric mechanics of periodic pleated Origami. *Phys. Rev. Lett.*, 110(21):215501, 2013.

[99] M. R. Barnes. Form finding and analysis of tension structures by dynamic relaxation. *Int. J. Space Struct.*, 14(2):89–104, 1999.

[100] S. Adriaenssens, P. Block, D. Veenendaal, and C. Williams. *Shell Structures for Architecture: Form Finding and Optimization*. Routledge, 2014.

[101] X. Provot. Deformation constraints in a mass-spring model to describe rigid cloth behavior. In *Proc. Graphics Interface '95*, pages 147–154, Quebec, Canada, 1995. Canadian Human-Computer Communications Society.

[102] R. Bridson, S. Marino, and R. Fedkiw. Simulation of clothing with folds and wrinkles. In *Proc. ACM SIGGRAPH/Eurographics Symp. Comput. Animation*, pages 28–36, Aire-la-Ville, Switzerland, 2003. Eurographics Assoc.

[103] A. A. Shabana. *Dynamics of Multibody Systems*. Cambridge Univ. Press, 4th edition, 2013.

[104] J. G. de Jalón and E. Bayo. *Kinematic and Dynamic Simulation of Multibody Systems: The Real-Time Challenge*. Springer Sci. Bus. Media, 2012.

[105] J. Baumgarte. Stabilization of constraints and integrals of motion in dynamical systems. *Comput. Methods Appl. Mech. Eng.*, 1(1):1–16, 1972.

[106] P. E. Nikravesh. *Computer-Aided Analysis of Mechanical Systems*. Prentice-Hall, Englewood Cliffs, NJ, USA, 1988.

[107] M. Géradin and A. Cardona. *Flexible Multibody Dynamics: A Finite Element Approach*. John Wiley & Sons, Chichester, U.K., 2001.

[108] J. G. Fulton and H. Schaub. Deployment dynamics analysis of an Origami-folded spacecraft appendage. *J. Spacecr. Rockets*, 59(6):2145–2157, 2022.

[109] Q. Zhang, Y. Liu, M. Li, Y. Han, J. Cai, and J. Feng. Simulation of dynamics during deployment of foldable Origami structures. *Int. J. Struct. Stab. Dyn.*, 20, 2020.

[110] H. M. Lankarani and P. E. Nikravesh. A contact force model with hysteresis damping for impact analysis of multibody systems. *J. Mech. Des.*, 112(3):369–376, 1990.

[111] M. Machado, P. Moreira, P. Flores, and H. M. Lankarani. Compliant contact force models in multibody dynamics: Evolution of the hertz contact theory. *Mech. Mach. Theory*, 53:99–121, 2012.

[112] H. Olsson, K. J. Åström, C. Canudas de Wit, M. Gäfvert, and P. Lischinsky. Friction models and friction compensation. *Eur. J. Control*, 4(3):176–195, 1998.

[113] L. Rios-Reyes and D. J. Scheeres. Generalized model for solar sails. *Journal of Spacecraft and Rockets*, 42(1):182–185, 2005.

[114] O. Mori et al. First solar power sail demonstration by IKAROS. *Trans. Jpn. Soc. Aeronaut. Space Sci., Aerosp. Technol. Jpn.*, 8(ists27):Psh_25–Psh_31, 2010.

[115] Y. Tsuda et al. Flight status of IKAROS deep space solar sail demonstrator. *Acta Astronaut.*, 69(9–10):833–840, 2011.

[116] A. D. Feucht, M. A. Clampin, et al. Design and development of the primary and secondary mirror deployment systems for the cryogenic jwst. In *Proceedings of the SPIE Astronomical Telescopes and Instrumentation Conference*, 2012.

[117] N. Kasdin, D. Lisman, S. Shaklan, M. Thomson, E. Cady, S. Martin, L. Marchen, R. Vanderbei, B. Macintosh, R. Rudd, D. Savransky, J. Mikula, and D. Lynch. Technology demonstration of starshade manufacturing for nasa's exoplanet mission program. In *Proc. SPIE Int. Soc. Opt. Eng.*, volume 8442, 2012.

[118] M. Arya et al. Demonstration of deployment repeatability of key starshade subsystems. *J. Astron. Telesc. Instrum. Syst.*, 7(2):021202, 2021.

[119] P. Willems et al. Nasa's starshade technology development activity. *J. Astron. Telesc. Instrum. Syst.*, 7(2):021203, 2021.

[120] M. W. Thomson. Starshade design for occulter-based exoplanet missions. In *Proc. SPIE*, volume 7731, page 773153, 2010.

[121] L. Dufour, L. S. Datashvili, F. Guinot, H. Legay, and G. Goussetis. Origami deployable reflector antenna for CubeSats. In *AIAA SciTech Forum*, 2021.

[122] A. Russo, B. Barakali, K. I. Kitsu, L. Baudet, J. Yang, and Z. You. Origami-inspired self-deployable reflectarray antenna. *Acta Astronaut.*, 213:240–251, 2023.

[123] S. V. Georgakopoulos, A.-S. Kaddour, C. L. Zekios, C. Ynchausti, L. L. Howell, and S. P. Magleby. Multifunctional and deployable Origami antennas. In *Proc. 3rd URSI Atlantic and Asia Pacific Radio Sci. Meeting (AT-AP-RASC)*, pages 1–3, 2022.

[124] Z. Zeng, T. Li, H. Dong, L. Yang, T. Liu, and X. Chen. Design method and driving optimization of Origami-inspired single-layer truss structures for

parabolic cylindrical mesh reflector antennas. *Front. Mech. Eng.*, 20(2):12, 2025.

[125] M. Sakovsky, I. Maqueda Jimenez, C. Karl, S. Pellegrino, and J. Costantine. Dual-matrix composite wideband antenna structures for CubeSats. In *Proc. 2nd AIAA Spacecraft Structures Conf.*, 2015.

[126] M. Sakovsky and S. Pellegrino. Closed cross-section dual-matrix composite hinge for deployable structures. *Composite Structures*, 208:784–795, 2019.

[127] D. B. Spencer et al. The LightSail 2 solar sailing technology demonstration. *Adv. Space Res.*, 67(9):2878–2889, 2021.

[128] Origami solar sail set to fly. *New Scientist*, 206(2760):10, 2010.

[129] J. Bell, L. Redmond, K. Carpenter, and J.-P. de la Croix. Dynamic characterization of a pop-up folding flat explorer robot (PUFFER) for planetary exploration. In *Proc. 38th IMAC Conf. Expos. Struct. Dyn., Topics in Modal Analysis & Testing, Vol. 8*, pages 383–391. Springer, 2020.

[130] M. T. Tolley et al. Self-folding Origami: Shape memory composites activated by uniform heating. *Smart Mater. Struct.*, 23(9):094006, 2014.

[131] D. Rus and M. T. Tolley. Design, fabrication and control of Origami robots. *Nat. Rev. Mater.*, 3:101–112, 2018.

[132] H. R. Kaufman. Experimental simulation of biased solar arrays with the space plasma. Technical Report NASA-CR-165485, NASA, 1981.

[133] J. Dever, S. Miller, E. Sechkar, and T. Wittberg. Space environment exposure of polymer films on the materials international space station experiment: Results from misse 1 and misse 2. *High Perform. Polym.*, 20:371–387, 2008.

[134] M. M. Finckenor and K. K. de Groh. Atomic oxygen exposure of polyimide foam for iss solar array wing blanket box assembly. Technical Report NASA/TM-2006-214325, NASA, 2006.

[135] K. K. de Groh and B. A. Banks. Atomic oxygen undercutting of long duration exposure facility aluminized-kapton multilayer insulation. *Journal of Spacecraft and Rockets*, 31(4):656–664, 1994.

[136] X. Zhang, H. Lin, H. Shang, J. Xu, J. Zhu, and W. Huang. Recent advances in functional fiber electronics. *SusMat*, 1(1):105–126, 2021.

[137] L. Wilson, S. Pellegrino, and R. Danner. Origami sunshield concepts for space telescopes. In *Proceedings of the 54th AIAA/ASME/ASCE/AHS/ASC Structures, Structural Dynamics, and Materials Conference*, number AIAA 2013-1594, Apr. 2013.

[138] Q. Ge et al. Active origami by 4d printing. *Smart Materials and Structures*, 23(9):094007, 2014.

[139] L. Seigner, G. K. Tshikwand, F. Wendler, and M. Kohl. Bi-directional origami-inspired sma folding microactuator. *Actuators*, 10(8):181, 2021.

[140] P. Boesch, M. Stelzer, and W. Bauer. Design and development of a cubesat solar array deployment mechanism. NASA Technical Memorandum NASA/TM–2018-219914, NASA, 2019.

[141] P. J. Senatore, A. T. Klesh, T. H. Zurbuchen, D. S. McKague, and J. W. Cutler. Concept, design, and prototyping of xsas: A high power extendable solar array for cubesat applications. In *Proceedings of the AIAA/USU Conference on Small Satellites*, 2010.

[142] Ph. Moignier. Shape memory alloy: Reversible hinge for deployment applications. In *Proceedings of the European Space Mechanisms and Tribology Symposium (ESMATS)*, 1999.

[143] M. Santer and S. Pellegrino. Compliant multistable structural elements. *International Journal of Solids and Structures*, 43(22–23):6969–6990, 2006.

[144] European Space Agency. Space engineering: Mechanisms. Technical Report ECSS-E-ST-33-01C Rev.2, European Space Agency, 2015.

[145] H. Patel, H. Arora, S. Joshi, and S. Mukherjee. Development of shape memory alloy (sma) based hold-down and release mechanism for space applications. In *Proceedings of the International Conference on Advances in Mechanical Engineering (ICAME)*, pages 393–403, 2021.

[146] S. Pellegrino. *Deployable Structures*. Springer, 2001.

[147] K. Kuriki, K. Ninomiya, M. Takei, and S. Matsuoka. Lessons learned from the space flyer unit (sfu) mission. *Acta Astronautica*, 51(11):797–806, 2002.

[148] M. M. Finckenor and K. K. de Groh. *A Researcher's Guide to: Space Environmental Effects*. Number NASA/NP–2015-03-015-JSC. NASA Johnson Space Center, 2021.

[149] M. Schenk, S. D. Guest, et al. Origami folding: A structural engineering approach. In *Origami 5: Fifth International Meeting of Origami Science, Mathematics, and Education*, pages 291–304. Rosen Publishing Group, 2011.

[150] R. C. van Schaik, H. J. C. Berendsen, A. E. Torda, and W. F. van Gunsteren. A structure refinement method based on molecular dynamics in four spatial dimensions. *Journal of Molecular Biology*, 234:751–762, 1993.

[151] H. Bekker. *Molecular Dynamics Simulation Methods Revised*. PhD thesis, University of Groningen, The Netherlands, 1996.

[152] S. E. Leon, E. N. Lages, C. N. de Araújo, and G. H. Paulino. On the effect of constraint parameters on the generalized displacement control method. *Mechanics Research Communications*, 56:123–129, 2014.

[153] Y. B. Yang and M. S. Shieh. Solution method for nonlinear problems with multiple critical points. *AIAA Journal*, 28(12):2110–2116, 1990.

[154] H. M. Hilber and T. J. R. Hughes. Collocation, dissipation and overshoot for time integration schemes in structural dynamics. *Earthquake Engineering and Structural Dynamics*, 6(1):99–117, 1978.

[155] A. H. Sharma, T. J. Rose, A. Seamone, T. W. Murphey, and F. Lopez Jimenez. Analysis of the column bending test for large curvature bending of high strain composites. In *Proc. AIAA SciTech 2019 Forum*, 2019.

[156] A. Ghassaei, E. D. Demaine, and N. Gershenfeld. Fast, interactive origami simulation using gpu computation. In *Origami 7: Proceedings of the 7th*

International Meeting on Origami in Science, Mathematics and Education (OSME 2018), pages 1151–1166, 2018.

[157] R. W. Ogden. *Non-Linear Elastic Deformations*. Dover Publications, Mineola, NY, USA, 1997.

[158] K. Liu and G. H. Paulino. Merlin: A matlab implementation to capture highly nonlinear behavior of non-rigid origami. In *Proceedings of the IASS Annual Symposium*, 2016.

[159] V. F. Pisarenko. Retrieval of harmonics from a covariance function. *Geophysical Journal International*, 33(3):347–366, 1973.

[160] S. Lenci, G. Rega, et al. *Global Nonlinear Dynamics for Engineering Design and System Safety*. Springer, 2019.

[161] M. Amabili. Nonlinear damping in large-amplitude vibrations: Modelling and experiments. *Nonlinear Dynamics*, 93(1):5–18, 2018.

[162] S. Herkal, S. Nagarajaiah, and G. H. Paulino. Dynamic behavior of origami structures: Computational and experimental study. *arXiv preprint arXiv:2408.01889*, 2024.

6.1 Appendix

6.1.1 Panel traction benchmark

Geometry. A single square facet of side length $L = 1$ m is discretised by four edge bars and one diagonal bar (Fig. 6.1). The angle γ between the y-axis and the diagonal bars joining the blue (loaded) and red (supported) nodes is varied from 0° (aligned with the y-axis) to 50° while keeping all bar lengths equal to unity; this reproduces the skew study reported by Filipov *et al.* [62].

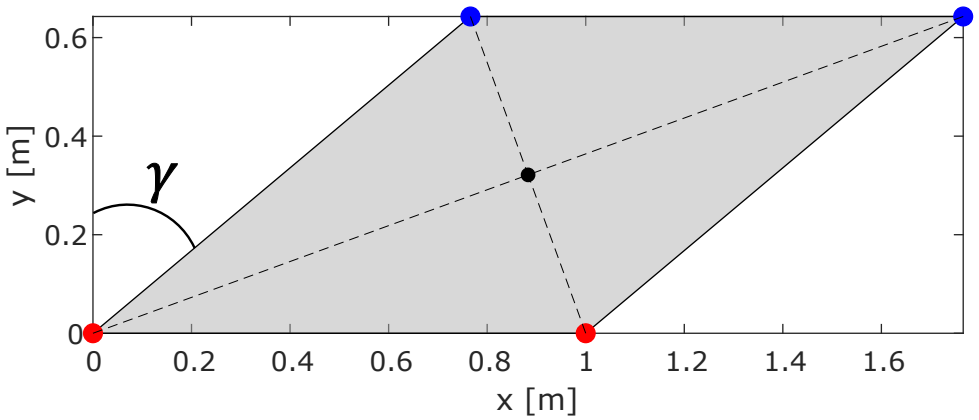

Figure 6.1: Panel traction set-up: blue nodes are loaded; one red node is fully fixed, the other is fixed in y and z but free in x. Dashed line indicates the variable skew bar.

Boundary conditions and loading. The lower-left red node is fully clamped, whereas the lower-right red node is constrained only in y and z to permit in-plane Poisson contraction. A unit vertical point load ($F_z = 1$ N) is applied to each of the two blue nodes, generating pure traction in the z-direction.

Material parameters and solver. Material properties match Table 5.1. A static Newton–Raphson procedure with 10^{-6} N residual tolerance is used for each value of γ.

Normalised vertical stiffness. Following Filipov *et al.*, the vertical stiffness is computed as $K = F/\langle\Delta_z\rangle$, where $\langle\Delta_z\rangle$ is the average vertical displacement of the loaded edge. The value is then normalised by the axial stiffness of an unskewed sheet,

$$\overline{K}(\gamma) \;=\; \frac{F/\langle \Delta_z \rangle}{E\,W\,t/H},$$

in which E is Young's modulus, t the thickness, W the panel width along the x axis and H the panel height along the y axis.

Results and discussion. Figure 6.2 plots the normalised stiffness $\overline{K}$ against γ for both the bar–and–hinge model and the reference nonlinear shell FE analysis. The two curves are nearly coincident up to $\gamma \approx 10°$; thereafter the bar–and–hinge prediction is slightly stiffer, with a peak deviation of 9% at $\gamma \approx 30°$. The trend and magnitude match the observations reported by Filipov *et al.*, confirming that the present formulation reproduces the in-plane traction behaviour of a skewed panel with satisfactory fidelity. This benchmark therefore validates the axial-stretch component of the hinge calibration before progressing to coupled shear and bending tests.

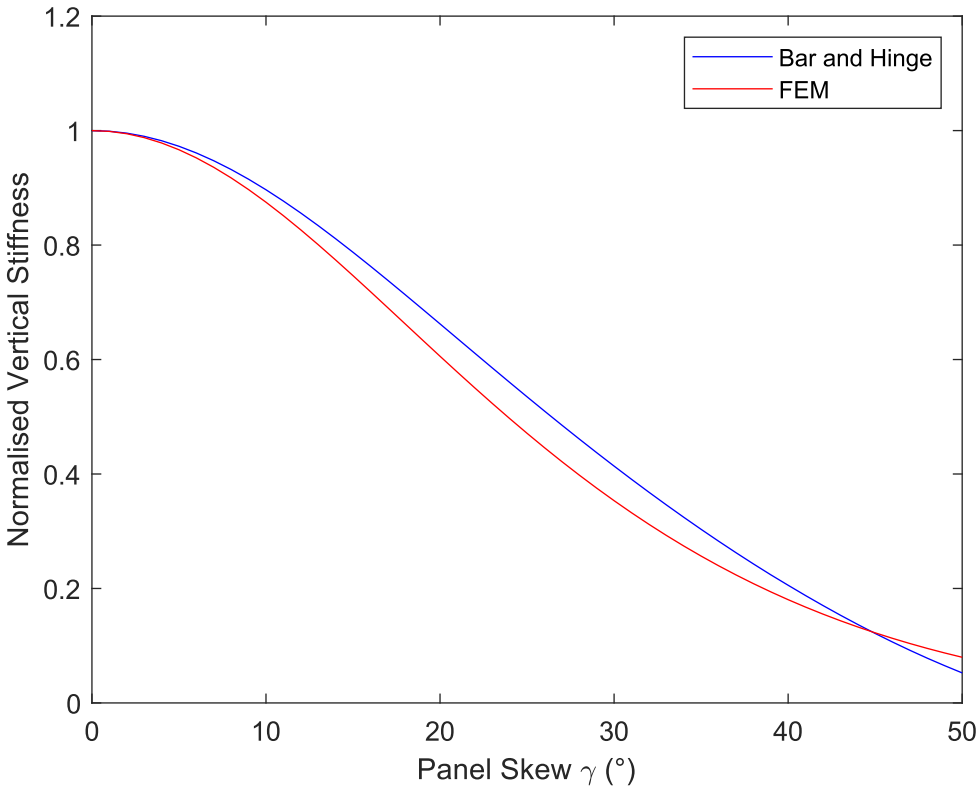

Figure 6.2: Normalised vertical stiffness versus panel skew angle γ: bar–and–hinge model (blue) and FE reference (red).

6.1.2 Panel shear benchmark

Geometry and skew parameter. The same 1×1 m^2 facet and bar–hinge layout used in Section 6.1.1 is adopted here (Fig. 6.1). The diagonal-bar skew angle γ again varies from 0° to 50° while the bar lengths remain unity.

Boundary conditions and loading. Both red nodes are fully clamped ($u_x = u_y = u_z = 0$). The blue nodes are restrained in y and z but free in x. A unit horizontal load $F_x = 1$ N is applied to each blue node, producing an in-plane shear deformation of the panel.

Normalised horizontal stiffness. Following Filipov *et al.* [62], the shear stiffness is defined as $K = F/\langle\Delta_x\rangle$, where $\langle\Delta_x\rangle$ is the average horizontal displacement of the loaded edge, and is normalised by the analytical shear stiffness of a thin elastic sheet,

$$\overline{K}(\gamma) \;=\; \frac{F/\langle\Delta_x\rangle}{G\,t\,W/H},$$

with G being the shear modulus.

Solver details. Material properties coincide with Table 5.1. A static Newton–Raphson scheme with a 10^{-6} N residual tolerance is employed for every γ.

Results and discussion. Figure 6.3 plots $\overline{K}$ versus γ. In contrast to the traction case, the bar–and–hinge model (red) *overestimates* the shear stiffness across the entire skew range, reproducing the 30–80 % bias reported in Filipov's original study. The discrepancy peaks at $\gamma \approx 30^\circ$, where the bar–and–hinge value is roughly 50 % higher than the FE reference, and diminishes as the diagonal aligns with the panel edge at $\gamma = 50^\circ$.

The systematic over-prediction is expected: the N5B8 discretisation assigns purely axial bars to represent in-plane shear, which stiffens the response compared with continuum shear deformation. Nonetheless, the model captures the qualitative trend, a mild rise followed by a drop in $\overline{K}$, and the magnitude of the error is consistent with published benchmarks. These results validate that the present implementation reproduces the known limitations and performance of the original bar–and–hinge formulation in shear, providing a reliable baseline for the coupled shear-bending analyses that follow.

6.1.3 Panel bending benchmark

Geometry and skew parameter. The same 1×1 m^2 square facet and bar–hinge topology is retained (Fig. 6.4). The diagonal-bar skew angle γ is set to 0°,15°,30°,45°, 60°,75°,

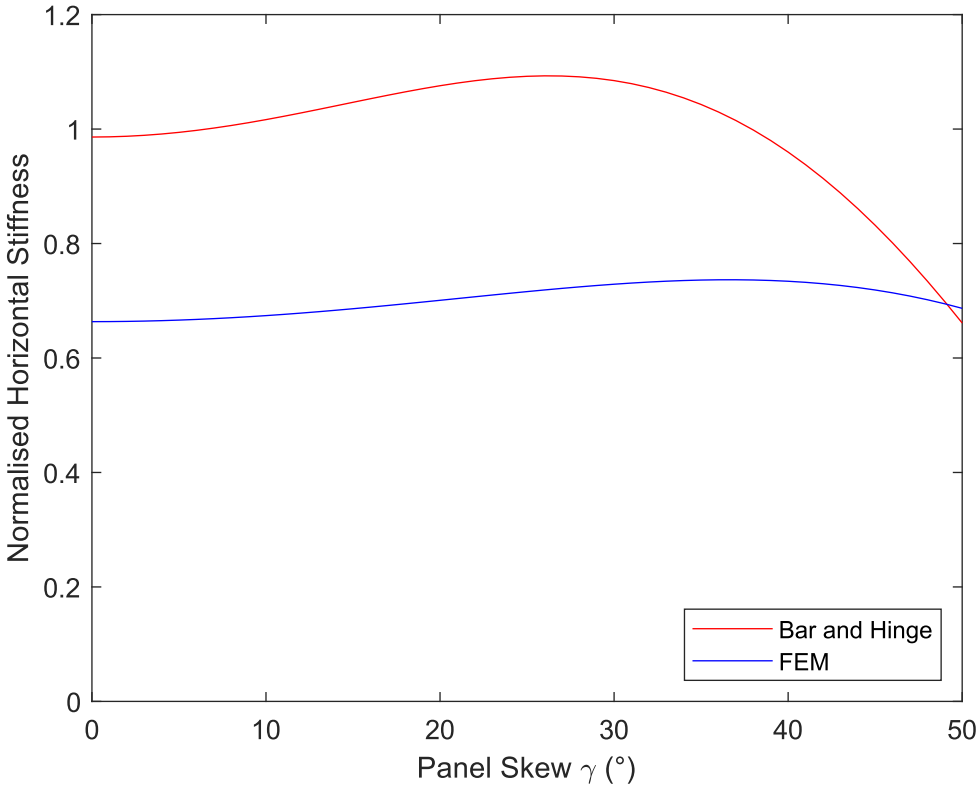

Figure 6.3: Normalised horizontal (shear) stiffness versus panel skew γ: bar–and–hinge model (red) and FE reference (blue).

matching the study of Filipov *et al.* [62].

Boundary conditions and loading. All three red nodes are fully fixed. A vertical point load $F_z = 0.5$ N is applied to the single blue node, inducing out-of-plane bending.

Normalised bending moment. Following Filipov *et al.*, the bending response is reported as the dimensionless ratio

$$\frac{M_B}{k} = \frac{F \cdot L/4}{k},$$

where M_B is the equivalent bending moment produced by the applied load, k is the crease-line rotational stiffness, and L is the panel side length. The abscissa is the panel bending angle θ_B, measured as the rotation of the upper facet about the crease line. The simulations are run until $\theta_B \approx 1.3$ rad; the linear-elastic regime terminates at the critical value $\theta_1 = 20° = 0.35$ rad.

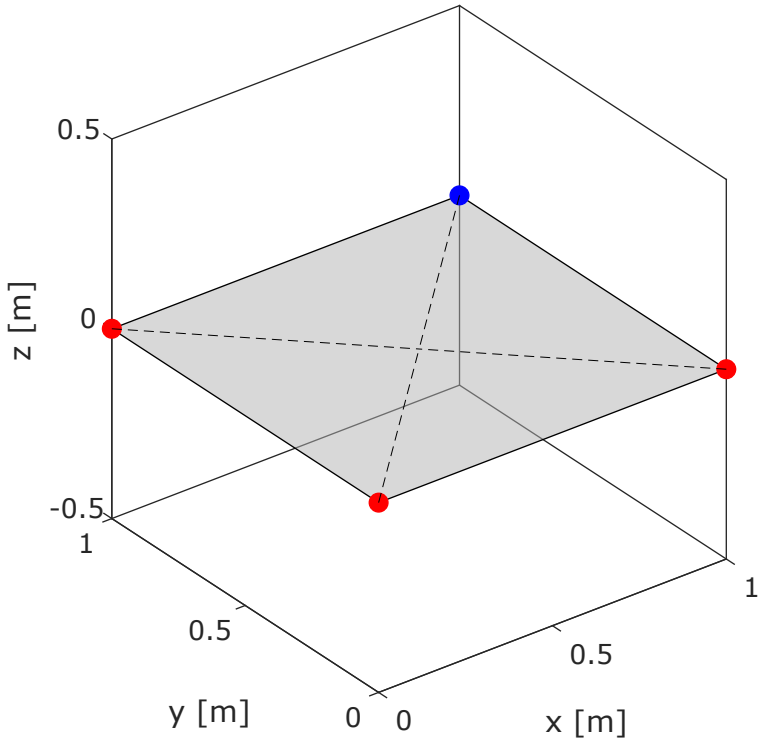

Figure 6.4: Panel bending set-up: red nodes fully clamped; a vertical load $F_z = 0.5$ N is applied to the blue node.

Choice of bilinear parameters. The transition angle θ_1 and the post-yield slope k_2 do not follow from first principles: they depend on sheet thickness, crease-line radius, material properties and geometrical factors, as discussed by Filipov *et al.* [62]. In the absence of dedicated experiments for a specific material considered here, θ_1 has been set arbitrarily to 20° ($= 0.35$ rad). This value provides a conservative estimate of fold-softening and is expected to be updated once hinge-bending tests become available (see Section **??** on planned experimental validation).

Solver settings. Material constants match Table 5.1. The Newton–Raphson residual tolerance is 10^{-6} N m with adaptive load increments to maintain quadratic convergence.

Results and discussion. Figure 6.5 plots M_B/k versus θ_B for each γ. The response is linear up to $\theta_1 \approx 0.35$ rad, in agreement with Filipov's analytical prediction. Beyond this threshold the panels stiffen, and the rate of stiffness increase grows monotonically with γ: the $\gamma = 75^\circ$ configuration is roughly twice as stiff as the

$\gamma = 30°$ configuration at $\theta_B = 1.0$ rad. This trend reflects the greater contribution of membrane stretching in highly skewed panels once bending strains exceed the small-angle limit.

Quantitatively, the bar–and–hinge curves reproduce the slope change at θ_1 and the ordering of stiffness with γ; deviations from Filipov's reference remain below 8% over the full bending range. The benchmark therefore validates the out-of-plane bending behaviour of the present implementation and confirms its suitability for simulating coupled membrane–bending deformations in origami sheets.

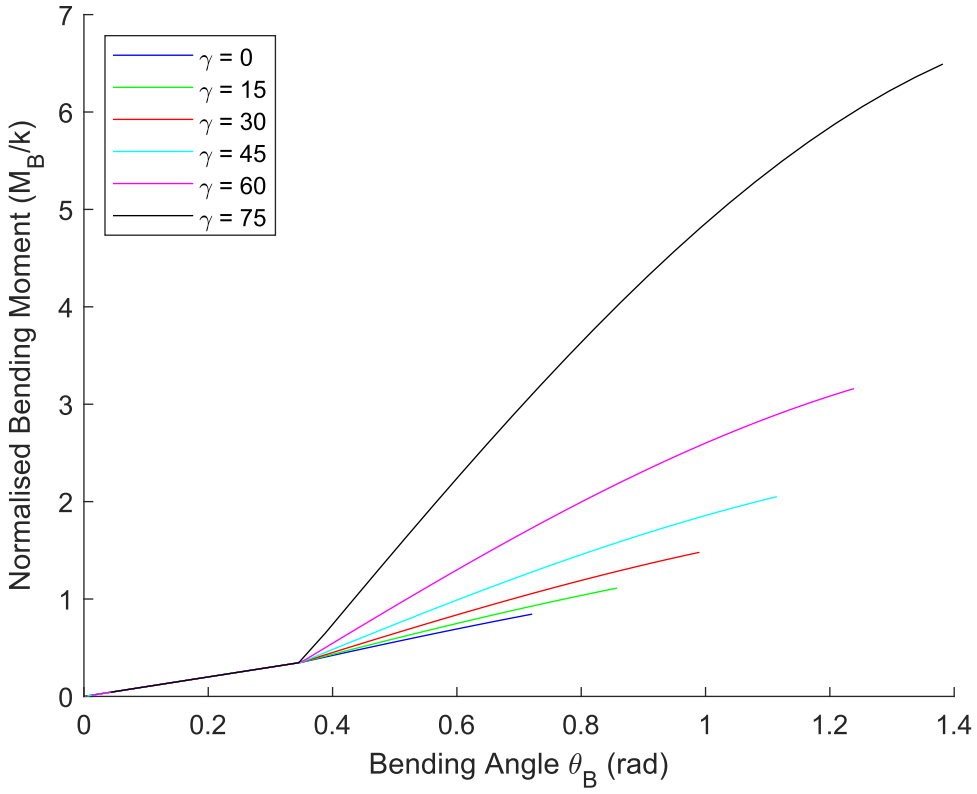

Figure 6.5: Normalised bending moment M_B/k versus bending angle θ_B for skew angles $\gamma = 0°$ (blue) to $75°$ (black).